Title
A G/NARRLI Effort: Measuring the Ionization Yield of Low-Energy Nuclear Recoils in Liquid Argon

Author
Joshi, Tenzing Henry Yatish

Publication Date
2014

Peer reviewed|Thesis/dissertation

A G/NARRLI Effort:
Measuring the Ionization Yield of Low-Energy Nuclear Recoils in Liquid Argon

by

Tenzing Henry Yatish Joshi

A dissertation submitted in partial satisfaction of the
requirements for the degree of
Doctor of Philosophy

in

Nuclear Engineering

in the

Graduate Division

of the

University of California, Berkeley

Committee in charge:

Professor Eric Norman, Chair
Doctor Adam Bernstein
Professor Edward Morse
Professor James Siegrist

Spring 2014

A G/NARRLI Effort:
Measuring the Ionization Yield of Low-Energy Nuclear Recoils in Liquid Argon

Abstract

A G/NARRLI Effort:
Measuring the Ionization Yield of Low-Energy Nuclear Recoils in Liquid Argon

by

Tenzing Henry Yatish Joshi

Doctor of Philosophy in Nuclear Engineering

University of California, Berkeley

Professor Eric Norman, Chair

Liquid argon has long been used for particle detection due to its attractive drift properties, ample abundance, and reasonable density. The response of liquid argon to low-energy $\mathcal{O}(10^2 - 10^4$ eV) interactions is, however, largely unexplored. Weakly interacting massive particles such as neutrinos and hypothetical dark-matter particles (WIMPs) are predicted to coherently scatter on atomic nuclei, leaving only an isolated low-energy nuclear recoil as evidence. The response of liquid argon to low-energy nuclear recoils must be studied to determine the sensitivity of liquid argon based detectors to these unobserved interactions. Detectors sensitive to coherent neutrino-nucleus scattering may be used to monitor nuclear reactors from a distance, to detect neutrinos from supernova, and to test the predicted behavior of neutrinos. Additionally, direct detection of hypothetical weakly interacting dark matter would be a large step toward understanding the substance that accounts for nearly 27% of the universe. In this dissertation I discuss a small dual-phase (liquid-gas) argon proportional scintillation counter built to study the low-energy regime and several novel calibration and characterization techniques developed to study the response of liquid argon to low-energy $\mathcal{O}(10^2 - 10^4$ eV) interactions.

For Georgina and Louise

Contents

List of Figures

List of Tables

Acknowledgments

This work was a part of a collaborative effort based at LLNL. Though progress was sometimes slow, the successes arrived thanks to the hard and persistent work of our small cohort. A GNARRLI effort indeed...

I thank my advisors Rick Norman and Adam Bernstein for being mentors, role-models, and partners through this process. While it may go unnoticed by some, Rick's teaching and advising style mandates self-responsibility. I am truly grateful for the trust that Rick placed in me and I admire Rick's experimental mindset. Adam has put together a terrific group at LLNL, bridging nuclear security and particle physics. I am thankful to have been a part of it over the past several years and am grateful to Adam for the perspective he has helped me develop.

I also thank Jim Siegrist and Ed Morse for sitting on my committee and sharing their insights and suggestions.

I thank all of the CENNS collaborators that I have worked with. Samuele Sangiorgio for the knowledge he has shared and the persistence he demonstrated throughout this effort. Samuele's work touched nearly every aspect of this experiment. Peter Sorensen's pragmatic approach was crucial in our push for nuclear recoil data. Additionally, when Peter wasn't down a mine shaft or at a conference he openly shared expertise on dark matter searches, data analysis, and relevant xkcd comics. Michael Foxe, my graduate student partner for his wide ranging work on this project. From work on detector design, to putting together the slow controls, to countless hours in the lab, Mike play a large part in moving this effort forward. Though we had some good times in the lab, the best memory I have is the trip to Anfield! Kareem Kazkaz for always having an open door. Whether it was a 30 second question about coding or an open ended idea, Kareem always made the time to answer my questions and conversations. Sergey Pereverzev for his work on this project, and for teaching me that sometimes it is necessary to be stubborn, but not always. Finn Rebassoo for his work on improving our analysis. Vladimir Mozin for his help with simulations and neutron source design. Chris Hagmann for his many perspectives throughout the project. Tim Gushe for the time he spent working with us over the summers. Jon Coleman and Kostas Mavrokoridis for their help with the TPB depositions. Igor Jovanovic for being a mentor while I was at Purdue and for his collaboration on this effort. I'm very grateful for some of the advice that you have shared over the years.

I must thank several others in helping this experimental effort succeed. Randy Hill for fabricating nearly everything for us and helping us to design a successful experiment. Graham Bench for helping us get the microprobe and neutron source running, and allowing us to run our experiment at CAMS. Tom Brown for keeping us out of trouble at CAMS. Jason Burke for taking the time and lending the equipment to help get

the neutron source up and running. Additionally Jason connected us with Vincent Meot who fabricated new lithium targets for our experiment, thanks Vincent.

At times it felt like years of frustration working on this project. Fortunately there were plenty of good times to be had in Berkeley, around the Bay, and in Tahoe. To all of my friends and housemates who have added beauty, fun, and adventure to my many memories, thank you. And a very special thank you to Kelly Karns for being an amazing friend from day one... and opening a bank account with me on day two.

During my time in Berkeley I found my partner, Lowry. Thank you Lowry, for giving me the support and encouragement I needed to see this through. I am excited to see what comes next! Lets find out together!

for all of the support and encouragement you have given me throughout this process.

Finally I would like to thank my family; Yatish, Louise, Georgina, and Avatar. You have provided me with the opportunity to make it to this point and supported me along every step of the way.

The author wrote this dissertation in support of requirements for the degree Doctor of Philosophy in Nuclear Engineering at the University of California, Berkeley. The research is funded in part by the LLNL Graduate Scholars Program, and is not a deliverable for any United States government agency. The views and opinions expressed are those of the author, and do not state or reflect those of the United States government or Lawrence Livermore National Security, LLC.

Neither the United States government nor Lawrence Livermore National Security, LLC, nor any of their employees makes any warranty, expressed or implied, or assumes any legal liability or responsibility for the accuracy, completeness, or usefulness of any information, apparatus, product, or process disclosed, or represents that its use would not infringe privately owned rights. Reference herein to any specific commercial product, process, or service by trade name, trademark, manufacturer, or otherwise does not necessarily constitute or imply its endorsement, recommendation, or favoring by the United States government or Lawrence Livermore National Security, LLC, and shall not be used for advertising or product endorsement purposes.

This work was performed under the auspices of the U.S. Department of Energy by Lawrence Livermore National Laboratory under Contract DE-AC52-07NA27344. I would like to thank the Lawrence Scholars Program at LLNL and the Department of Homeland Security's DoNuTS grant to UC Berkeley for funding my research. LLNL-TH-654146

Chapter 1

Introduction

Since the discovery of radioactivity, radiation detectors have served as humanity's window into the sub-atomic world. With the continued improvement of detectors we have studied isotopes ever further from stability, developed imaging techniques that have revolutionized medical treatment, and tested the fundamental theories which attempt to describe the natural world. This dissertation is centered around applying nuclear physics to calibrate and characterize radiation detectors (specifically dual-phase argon detectors) at energies lower than have been previously demonstrated.

The motivation for this study is spread between fundamental physics and nuclear non-proliferation, detailed study of the neutrino, and the monitoring of plutonium production in nuclear reactors. The primary question being: *Are liquid argon based detectors capable of detecting coherent elastic neutrino nucleus scattering (CENNS)?* CENNS is predicted by the Standard Model of Particle Physics (SM) but has never before been observed. Detection and study would be a new test of the standard model. Additionally, CENNS detectors could potentially monitor nuclear power plants from a distance in a detector volume smaller than the current detectors.

The research presented here was performed within a collaboration based at LLNL and with collaborators from the University of California Berkeley, the Pennsylvania State University, and the University of Liverpool. In this dissertation I present my own contributions to the broader collaboration effort, but gratefully acknowledge all of the help of my collaborators. In this chapter I introduce the relevant topics. Chapter 2 presents a description of the prototype dual-phase detector that was built at LLNL. Chapter 3 describes the quasi-monoenergetic neutron source that I designed for nuclear recoil measurements. Chapter 4 presents the first measurement of nuclear recoil ionization yield in liquid argon, made using the aforementioned neutron source. Chapter 5 introduces the idea of using resonant photo-nuclear scatter to produce sub-keV nuclear recoils and Chapter 6 includes thoughts on possible future measurements and conclusions.

1.1 Neutrinos (ν) & Antineutrinos ($\bar{\nu}$)

Hypothesized by Pauli in 1930, the neutrino (ν) and its antimatter counterpart ($\bar{\nu}$) laid the foundation for the theory of nuclear β-decay [36] and the Weak Interaction. Building on this theoretical understanding, experimental observation of the $\bar{\nu}$ occurred in 1956 when Cowan, Reines, et al. detected $\bar{\nu} + p \rightarrow n + e^+$, sometimes referred to as inverse β-decay, at a nuclear reactor [28]. Detection of the ν was reported by Davis et al. during an experiment attempting to use neutrinos to validate the standard solar model [31]. The experiment, in the Homestake mine in South Dakota, used a volume of tetrachloroethylene and searched for $\nu + {}^{37}\mathrm{Cl} \rightarrow {}^{37}\mathrm{Ar} + e^-$. Though the experiment successfully observed neutrinos of solar origin, the rate of detection was $\sim$ 37% of that expected [32]. This deficit gave rise to the solar neutrino problem.

This problem was eventually laid to rest by the Sudbury Neutrino Observatory (SNO) experiment [3], confirming the hypothesis that neutrinos undergo flavor oscillation, violating conservation of lepton flavor and implying neutrinos are massive. The implications of this discovery were far reaching because the neutrinos of the Standard Model of Particle Physics (SM) are massless Dirac neutrinos. This is evidence of physics beyond the Standard Model. Since this discovery, experiments have set out to measure the mixing angles describing neutrino oscillation, the mass differences of the different eigenstates, and the Majorana or Dirac nature of neutrinos. Additionally, experiments have been proposed to search for short baseline neutrino oscillations that would result from sterile neutrino flavors.

Neutrinos have directly shown that, despite its many triumphs, the SM is incomplete. This knowledge presents an opportunity for physicists around the world to test the many predictions of SM neutrino properties to look for additional discrepancies. One SM prediction that has never been observed is the coherent scatter of neutrinos on atomic nuclei, often referred to as coherent elastic neutrino-nucleus scattering (CENNS).

Coherent elastic neutrino-nucleus scattering

Mediated by the weak neutral boson, the Z^0, CENNS is flavor-blind neutrino-nucleus elastic scatter. Predicted in 1974 by D.Z. Freedman [37] and elaborated on by Drukier and Stodolsky in 1984 [35], CENNS as eluded detection for 40 years. The cross-section for interaction is predicted to be

$$\frac{d\sigma}{d(\mathrm{Cos}\ \theta)} = \frac{G_F^2}{8\pi}\left[Z\left(4\sin^2\theta_W - 1\right) + N\right]^2 E_\nu^2\ (1 + \cos\theta), \tag{1.1}$$

where G_F is the Fermi constant, θ_W is the weak (Weinberg) mixing angle, Z is the proton number of the target nucleus, N is the neutron number of the target nucleus, E_ν is the neutrino energy, and θ is the scattering angle. The weak mixing angle has been measured

as $sin\theta_w \simeq 0.23 - 0.24$ [13]. As an approximation, taking $\sin^2\theta_w = 0.25$, the differential cross-section simplifies to

$$\frac{d\sigma}{d(\cos\theta)} \simeq \frac{G_F^2}{8\pi} N^2 E_\nu^2 (1 + \cos\theta). \tag{1.2}$$

This approximation is good to $5 - 15\%$, and convenient for order of magnitude calculations. The cross-section enhancement provided by the coherent interaction with all nucleons $\propto N^2$ results in a significantly larger cross-section that that of inverse beta-decay for high N(Z) nuclei. As a result, CENNS is the interaction with the largest cross-section for neutrinos with wavelengths larger than the size of the nucleus ($E_\nu <\sim 50$ MeV), necessary for coherent interaction with all nucleons. This makes CENNS detectors attractive for studying neutrinos from our sun, reactors, and supernova. Additionally, CENNS is likely to be a limiting background for next generation dark matter searches [29] and plays a major role in supernova dynamics.

The resultant signal from CENNS is a recoiling atom, often referred to as a nuclear recoil. The energy of the recoiling atom is simply,

$$E_R = \frac{E_\nu^2 (1 - \cos\theta)}{2\text{MA}}, \tag{1.3}$$

where M is the mass of the nucleon and A is the atomic number of the target nucleus. The mean recoil energy is

$$\overline{E_R} = \frac{2E_\nu^2}{3\text{MA}} \simeq \left(\frac{E_\nu}{1\text{MeV}}\right)^2 \frac{2}{3\text{A}}\ [\text{keV}], \tag{1.4}$$

where M$\sim$ 1 GeV. The very low energy of the resultant nuclear recoils, in combination with the very small cross-section of all neutrino interactions, are the primary reasons that CENNS has not yet been observed. Figure 1.1 shows the mean recoil energy as a function of neutrino energy for several different target isotopes and the total cross-section as function of neutrino energy for different target isotopes.

The detection of CENNS of solar or reactor neutrinos requires a device sensitive to nuclear recoils below 1 keV. Searching for higher energy neutrinos like those from a stopped pion source would require thresholds of $\mathcal{O}$(keV). These thresholds are made more challenging by the fact that nuclear recoils produce less ionization and excitation than an electron recoil of the same energy due to a loss of energy to phonon production, a phenomena sometimes called quenching. In addition to the requirement of a very low threshold, CENNS detection devices also require very low backgrounds in the region of interest. This is a significant challenge in itself because attempted observation at either a reactor or a stopped pion source would require near-surface deployment. The need for low backgrounds mandates significant shielding and detector construction of low radioactivity materials. One attractive option for improving background rejection in

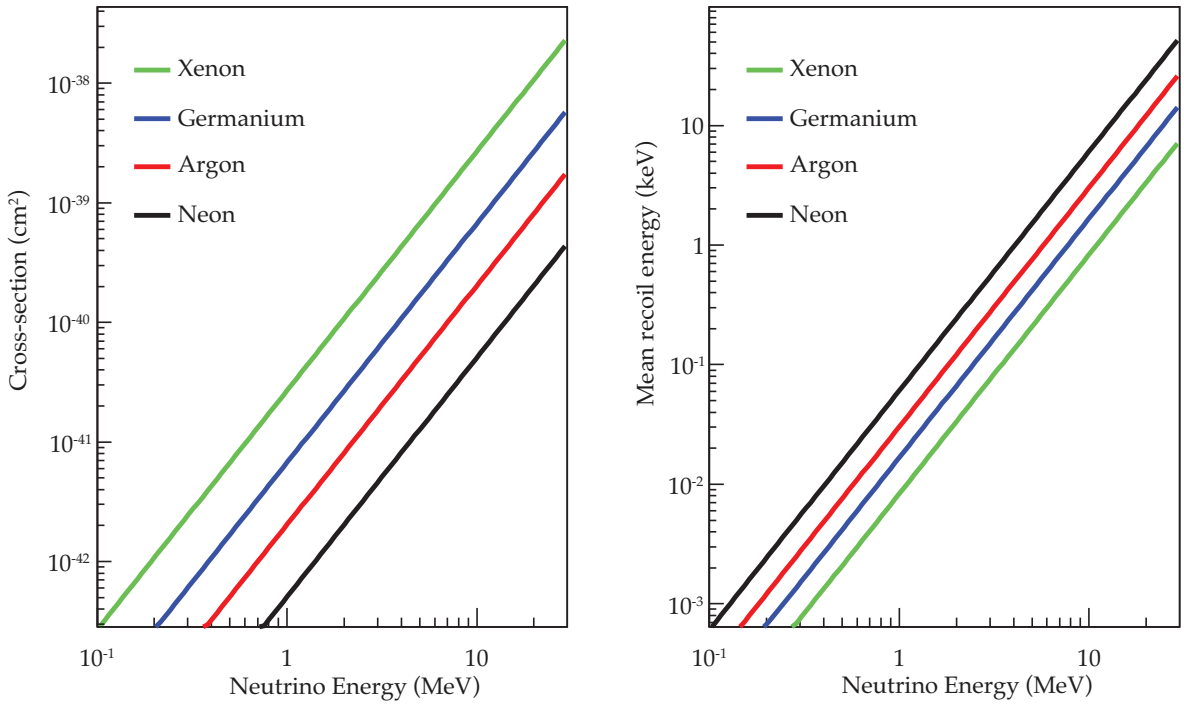

Figure 1.1: Mean recoil energy and total cross-section as a function of neutrino energy for CENNS with different targets

candidate devices is the ability to discriminate nuclear recoils from electron recoils (e.g. Compton electrons). While several detector technologies have demonstrated this ability, the discrimination power falls with recoil energy.

ν & $\bar{\nu}$ sources

Neutrinos are produced during weak interactions (e.g. β-decay, meson decay, and lepton decay). One way of categorizing the sources of neutrinos is: solar, radioactive decay of natural materials, cosmic-ray interactions, relics of the big-bang, and manmade. For the purpose of this work it is the manmade sources of neutrinos that are most interesting. Specifically nuclear reactors and stopped pion sources that are capable of producing significant quantities of neutrinos with $E_\nu < 50$ MeV.

Nuclear reactors are prolific sources of $\bar{\nu}_e$. In a typical 3 GW_{th} nuclear power plant, $\sim 10^{21}$ $\bar{\nu}_e$ are emitted isotropically every second. In reactors, a chain reaction of the neutron induced fission of fissile and fissionable isotopes is controlled. The fission products are neutron-rich and thus unstable to β^- decay. As the fission products relax towards stability, $\bar{\nu}_e$ are emitted. The distribution of fission products is bimodal and varies for

the fission of different isotopes. This variation in fission product distribution results in differences in the mean number of $\bar{\nu}_e$ emitted per fission and the energy spectrum of emitted $\bar{\nu}_e$ per fission (Fig. 1.2) [75], and in turn alter the nuclear recoil spectrum from CENNS (Fig. 1.3). Precise understanding of these differences are important for reactor based neutrino oscillation experiments.

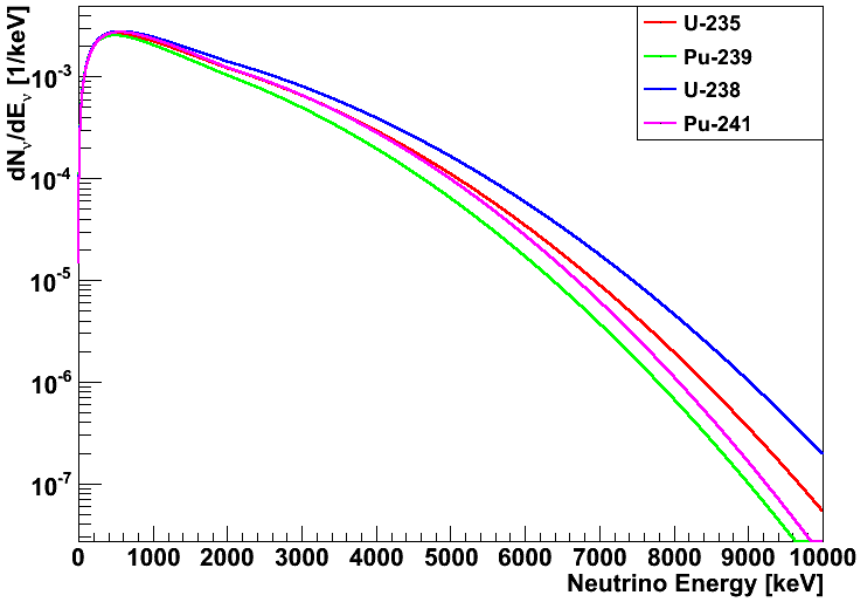

Figure 1.2: Figure courtesy of LLNL collaboration. Fission $\bar{\nu}_e$ spectra for common fissile isotopes per fission [75].

Another manmade source of neutrinos are stopped pion sources such as the Spallation Neutron Source (SNS) at Oak Ridge National Laboratory. In these sources, high energy protons $\mathcal{O}$(GeV) produce pions (π^+ & π^-) within a high-Z target; also creating large numbers of spallation neutrons. The π^- are captured within the target but the π^+ quickly decay at rest into $\mu^+ + \nu_\mu$ producing mono energetic 29.9 MeV ν_μ. Eventually the μ^+ also decay through a three-body decay into $e^+ + \bar{\nu_\mu} + \nu_e$. The neutrinos produced in this decay populate a spectrum with maximum energy of 52.85 MeV, half the rest mass of the μ^+. Figures 1.4 and 1.5 illustrate the neutrino and CENNS recoil spectra expected at the Spallation Neutron Source at ORNL. The pulsed time signature of stopped pion sources and the resultant high energy neutrinos make these sources attractive for CENNS experiments. Figure 1.6 shows expected signal rates for experiments at a spallation source (ISIS) and a typical power reactor for different target materials as a function of threshold recoil energy (10 m standoff).

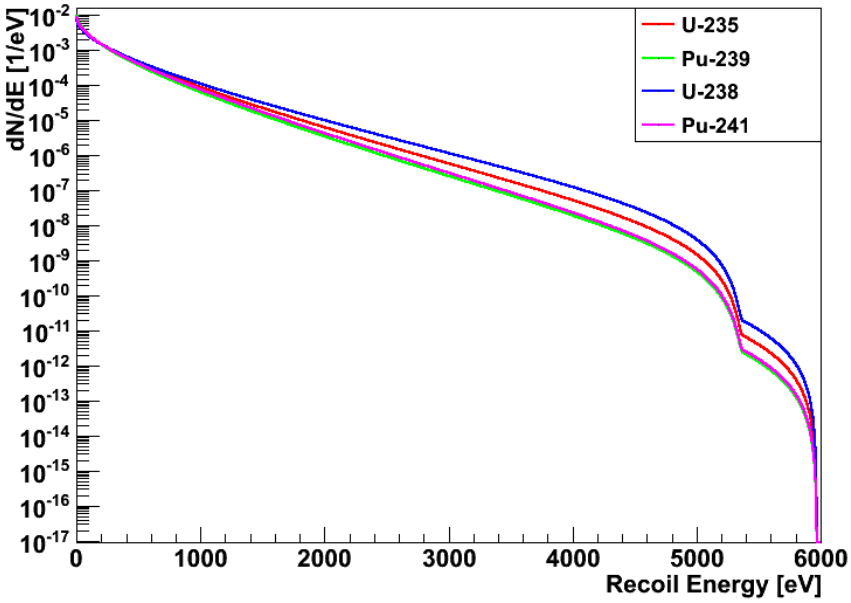

Figure 1.3: Figure courtesy of LLNL collaboration. Nuclear recoil spectra from CENNS of reactor $\bar{\nu}_e$.

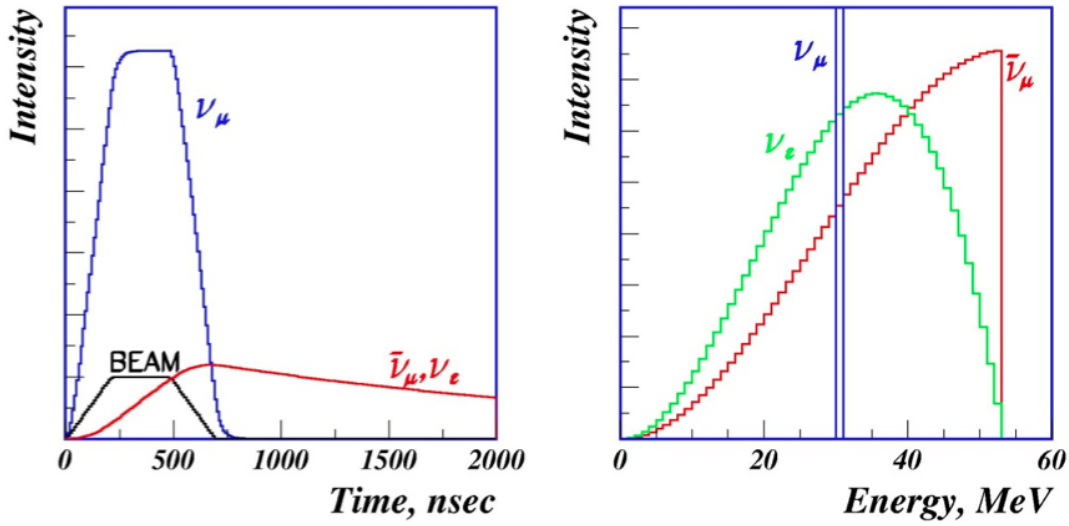

Figure 1.4: Figure from [15]. Stopped pion ν & $\bar{\nu}$ spectra and temporal structure at the Spallation Neutron Source.

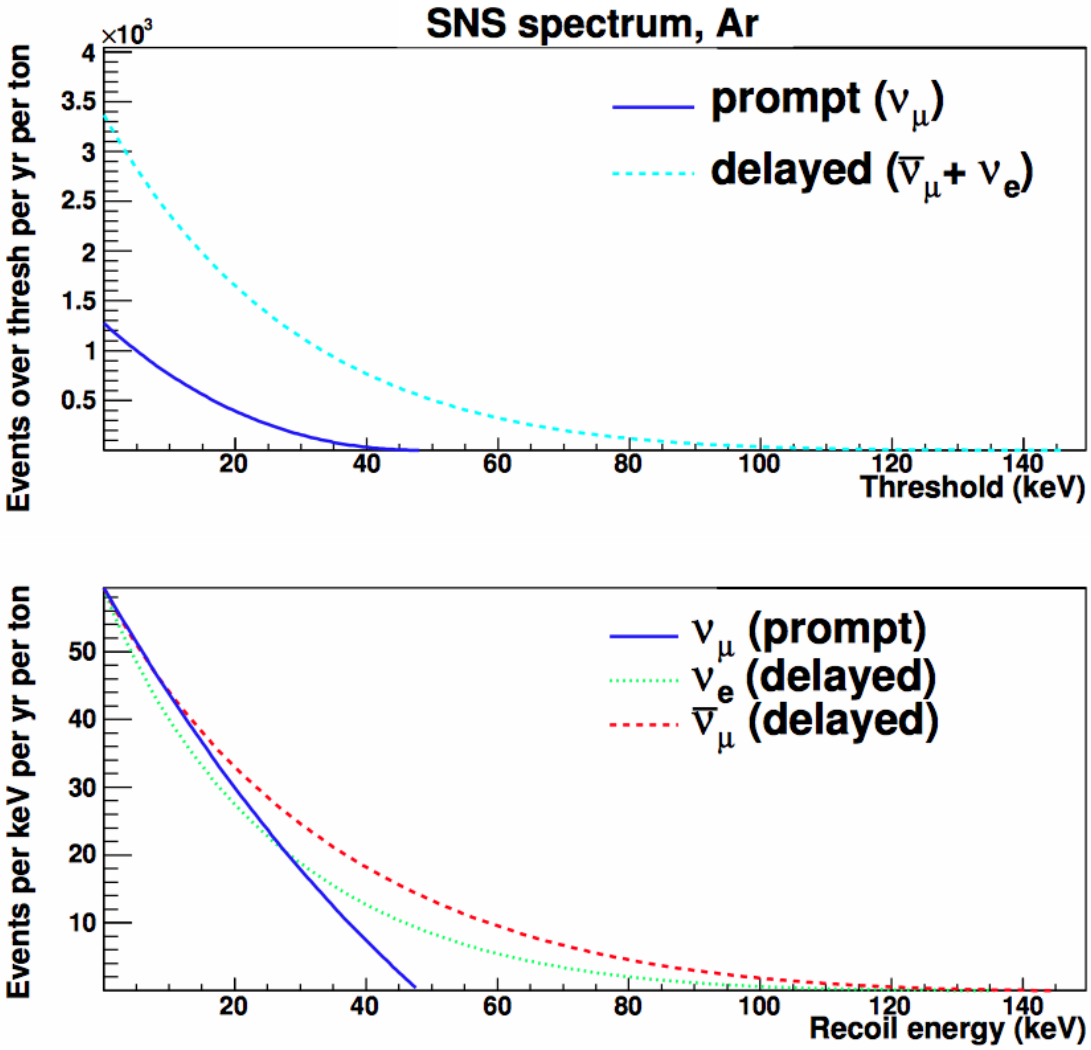

Figure 1.5: Figure from [15]. (top) CENNS detection rate as a function of detector threshold for an argon detector at the SNS. CENNS event rate as a function of recoil energy from CENNS of stopped pion ν & $\bar{\nu}$.

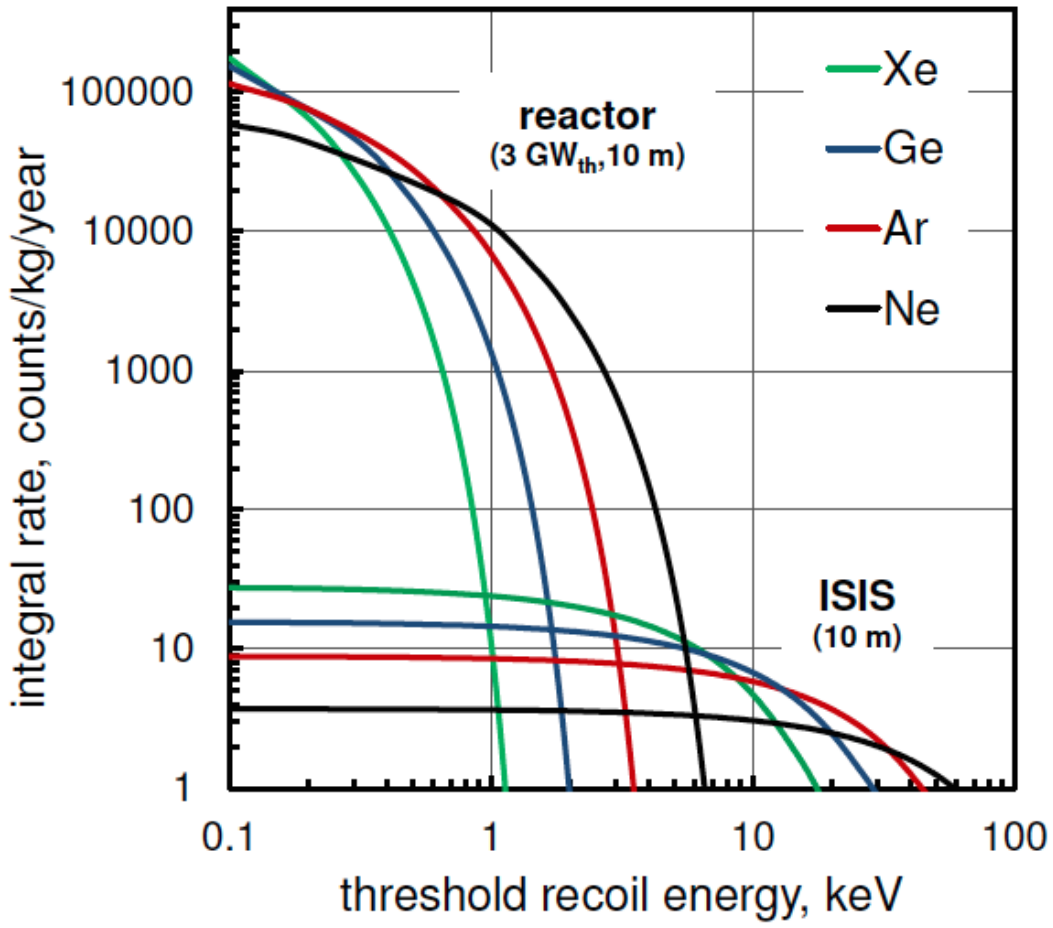

Figure 1.6: Figure from [23]. Expected number of detectable CENNS events at a stopped pion source and a reactor as a function of detector energy threshold for a 10 m standoff.

Parallels with dark matter searches

There is an increasing amount of evidence that $\sim$ 23% of the universe is some type of non-baryonic dark matter [38]. While all evidence for this dark matter comes from astronomy, there are a variety of measurements all leading to a similar conclusion. The sources of evidence include: the rotational velocities of spiral galaxies, analysis of superclusters of galaxies, the power spectrum of the Cosmic Microwave Background (CMB), models of Big Bang nucleosynthesis (BBN) limiting baryonic contribution to the makeup of matter in the universe, and Baryon Acoustic Oscillations (BAO). A detailed discussion of this evidence is outside of the scope of this dissertation, but the resultant theory of cosmology, ΛCDM, incorporates some dark energy (Λ) and cold dark matter (CDM) and suggests that we know surprisingly little about the vast majority of the universe.

The Weakly Interacting Massive Particle (WIMP), with mass $\mathcal{O}$(GeV–TeV) and interaction cross-section on the weak scale, is a strongly favored CDM candidate motivated by Supersymmetric (SUSY) extensions of the standard model [38]. The WIMP-nuclear cross-section is constrained by SUSY and interactions with nucleons are expected to present the best opportunity for direct dark matter detection if the majority of dark matter is made of WIMPs [38]. The cross-section may be spin-dependent or spin-independent. In the spin-independent case the WIMP would coherently scatter with all nucleons of a nucleus, similar to CENNS. In both cases the resultant signal is a nuclear recoil.

The portion of the scientific community focused on direct detection of dark matter have constructed low-background detectors focused on identifying very rare nuclear recoils and distinguishing them from other backgrounds. The effort to detect CENNS is, as a result, very similar to that of direct WIMP searches. One difference is the expected recoil energies. Favored WIMP masses will result in nuclear recoils $\sim \times 10 - 100$ higher in energy than signals from CENNS, however the majority of signals will pile up at lower energies. As a result, CENNS searches have adopted similar technologies as those used in these WIMP searches and focused on lowering the threshold of such devices. The efforts presented in this dissertation are directed towards studying the signals from low-energy nuclear recoils and calibrating these detectors at low energies. The findings presented here are therefore also relevant to the direct dark matter search community.

1.2 Monitoring of Nuclear Reactors for Nuclear Safeguards

While the nuclear fuel cycle is capable of producing clean power for humanity, many of the technologies used throughout this fuel cycle may be exploited for the development of nuclear weapons (Fig. 1.7). This recognition, and knowledge of the horror that nuclear weapons can so easily deliver, led nearly every country in the world to sign and ratify the Treaty on the Non-Proliferation of Nuclear Weapons, often referred to as the NPT. This treaty is built upon three pillars: non-proliferation, disarmament, and the peaceful use of nuclear energy. Under this treaty, non-nuclear weapons states (NNWS) are acknowledged an inalienable right to use nuclear energy for peaceful purposes. The NNWS also agree to accept safeguards from the International Atomic Energy Agency (IAEA) to verify that nuclear energy program within their country is being used for peaceful purposes and no materials or technologies are being diverted for production of nuclear explosives or weapons. In exchange, the nuclear weapons states (NWS) agreed to not transfer weapons or weapons technology to NNWS, negotiate in good faith to cease the nuclear arms race, and negotiate in good faith towards disarmament with the goal being a treaty on general and complete disarmament.

To enforce the NPT, the IAEA enacts a variety of technical measures called safeguards to verify that no materials or technologies are being diverted from peaceful nuclear energy programs to covert nuclear weapons programs. While safeguards are deployed by IAEA inspectors at facilities across the fuel-cycle, the safeguards placed at nuclear reactors are important for this work. During operation of nuclear reactors successive neutron capture events in the fuel breeds plutonium and other transuranics. While the quality of plutonium within spent nuclear fuel is not weapons grade, the intentional short-term irradiation of fuel assemblies might be used to produce weapons grade plutonium. Such behavior is in violation of the NPT and IAEA safeguards are set in place to prevent inappropriate irradiation or diversion of fuel assemblies. Though current safeguards do measure the power of the reactor core, such measurements are indirect and infer this quantity from temperature or flow. No safeguard, at present, directly quantifies the amount of plutonium produced during reactor operation. As explained in Sec. 1.1, the $\bar{\nu}_e$ signal from nuclear reactors is directly related to the power and composition of the core. Near-field $\bar{\nu}_e$ detection provides a direct measure of the isotopic fission rates within the reactor core, and combined with knowledge about the reactor design enable calculation of plutonium content within the core. Such measurements are currently unavailable to IAEA inspectors and would help to improve detection of plutonium diversion at downstream reprocessing facilities. Additionally, $\bar{\nu}_e$ detection is inherently non-intrusive and continuous, making it well suited for remote monitoring.

Reactor monitoring with $\bar{\nu}_e$ has been demonstrated using the inverse beta-decay reac-

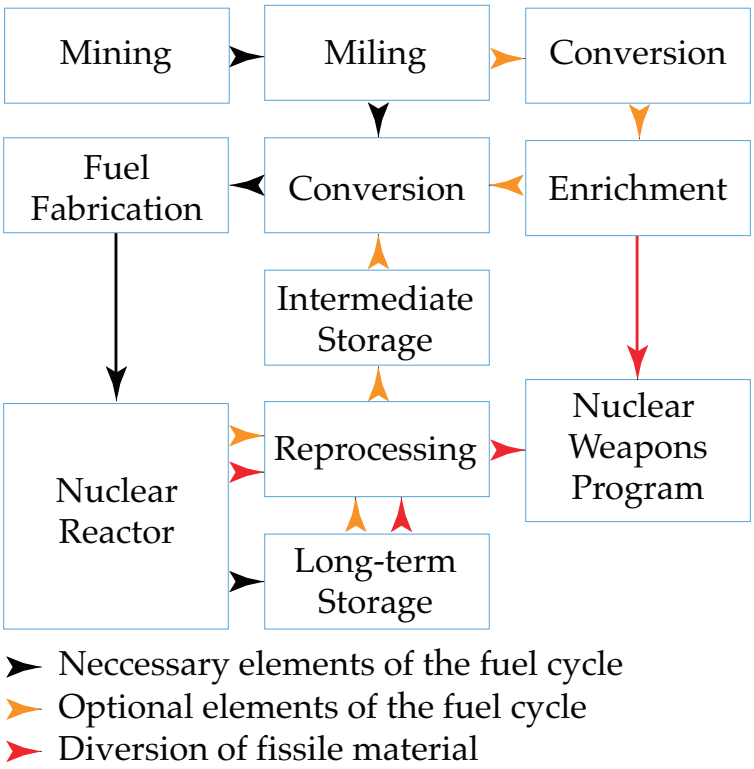

Figure 1.7: Nuclear fuel cycle and primary diversion opportunities. Figure adapted from [72]

tion [2, 18]. In recent demonstrations $\bar{\nu}_e$ monitoring has been able to successfully monitor the isotopic evolution of fuel in a reactor, detect on-off status . Figure 1.8 shows $\bar{\nu}_e$ detection rate compared to thermal power of a reactor as reported by the operator. The slow degradation of rate is associated with the ingrowth of plutonium in the core and burn-up of ^{235}U and enables quantification of plutonium ingrowth. While successful, these inverse β-decay detectors are large $\mathcal{O}$(few m^3). One opportunity for shrinking $\bar{\nu}_e$ reactor monitoring detectors is to detect CENNS rather than inverse β-decay. The cross-section of CENNS is $\mathcal{O}(\times 100)$ larger, suggesting smaller detectors would be capable of detecting similar rates of $\bar{\nu}$ interactions. As a result, investigation of the energy thresholds of dual-phase argon detectors will shed light on whether such detectors may be useful for nuclear safeguards.

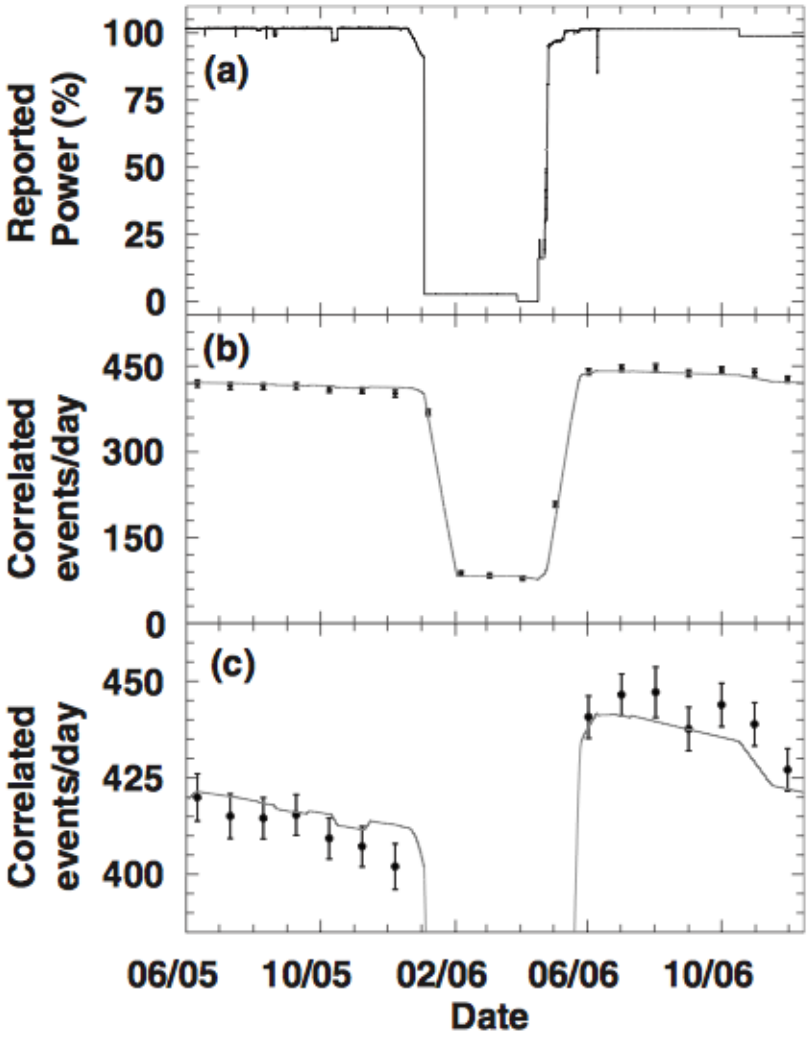

Figure 1.8: Figure from [18]. (a) Reactor power reported by the operator. (b) Observed correlated event rate (inverse-β decay signal) from the detector and predicted rate based upon a rolling average of the burn up model. (c) Same as (b) but expanded y-axis.

1.3 Dual-Phase Noble Element Detectors

Dual-phase noble element detectors, in particular argon and xenon, provide scalable low-background volumes with the ability (in some circumstances) to discriminate nuclear recoils from electron recoils (e.g. Compton electrons) [52]. The large electron lifetimes within the liquid enable scalable monolithic detection volumes and the scintillation properties of the liquid (prompt scintillation or S1) and gas (electroluminescence or S2) enable operation as time-projection chambers (TPCs) [55]. The ability to fiducialize these monolithic volumes provides an actively self-shielded central volume ideal for rare-event searches. A comprehensive review of this technology and its applications to rare-event searches may be found in [23]. In this section I briefly discuss the operating principles of dual-phase argon detectors, the general properties of liquid argon, energy deposition and excimer scintillation in liquid nobles, and provide an overview of experiments that have characterized the nuclear recoil response of liquid argon.

Dual-phase detector design

In a dual-phase detector an electric field is applied across the liquid target ($\mathcal{E}_d$). When some radiation interacts within the target, prompt scintillation light is emitted (referred to as S1) and ionization electrons are collected by the applied field. The electrons are drifted to the liquid-gas surface and, with a strong enough applied field [16], extracted across this interface into the gas. Under the influence of an electric field in the gaseous volume ($\mathcal{E}_g$), electrons produce scintillation via electroluminescence as they drift to the anode. The scintillation signal produced during electroluminescence is often referred to as secondary scintillation or S2. This process, the general layout of dual-phase detectors, and a schematic view of the S1 and S2 signals, is illustrated in Fig. 1.9.

The (z) position of the interaction may be calculated from the time required to drift the electrons to the gas volume under a known applied drift field. The (x, y) position of the interaction can be resolved when viewing the S2 signal with an array of photo-detectors. In this way the dual-phase detector functions as a time-projection chamber and can resolve the (x, y, z) coordinate of an interaction and use this information for background rejection. In some detectors additional reflective (or wavelength shifting) materials are included around the walls of the detector volume to increase light collection. Arrays of photo-detectors may be deployed above a transparent, below a transparent cathode, or both.

The Properties of Liquid Argon (LAr)

Liquid argon (LAr) has long been used for particle detection via charge collection in the calorimetric drift chambers of high energy colliders. As a result, the electronic drift

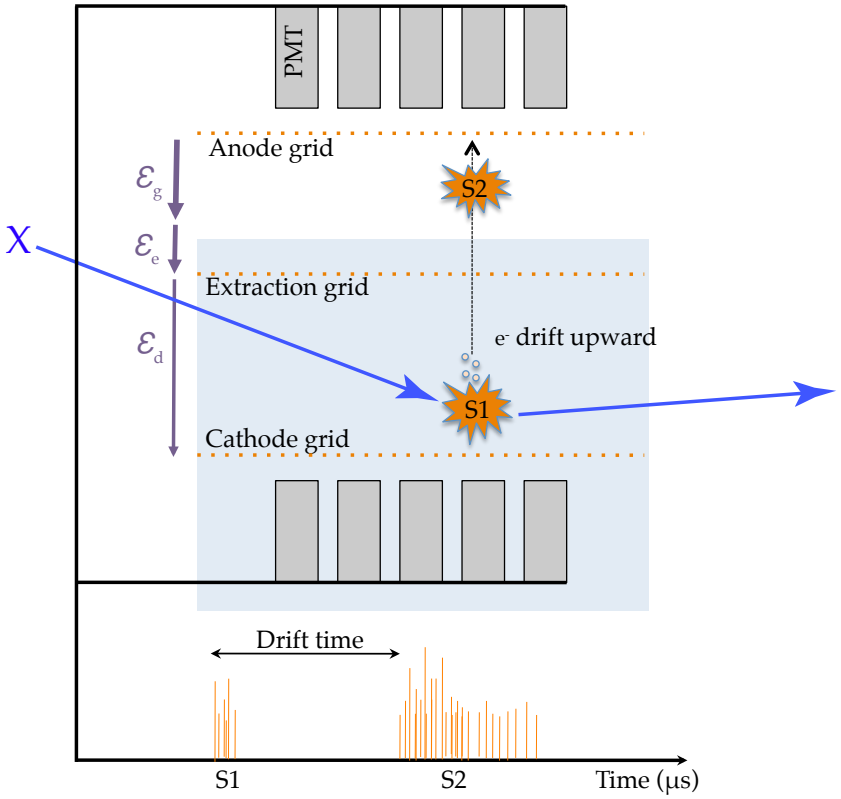

Figure 1.9: Schematic of dual-phase noble element detectors. Some particle χ interacts within the liquid target volume producing prompt scintillation (S1) and ionization. The ionization is separated with the drift field ($\mathcal{E}_d$), extracted into the gas with the extraction field ($\mathcal{E}_e$), and drifted across the gas gap producing electroluminescence (S2) in the gain field ($\mathcal{E}_g$). Scintillation photons from S1 and S2 are detected by PMTs. The time separating the start of S1 and S2 indicates interaction depth (z) and the distribution of S2 light within a PMT array indicates (x, y).

properties of liquid and gaseous argon have been well characterized [69]. More recently, the discrimination power of primary scintillation to distinguish between nuclear and electron recoils for $\mathcal{O}(50\text{keV})$ has prompted interest in this medium for direct WIMP dark matter searches [17]. The noble nature of argon allows excellent electronic drift properties once sufficiently purified of electronegative impurities, which may be easily performed with commercially available getters. Additionally, its ample natural abundance (0.93%) makes it a relatively inexpensive media for radiation detection, though the cryogenic systems required for liquefaction must also be considered. Table 1.1 lists

Table 1.1: Properties of argon.

Parameter	*Value*
Z	18
A	36,38,40
Molecular weight	39.95
Boiling Point at 1 atm	87.25 K
Density of liquid	1.4 g/cm^3
LAr dielectric constant	1.4–1.6
Scintillation light wavelength (λ)	128 nm

the general properties of argon

The vacuum ultra-violet (VUV) scintillation of argon is challenging to detect directly. Rather, wavelength shifters are often used to shift the 128 nm photons into the visible where traditional PMTs are effective. Tetra-phenyl butadiene (TPB) has been demonstrated to effectively shift argon scintillation into the visible without degrading electron mobility in the LAr [56]. The optimal range of evaporated TPB areal density was shown to be $\sim$ 0.05 mg/cm^2 [56]. A TPB evaporation apparatus was used at PSU to produce TPB coated windows for our experimental effort.

Energy deposition in liquid argon

The partitioning of energy between ionization, excitation, and heat is highly dependent upon the energy and type of particle interacting with the liquid [23]. Following energy deposition, electron-ion recombination plays an important role in determining the observable (extracted electrons and scintillation photons) response to radiation interactions. VUV scintillation light in liquid nobles results from the relaxation of the two lowest electronic excited neutral molecules ($^1\Sigma_u^+$ and $^3\Sigma_u^+$), the singlet and triplet excimers. excimers are formed following both the excitation of individual atoms and following charge recombination, but the population of the singlet and triplet states is not necessarily the same from each path [17, 23]. In liquid argon the lifetime of the singlet is measured to be $\tau_s \sim 7$ ns and the lifetime of the triplet is measured to be $\tau_t \sim 1600$ ns [23]. Figure 1.10 illustrates the production of observable signals in liquid argon.

The fraction of ions that recombine is related to the spatial distribution of ions and electrons following ionization. Recombination may be suppressed with an applied electric field. As the population of singlet and triplet excimers is different when produced via recombination, a difference in the observables (singlet to triplet fraction of prompt scintillation and prompt scintillation to charge fraction) may be expected for different

ionizing particles. This phenomena has been exploited for particle identification, to distinguish electronic from nuclear recoils in liquid argon and liquid xenon. For lower recoil energies the discrimination power of this phenomena decreases, however charge collection may be enhanced (at the expense of scintillation yield) with application of larger electric drift fields. This is attractive because separated charge is collected with $\sim 100\%$ efficiency in these detectors whereas scintillation detection is limited by the quantum efficiency of the photo-detectors. As a result, it is the ionization channel that will provide access to the lowest energy sensitivity of these detectors, eventually arriving at the cost of (z) position reconstruction when S1 is no longer effectively observed.

Nuclear recoil studies in liquid argon

While the response of liquid argon to high-energy particles has been studied in great detail, the response to nuclear recoils < 300 keV has only been explored by a handful of experiments. To date, all experiments studying the nuclear recoil response in liquid argon have investigated the prompt scintillation yield resultant from nuclear recoils. The focus on scintillation is a result of the very high efficiency for particle identification based on the shape (singlet to triplet ratio) of S1 light.

Most of these experiments have used fusion (D-D and D-T) neutrons to induce nuclear recoils within the LAr target volume [20, 63, 39, 52]. In [5] a pulsed ^{7}Li(p,n)^{7}Be neutron source was used to produce high-energy neutrons (604-1600 keV) to induce nuclear recoils in the LAr target volume. To probe lower energy nuclear recoils [63, 39, 52, 5] used liquid scintillation detectors placed at known scattering angles to tag the scattered neutrons, allowing kinematic reconstruction of the nuclei recoil energy. To date,

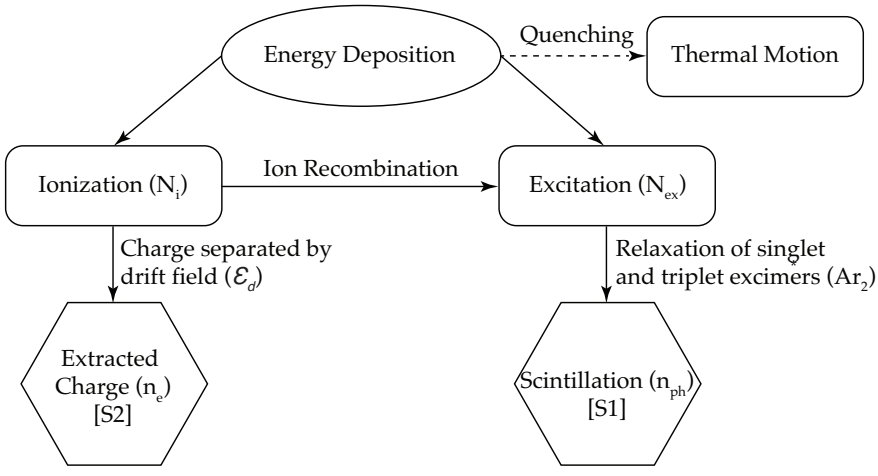

Figure 1.10: Overview of the single production in dual-phase detectors.

the lowest energy nuclear recoils observed were at 10.8 keV using scintillation light [5]. Until the present work, there were no published measurements of nuclear recoil ionization yield. An important challenge in characterizing lower energy nuclear recoils with $\mathcal{O}$(MeV) neutrons comes from the accidental events that arise when tagging neutrons at shallow scattering angles. In Chapter 3 I present the design of a neutron source that can produce quasimonoenergetic neutrons $\mathcal{O}$(100 keV) that was used to circumvent this problem [44]. The first measurement of nuclear recoil ionization yield in liquid argon is presented in Chapter 4 [45], using this quasimonoenergetic neutron source to produce 6.7 keV nuclear recoils.

Chapter 2

The G/NARRLI detector

Gamma or Neutron Argon Recoils Resulting in Liquid Ionization (G/NARRLI) is the small prototype dual-phase argon proportional scintillation counter that was built at LLNL. The name reflects the purpose of the detector: to measure the ionization yield of nuclear recoils in liquid argon (LAr) using Ar(n,n)Ar (Chapter 4) or Ar(γ,γ)Ar (Chapter 5). The ionization yield was focused on because dual-phase proportional counters can achieve single electron sensitivity, making detection of ionization theoretically 100% efficient, while prompt scintillation photon detection efficiency is limited by the geometric coverage of photo-detectors and their intrinsic quantum efficiency. The expected signal for reactor $\bar{\nu}$'s undergoing CENNS in a liquid argon target is only a few ionization and scintillation quanta. As a result, the scintillation quanta would be impossible to distinguish from the dark current present in PMTs.

G/NARRLI was built to achieve stable operation over multiple days and single electron sensitivity so that nuclear recoil ionization yield measurements could be accurately performed. In this chapter, I discuss the the design of the G/NARRLI detector (Sec. 2.1), signal readout (Sec. 2.2), data analysis algorithms (Sec. 2.3), and the calibrations performed to demonstrated performance (Sec. 2.4).

Relevant Publications:

S. Sangiorgio, **T.H. Joshi**, A. Bernstein, J. Coleman, M. Foxe, C. Hagmann, I. Jovanovic, K. Kazkaz, K. Movrokoridis, V. Mozin, S. Pereverzev, P. Sorensen. First demonstration of a sub-keV electron recoil energy threshold in a liquid argon ionization chamber. *Nuclear Instruments and Methods in Physics Research A* **728.0** (2013). [65]

In this article we demonstrated use of ^{37}Ar as a calibration source for dual-phase argon detectors.

2.1 Detector Design

The design of the detector system was done with calibration measurements at beam facilities in mind. The cryogenic and gas handling systems, high voltage supplies for phototubes and detector electrodes, and dual-phase detector were placed on a semi-mobile cart for straight forward transportation between the laboratory in B432 at LLNL and the Center for Accelerator Mass Spectrometry (CAMS) at LLNL. The cart allowed for separation of the detector volume from the electronic noise of the support systems. Additionally, the cart allowed for the detector volume to be rotated around a physically coupled target for exploitation of the neutron source discussed in Chapter 3. A separate electronics cart housed the slow control systems, electronics for signal shaping and event trigger, data acquisition system, and readout computer. A photo of the detector systems is shown in Fig. 2.1.

Figure 2.1: Photograph of the G/NARRLI detector cart and electronics rack

The gas handling system (Fig. 2.2) was built to enable flow control and purification of argon during injection from a standard gas cylinder. A SAES MC1500 getter was used to filter impurities from the argon. Additionally, the system allowed for controlled circulation through the getter during cryogenic operation of the detector, with the circulation pump forcing flow and a flow controller controlling the flow. The slow control software, written in LabView, interfaced with the flow controller to monitor and adjust flow rates. A smaller, secondary gas can was used for injection of ^{37}Ar . This gas cylinder was attached to an expansion volume with a pressure sensor, allowing metered injection of ^{37}Ar from knowing the remaining activity and pressure of gas cylinder.

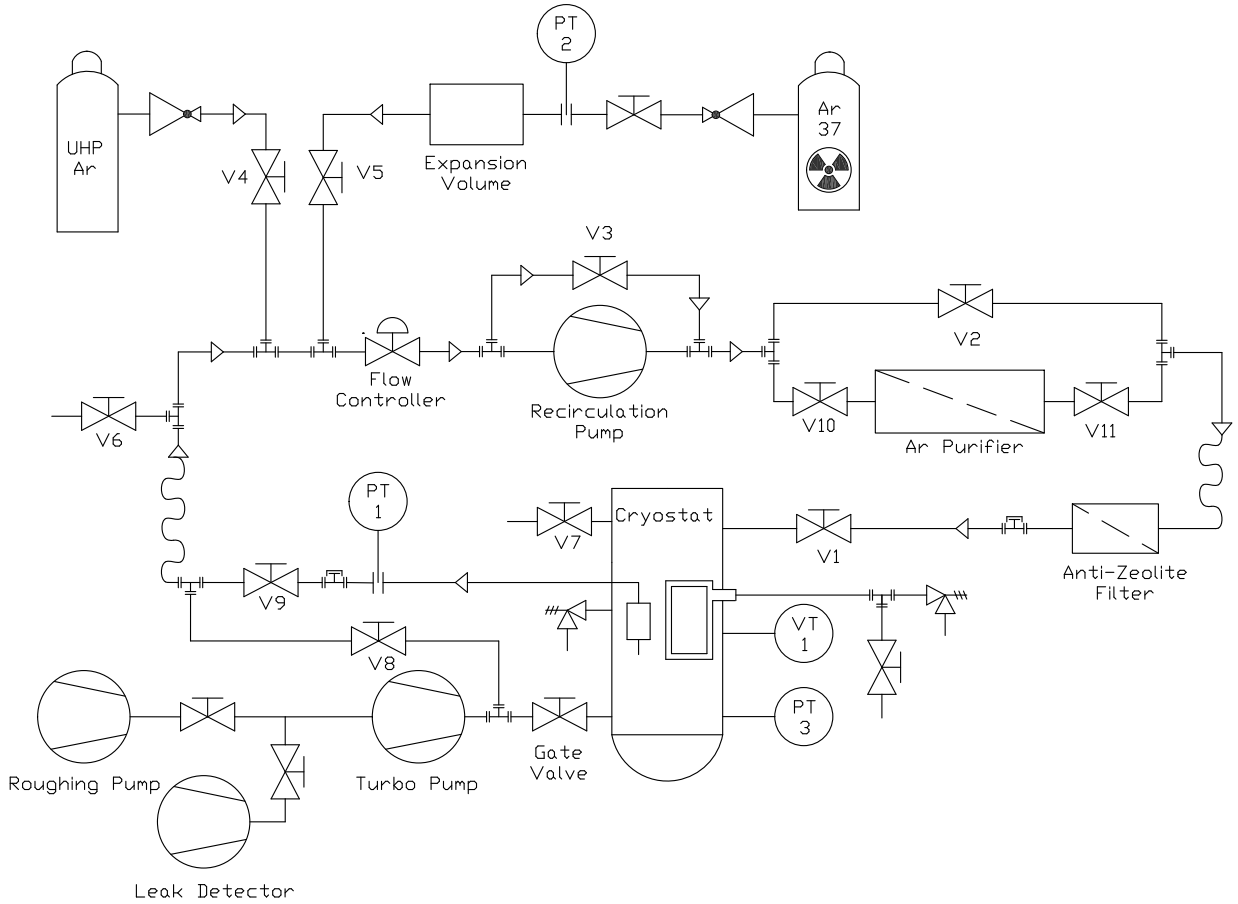

Figure 2.2: Figure courtesy of M. Foxe and T. Gushe. Schematic view of the gas handling system for G/NARRLI. Gas cylinders, circulation, purification, condensation and leak detection components are indicated.

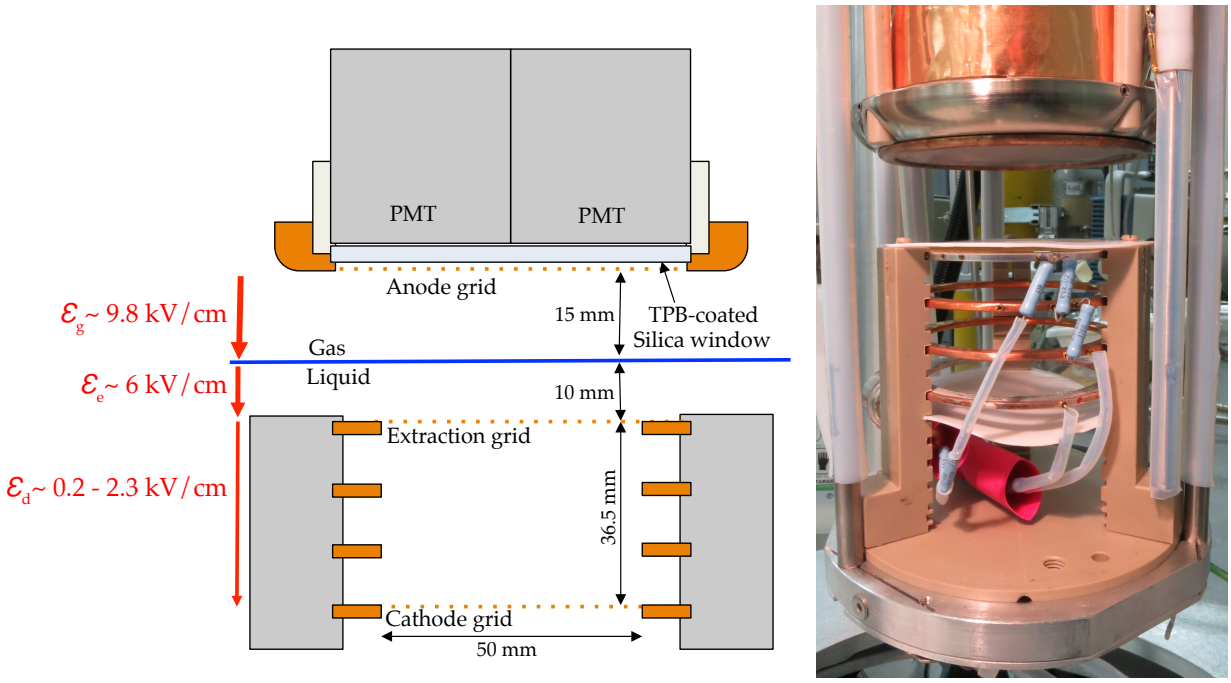

Figure 2.3: Schematic and photograph of the G/NARRLI detector internals.

The detector made use of a cold finger design illustrated in Fig. 2.3. A Q-Drive model 2S132K-FAR cryocooler was attached to the finned copper cold finger, cooling it to 88 K for liquefaction and detector operation. The cryocooler was able to produce 25-30 W of cooling power at 88 K in vacuum. A vacuum jacket surrounded the cold finger internally for IR shielding during operation. Liquid flowed through a tube to the bottom of the cryostat, where it initially cooled the cryostat and eventually condensed. A cylindrical capacitive meter monitored liquid level and triggered the stop of gas injection when the liquid level reached the desired level above the extraction grid.

The small dual-phase detector was built to achieve large gain fields as a means of achieving single electron sensitivity, and focused on the collection of proportional scintillation light. The detector itself was small, to allow external radiation to effectively penetrate to the active volume for calibration. A lower mesh cathode defined the bottom of the detector active volume. Three copper field rings were equally spaced axially, to define and shape the electric field within the detectors liquid target region. The upper of these field rings housed the extraction grid, further defining the field in the liquid target. The mesh anode was attached to the phototube housing 2.5" above the extraction grid. A piece of quartz that was coated on its lower side with evaporated tetraphenylbutadine (TPB) rested 2 mm above the anode, captured by the phototube housing, for the purpose of wavelength shifting argon scintillation light from 128 nm to a 400–480 nm for efficient

detection by the phototubes. A 2x2 array of 1" Hamamatsu 8520 cryo-spec PMTs were held 1 mm above the quartz, viewing the proportional scintillation region from above.

High voltage, applied to the cathode and extraction grid, was brought through cryogenic and vacuum compatible feedthroughs that were designed and fabricated at LLNL. These feedthroughs were tested to -50 kV in LN and operated between -15 and -30 kV during detector operation. A resistor chain between the cathode, field shaping rings, extraction grid, and feedthroughs (Fig. 2.4) was used to define the potential applied to each electrode. The anode was kept at ground.

During normal operation the liquid level was $\sim$ 1 cm above the extraction grid, leaving a 1.5 cm gas gap. At the gain fields operated at during data acquisition, this corresponds to an approximate 2 μs drift time for the charge cloud. The expected duration of S2 events, governed by the drift time across the gas gap and the triplet eximer lifetime in gas ($\tau_s \sim 1600$ ns), was $4 - 20$ μs, depending upon the size of the event. For the range of drift fields explored during normal operation, the maximum drift time range between 10–45 μs.

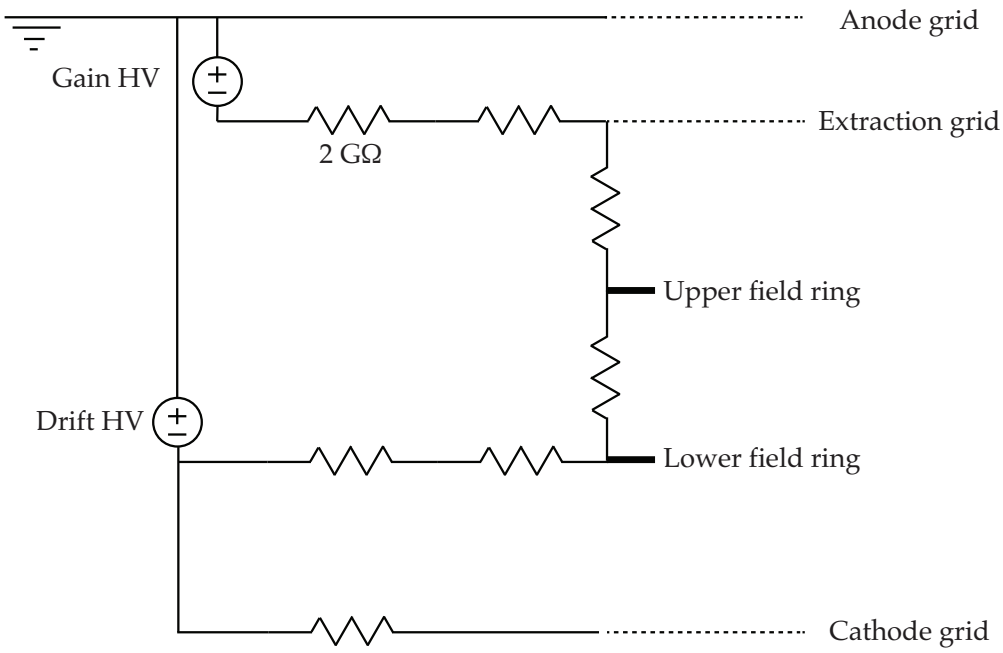

Figure 2.4: High voltage resistor chain used in G/NARRLI.

2.2 Signal Readout

Phototube signals were passed through BNC feedthroughs to exit the cryostat. Signals then passed through a set of NIM based analog electronics to amplify signals and produce a consistent trigger for the waveform digitizing data acquisition system (Fig. 2.5). All four phototubes, Hamamatsu 8520, produced single photoelectron (SPE) response. However one of the four had poor SPE resolution. The SPE peaks along with fits based on the methodology of [6] are shown in Fig. 2.6

The analog trigger, illustrated in Fig. 2.5, produced a trigger when all four phototubes registered a SPE within 10 μs. The LeCroy 428F Fan In/Out was used to reset the signal baseline after the first pass of amplification through the Philips fast amplifier. A veto was produced using the integral of all signals, and passed first through a shaping amplifier then through a discriminator. The veto was extended for 3 ms with a gate generator. This veto was necessary to prevent data acquisition during after-glow or 'grass' that followed very large events (e.g. muons).

Two different waveform digitizing data acquisition systems were used. The first employed a LeCroy WaveRunner oscilloscope. Though effective, this DAQ had a large amount of dead-time associated with data transfer from the oscilloscope to the computer and was only 8 bit. The second, a VME based CAEN V1720, addressed these issues by providing 12 bit data acquisition with $>$ 99% live-time (pre-veto).

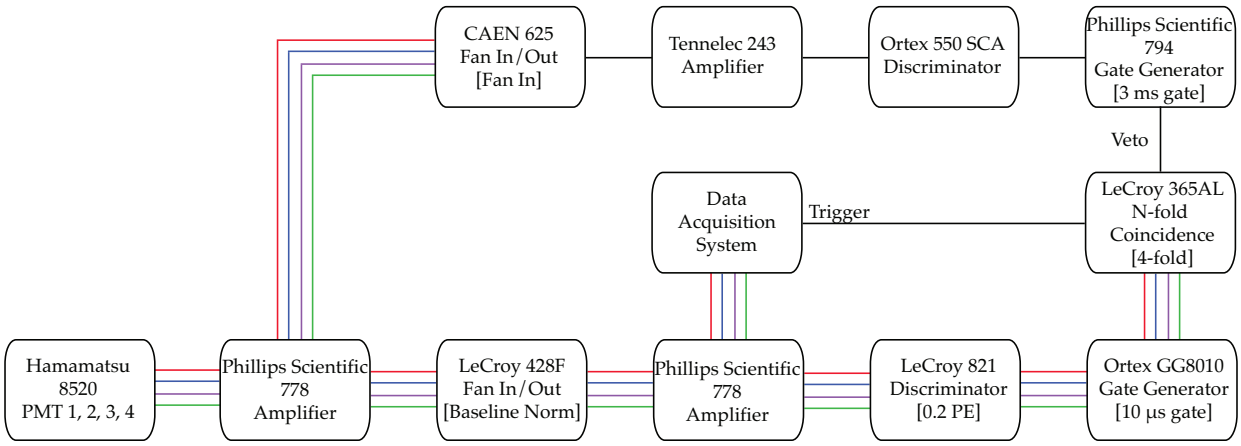

Figure 2.5: Schematic of triggering electronics. The trigger is produced when all four PMTs detect a PE within a 10 μs window.

2.3 Data Analysis

Data was collected as full digitized waveforms from the four phototube channels. Upon each trigger of the acquisition system, a 100 μs trace was digitized. Typically, a 40 μs pre-trigger was included. Figure 2.7 shows an example of a digitized trace of the four phototubes from an 2.82 keV X-ray event from ^{37}Ar . A data analysis package, CNSAnalysis, was written for the analysis of G/NARRLI data. CNSAnalysis was written in C++ using the ROOT data analysis framework [19].

A gate-time analysis [46] was used to identify events within the digitized traces. In this analysis, the detection of a photon within a trace initiates the beginning of a gate. If another photon is observed within the gate-time, τ_g, the gate is extended. This continues until no photons are observed within τ_g of the final detected photon. Multiple events may be identified within a single trace.

Every event identified in the analysis was then entered into a ROOT tree as an instance of an event class. This class contained all relevant information about the event, including trace number, start time, width, τ_{95} (the time taken for 95% of the signal to be detected), integrated charge in each phototube, number of photons detected by each phototube (using an input SPE calibration), whether any digitized points extended be-

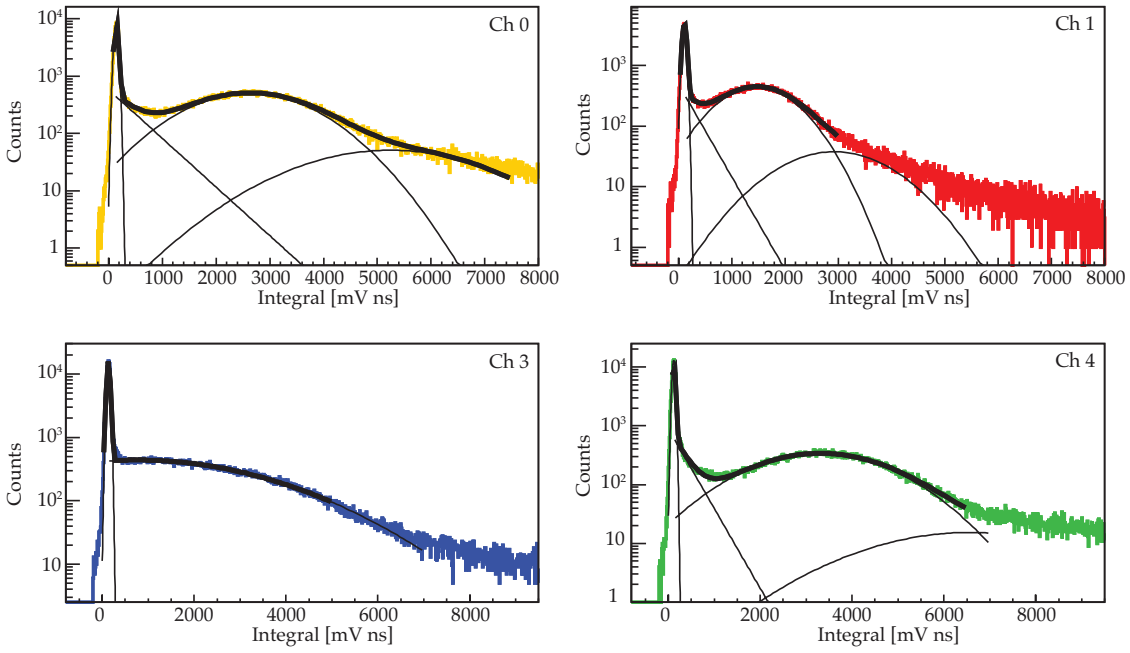

Figure 2.6: Single photoelectron peaks from G/NARRLI PMTs. The fitting function used is described in [6].

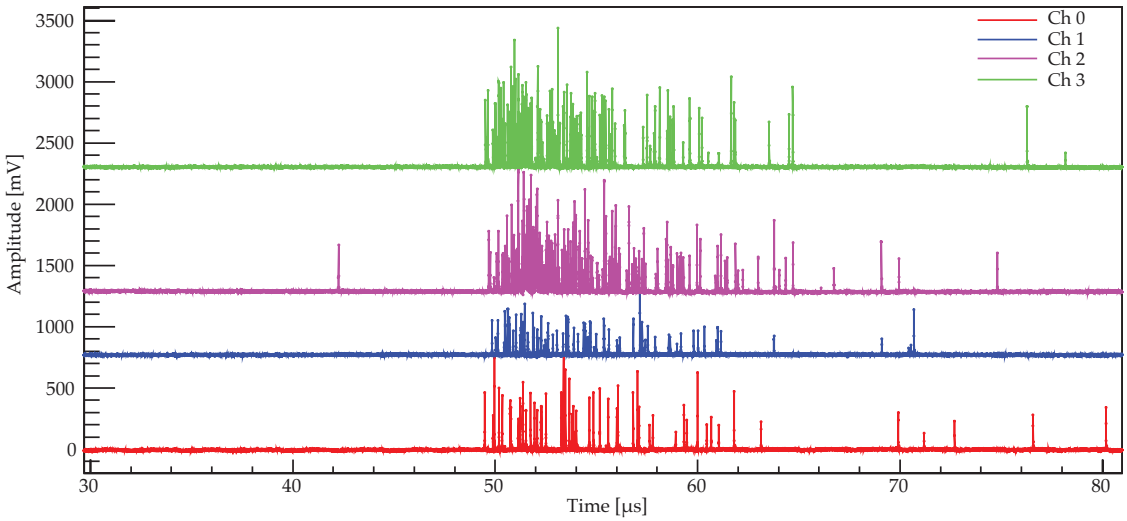

Figure 2.7: Example of a digitized event. A S1 photo was detected ~ 8 μs before detection of the S2 signal.

yond the dynamic range of the data acquisition system, the number of photons detected in the previous and subsequent events, and the fraction of light detected in the first 100 ns. With all events collected in tree form, the analysis and visualization of data could be performed quickly, by applying a series of cuts to the database of events with standard or customized analysis scripts.

Standard Cuts

A set of data quality cuts were applied to the data to ensure consistent analysis of noise-free data. Figure 2.8 illustrates the application of these cuts to ^{37}Ar data.

1. Triggered events were selected by applying a cut to the start time of the S2 event. An event was accepted if it started within 4 μs before the trigger. This cut insured that events had triggered all four phototubes and would be fully digitized. It also assisted in the rejection of primary scintillation events of high energy gammas and multiple scatter events.

2. Events with greater than 10 digitized points that exceeded the dynamic range of the acquisition system were rejected, to prevent incomplete event reconstruction. This was predominantly a problem for the 8 bit LeCroy data acquisition system.

3. S1 events were rejected by excluding any events where more than 10% of the total collected light appeared in the first 100 ns. This is useful in the rejection of periph-

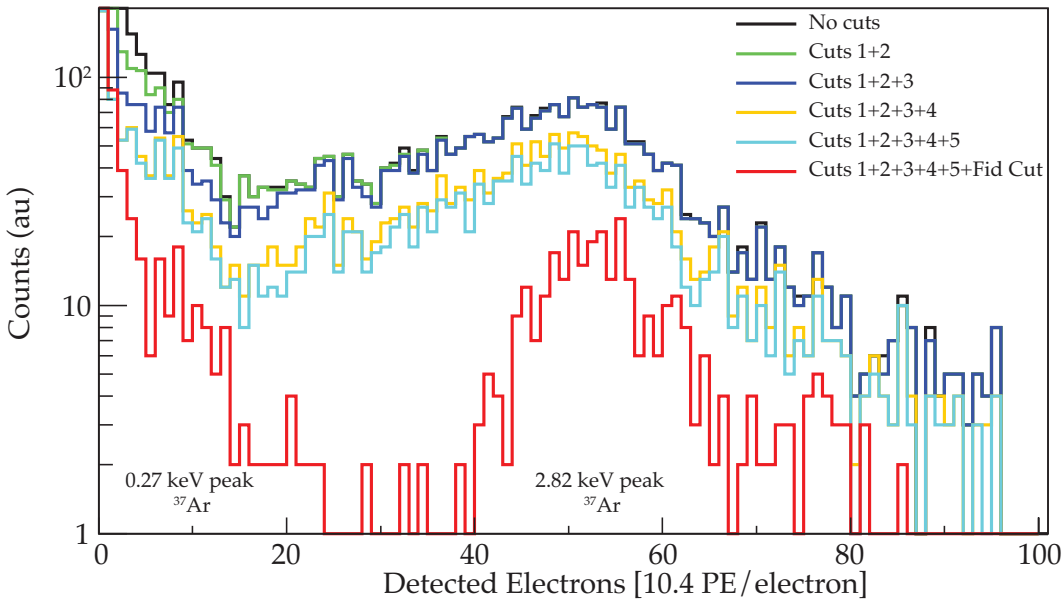

Figure 2.8: Progressive application of standard data cuts to ^{37}Ar data.

eral background events that produce large amounts of primary scintillation but are not within the active target, meaning no S2 signal is observed.

4. When studying low-energy ($<$ 10 keV) signals, isolated events were selected by rejecting events that had significant amounts of light before or after the triggered S2 event. This aided in the rejection of multiple scatter events and spurious light emission following muon events.

5. Multiple scatter events were also rejected by applying a cut of $\tau_{95} < 20\mu$s to the width of events. This cut eliminates axially-separated multiple scatter events, which have multiple charge clouds that arrive at different times, thus extending the width of the event.

Fiducialization

The geometric efficiency of the phototubes varies by $\sim 30\%$ across the active region of the detector. As a result, a fiducializing cut was made to select central events and improve resolution. The fiducial cut uses the normalized ratio of light collected in adjacent pairs of the phototubes (e.g. North/South vs. West/East pairs of phototubes), shown in Fig. 2.9. The normalized ratio was calculated as

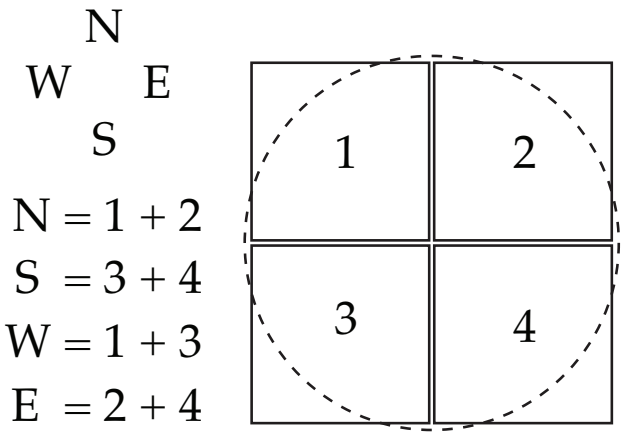

Figure 2.9: Illustration of fiducialization terms used in the fiducial cut. The dashed curve and solid squares indicate the active volume and the PMT positions, respectively. The cardinal directions represent the sum of adjacent PMTs as indicated.

$$\text{If } [N > S] \quad R_{NS} = N/S - 1 \tag{2.1}$$

$$\text{Else} \quad R_{NS} = -1 * (S/N - 1) \tag{2.2}$$

$$\text{If } [W > E] \quad R_{WE} = W/E - 1 \tag{2.3}$$

$$\text{Else} \quad R_{WE} = -1 * (E/W - 1) \tag{2.4}$$

To model this fiducial cut, a numerical model was created. The model first computed the geometric efficiency of each phototube for point-like charge clouds drifting across the S2 gap at different (x, y) positions. The geometric efficiency of the square PMTs for a charge cloud at distance d was determined by adding or subtracting the contribution from different rectangular apertures, where the fraction solid angle, Ω, subtended by rectangular aperture of dimension $a \times b$ is given by

$$\Omega = \frac{1}{4\pi} \arctan \frac{ab}{d\sqrt{a^2 + b^2 + d^2}} \tag{2.5}$$

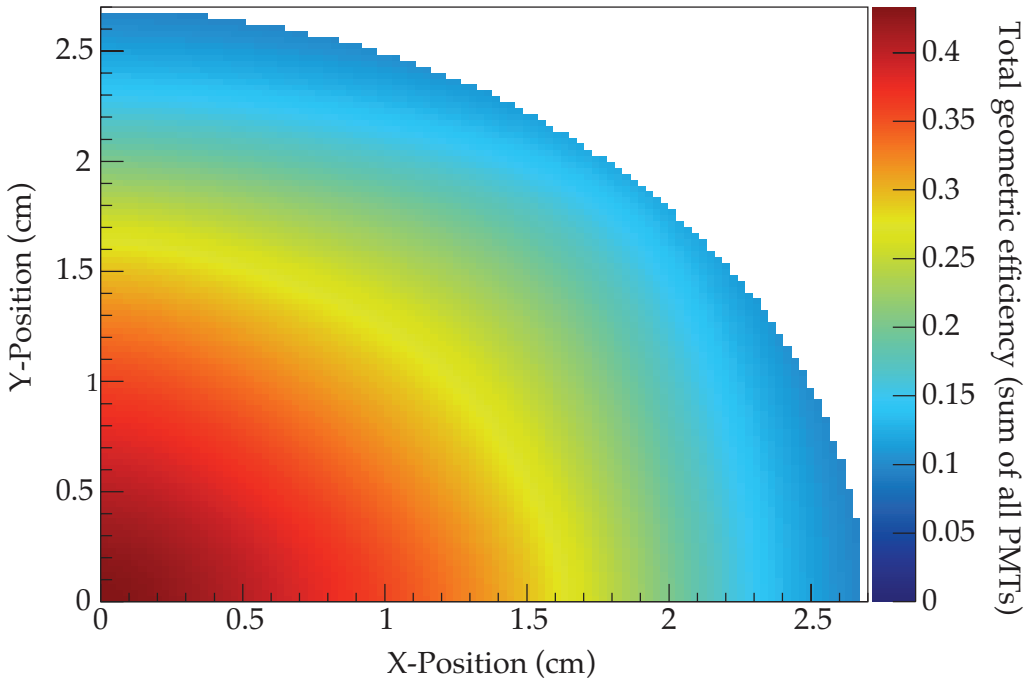

Figure 2.10: Geometric efficiency of the G/NARRLI detector for S2 events from numerical modeling. Sum over all four PMTs.

The efficiency for the entire gaseous drift length was then computed by integrating over the path of the charge cloud. An input single electron calibration value (SPE/e^-) for central ($r < 1$cm) events was entered to determine the light yield per electron drifting across the S2 gap. With this light yield calculated, this class could receive (x, y) coordinates and number of electrons, returning the detected light per phototube. This was done by sampling a binomial distribution, where the geometric efficiency of each phototube corresponded to the probability of success and the number of attempts corresponded to the number of photons produced by the total charge cloud.

Using this numerical model, the optimum cut for selecting events within a circular region corresponded to a diamond-shaped geometric cut within the R_{NS}, R_{WE} phase space,

$$|R_{NS}| + |R_{WE}| < FC, \tag{2.6}$$

where FC is some fiducial cut value. The model was then used to consider the efficiency of fiducial cuts as a function of number of electrons and event location. Figure 2.11 shows the cut efficiency (z-axis) as a function of radial position (x-axis) and severity of the fiducial cut (y-axis) for 10,000 homogeneously sampled events. Each panel corresponds to a different numbers of extracted electrons.

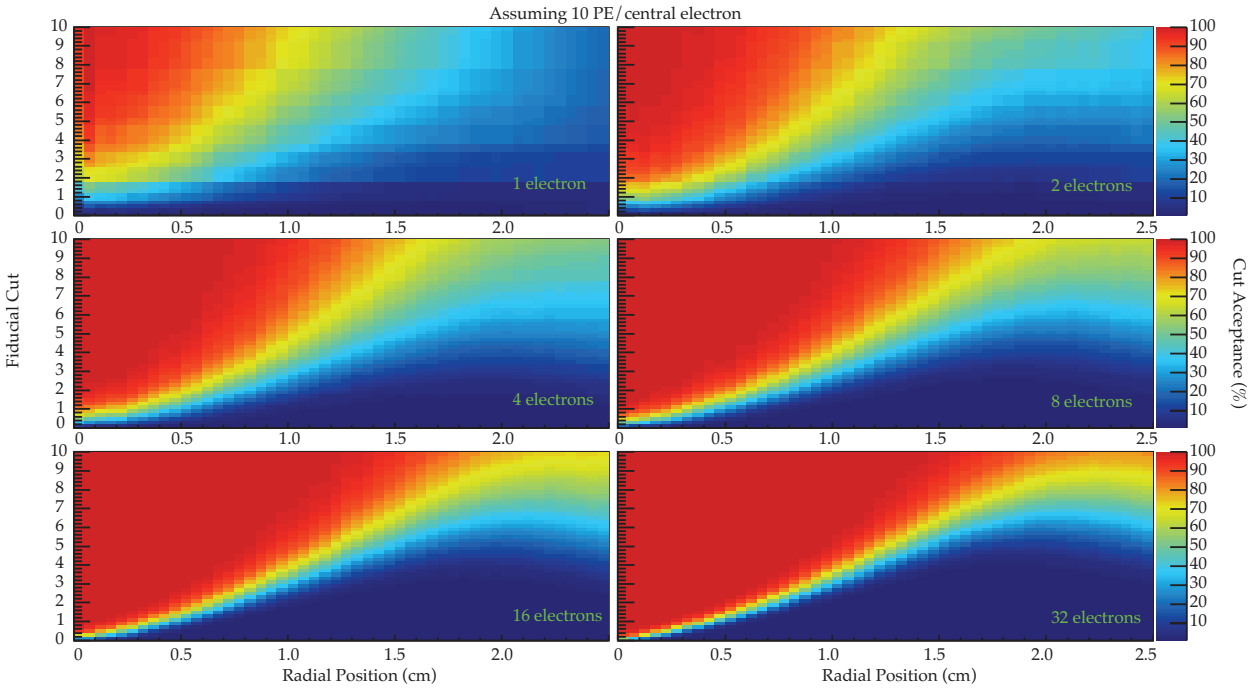

Figure 2.11: Estimation of fiducial cut efficiency using numerical modeling for different numbers of electrons. Cut acceptance given for uniformly sampled events at varying radii as a function of the fiducial cut value (FC). The numerical model uses an assumption of 10 PE per central electron to calculate the mean light yield per unit length for electrons.

2.4 Detector Calibration

Three calibration sources were used throughout detector commissioning: ^{241}Am , ^{55}Fe and ^{37}Ar . The first and last were consistently used throughout the nuclear recoil measurement campaign. The ^{241}Am source (59 keV γ) was used as an external gamma calibration, primarily to measure the electron lifetime within the detector. The electroplated ^{55}Fe (5.9 keV X-ray following K-capture) source was placed directly within the active region of the detector and used as an internal calibration source, providing early validation of the low-energy sensitivity of G/NARRLI. A novel calibration for dual-phase detectors, ^{37}Ar (2.82 [0.27] keV X-ray/Auger from K[L]-Capture) was proposed during early stages of work on this project. Using an argon isotope within the detector enabled a homogenous calibration source to be easily injected.

Table 2.1: Decay emissions from ^{55}Fe . (ENSDF) [74]

Radiation	*Yield (decay^{-1})*	*Energy (keV)*
K-α1 X-ray	1.66×10^{-1}	5.899
K-α2 X-ray	8.46×10^{-2}	5.888
K-β X-ray	3.40×10^{-2}	6.490
L X-ray	6.61×10^{-3}	0.640
Auger-K	6.00×10^{-1}	5.190
Auger-L	1.40	0.610

Measuring Electron Lifetime with ^{241}Am

The 59 keV γ-ray emitted following the decay of ^{241}Am corresponds to high enough energy to effectively penetrate to the central region of G/NARRLI, but low enough energy to interact via photo effect in argon with high probability. This enabled it to be used as a single site photo peak calibration source. The short attenuation length in LAr resulted in a significant fraction of the events accumulating near the periphery of the detector, however the fiducial cut enabled selection of central events as illustrated in Fig. 2.12. Calibration measurements were made with a 300 μCi source that was electroplated on a $\sim$ 3 cm diameter area. This source was collimated, either vertically or horizontally (5 mm gap), using 3 cm thick stainless steel bars.

The large amount of energy deposited produced a consistently observable primary scintillation signal, enabling z-position reconstruction. Using this depth information, a comparison of photo-peak energy with interaction depth provided a means of measuring the electron lifetime (τ_e) within the liquid argon target. Verifying and maintaining high purity of the argon is necessary, because depth correction of low-energy measurements will not be possible due to the low light collection efficiency for primary scintillation. Figure 2.12 shows typical purity data acquired with the vertically collimated ^{241}Am source.

An Internal ^{55}Fe Source

After demonstrating satisfactory τ_e using ^{241}Am , a low-energy calibration was needed. A $\sim$ 200 Bq electroplated ^{55}Fe source, used in calibration of a gas-phase argon detector, was available in the laboratory. ^{55}Fe is a proton rich isotope with a low Q-value (231.21 keV). Due to the low Q-value, decay occurs via an allowed electron capture to ^{55}Mn with $t_{1/2} = 2.747$ yr. The decay emissions are listed in Table 2.1. The X-rays that escape an electroplated source serve as a stable low-energy calibration of $\sim$ 5.9 keV.

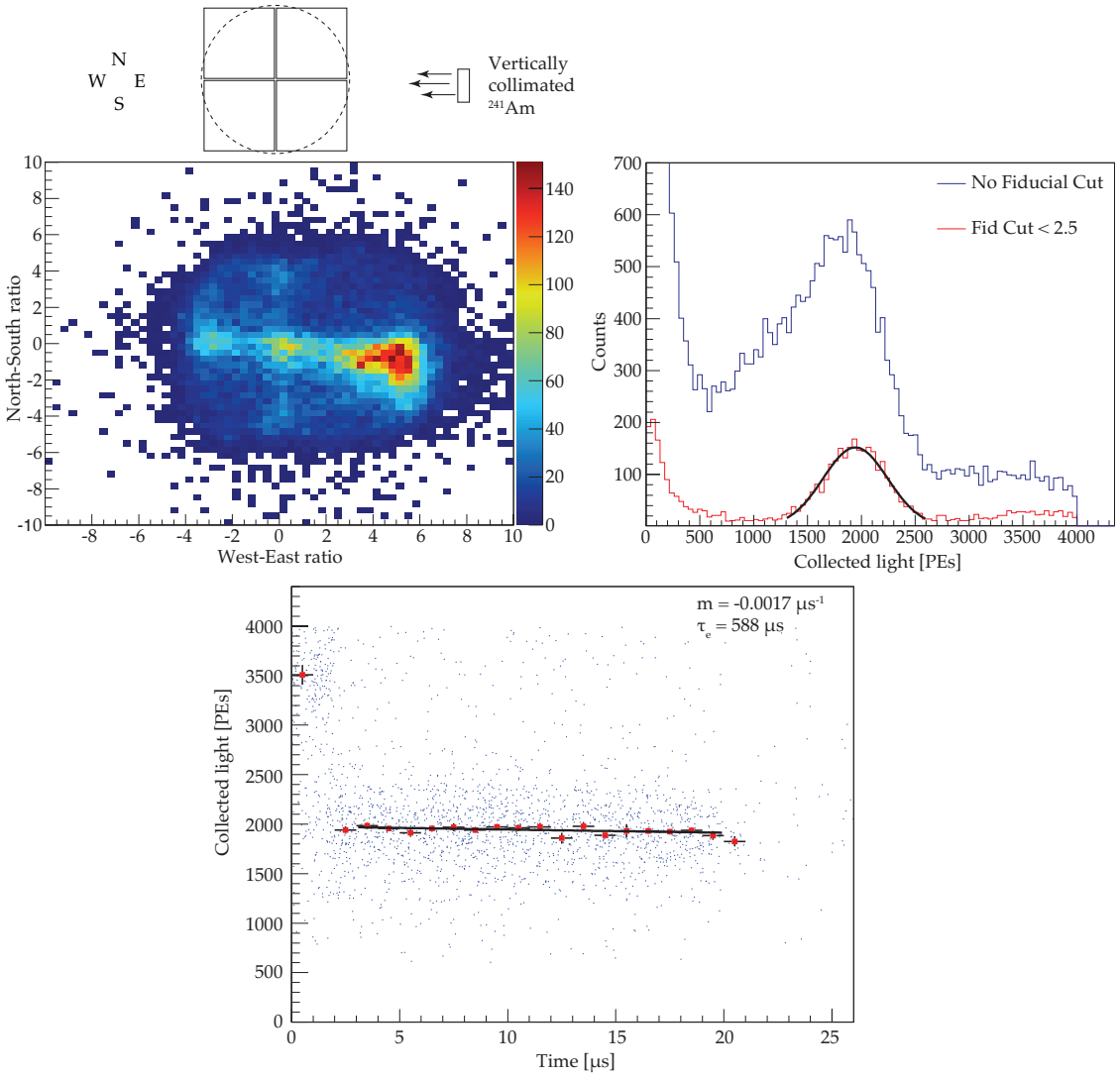

Figure 2.12: (left) Fiducial phase space (R_{NS}, R_{WE}) for ^{241}Am data. A vertically collimated ^{241}Am source irradiated the detector from one side as indicated in the schematic drawing (top down view). (right) ^{241}Am spectra before and after fiducial cut. (bottom) Scatter plot of detected light vs S1-S2 drift time for 59 keV photoelectric events. A fit to this scatter plot measures electron lifetime in the liquid.

A magnetically movable PTFE mount was made to hold the ^{55}Fe source within the active region of the detector and allow radial motion of the source. The source was held at equipotential, with the adjacent field ring using a thin copper wire. Figure 2.13 shows a photograph of the ^{55}Fe calibration assembly within the detector. No problems were encountered during thermal cycling of the setup, and high voltage stability was attained

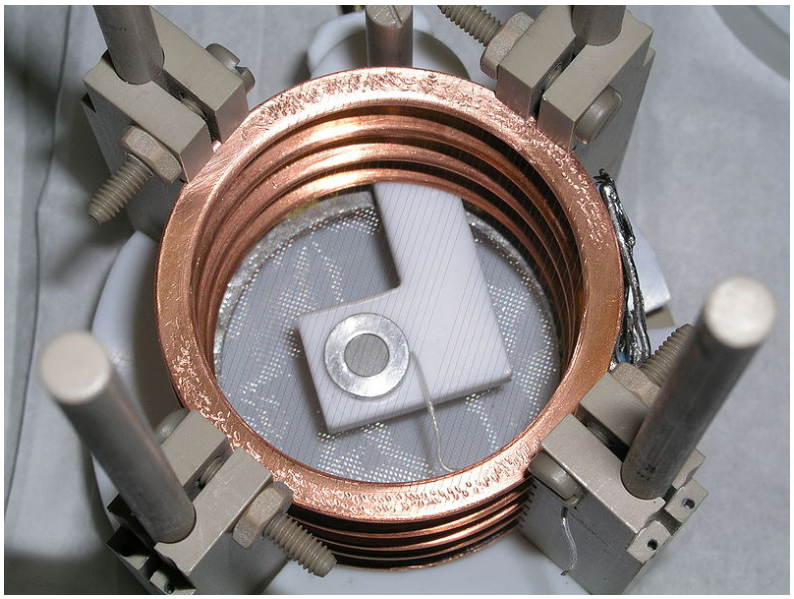

Figure 2.13: Photograph of the ^{55}Fe source and holder within the field cage.

during several cool downs. Figure 2.14 illustrates signals from 5.9 keV X-rays and the efficacy of the fiducial algorithm when the radial position of the source is moved.

Single electrons during ^{55}Fe data taking

During operation of the detector with the ^{55}Fe source installed, there were occasional discharges within the detector. At that point in development of G/NARRLI, this was not an uncommon occurrence and following a discharge stability was regained without tripping the high voltage supplies. What was uncommon, however, was the observation of single electrons following the return to stability. These events had the appropriate time structure of S2 events, as opposed to S1 events, and produced an observable peak in the spectra (Fig. 2.15) that was invariant with shifts to the drift field but scaled appropriately with the gain field (Fig. 2.15). The identification of these events and extensive data taking during their presence enabled single electron calibration of the detector in various configurations, which in turn allowed transformation of data from SPE to detected electrons. An example single electron event is shown in Fig. 2.16.

Using ^{37}Ar as a Homogenous Calibration

Like ^{55}Fe , ^{37}Ar is an isotope that decays via electron capture (Q=813.5 keV and $t_{1/2} =$ 35.04 days). Table 2.2 lists the energy release from different ^{37}Ar decay modes. Detailed

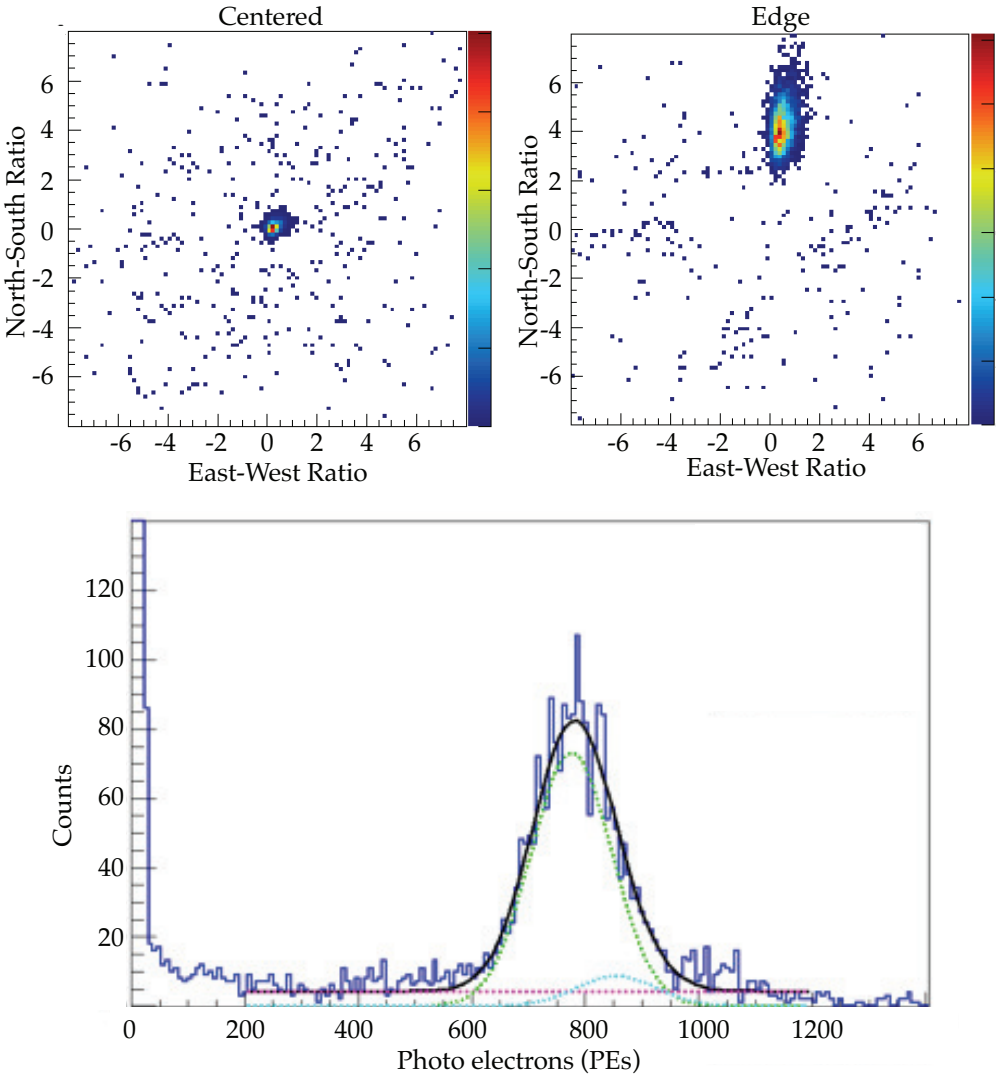

Figure 2.14: Fiducial phase space with ^{55}Fe source centered (left) and at the detector edge (right). Spectra with the ^{55}Fe source centered shown at bottom.

study of the ^{37}Ar decay [12] showed 2.82 keV release per K-capture (90.2%) and 0.27 keV release per L-capture (8.9%), where energy is released in the form of X-rays and Auger electrons.

The idea of using ^{37}Ar as a calibration for G/NARRLI came about during the NE230 course, while discussing noble element monitoring for the Nuclear Test Ban Treaty verification. After proposing this idea within the collaboration, we began discussions with McClellan Nuclear Research Center about the production of a 30-40 μCi ^{37}Ar gas source. Irradiations were performed in the gas irradiation target within the TRIGA reactor. This

target is often used for production of ^{41}Ar, and production of ^{37}Ar follows the same procedure of irradiation of ^{nat}Ar with thermal neutrons from the reactor. The activated sample was allowed to cool over the weekend, to let the ^{41}Ar decay away, before being transported from MNRC to LLNL.

As illustrated in Fig. 2.2, the ^{37}Ar source was connected to the gas handling system through an expansion volume with a pressure sensor. The activity of the ^{37}Ar within the expansion volume was calculated as

$$A[t] = \frac{A[t_0]2^{(t-t_0)/t_{1/2}} * V_e}{PN} \tag{2.7}$$

where $A[t]$ is the activity of the ^{37}Ar source at some date t; t_0 is the date of source production; $V_e = 0.0613\text{ft}^3$ is the volume of the expansion chamber; $t_{1/2} = 35.04$ days is the half-life of ^{37}Ar ; P is the pressure of the ^{37}Ar gas canister; and $N = 12$ ft^3/2000 psi is a conversion factor. Once an appropriate activity of ^{37}Ar ($\sim$ 3 kBq) was injected into the expansion volume, the valve to the circulation lines was opened and the circulation pump was used to pull the gas from the volume. The outlet from the detector volume was left closed. Regular argon was used to backfill a portion of the circulation lines and then circulation was turned on for 10-15 minutes, forcing the injected argon through the getter. After circulation was stopped, a period of 15-30 minutes was generally left to allow the detector volume to stabilize.

The ^{37}Ar uniformly distributed within the liquid argon volume and provided a homogenous source of 2.82 and 0.27 keV energy depositions. Calibration spectra shown in Fig. 2.17 show presence of expected lines before and after fiducial cuts. The fiducial cuts improve resolution and reduce rate as expected for a homogenous source. The presence

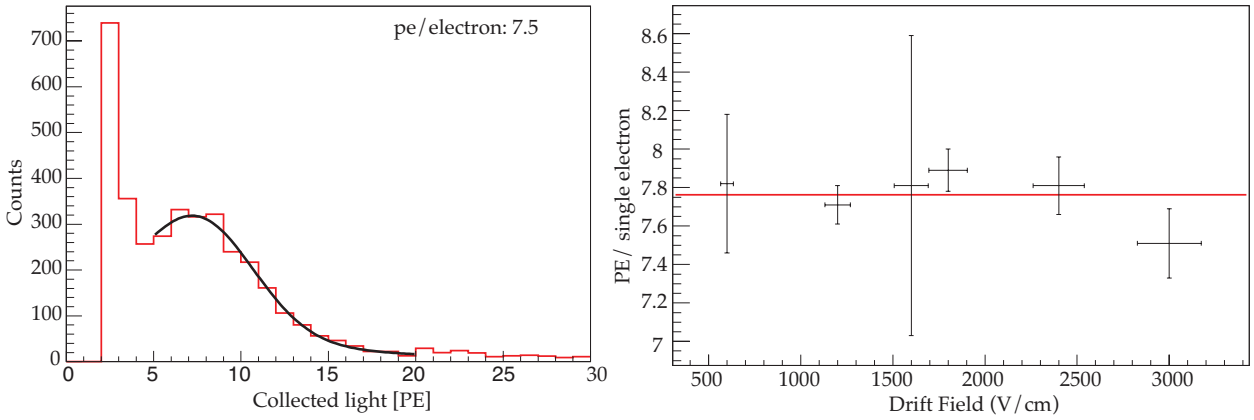

Figure 2.15: (left) Example single electron spectra. (right) Invariance of single electron peak with applied drift field.

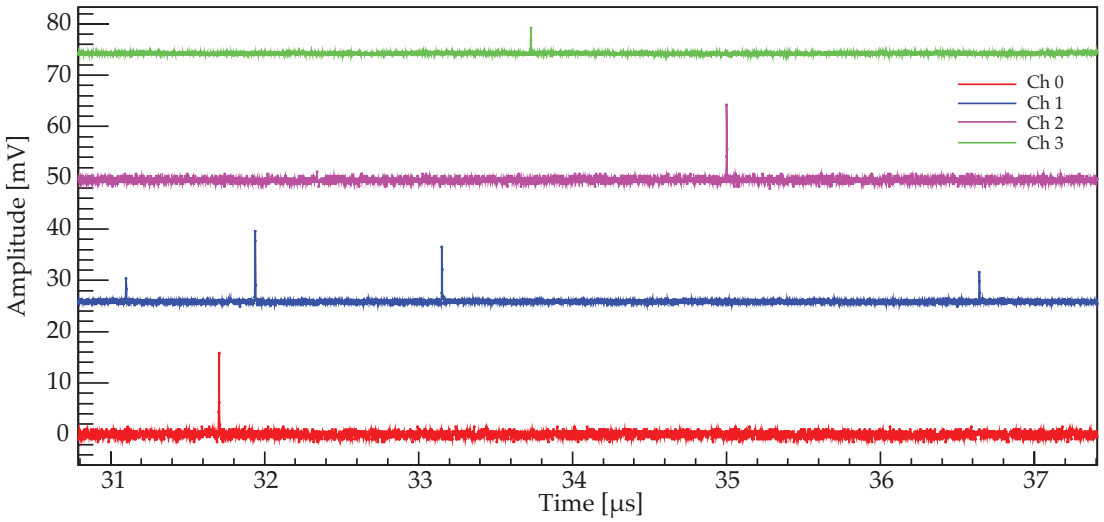

Figure 2.16: Example single electron event.

of single electron data during acquisition with the ^{55}Fe enabled mapping of detected electrons as a function of drift field for the 2.82 keV peak. Figure 2.19 shows the response of the 2.82 keV peak (detected electrons) for varying drift fields. The fit function is an empirical modification [30, 70] to the Thomas-Imel box model [73] that is described in Sec. 4.4.

This data enabled single electron calibration of future data sets, where the single electron peak was not present via introduction of ^{37}Ar and comparison (discussed in Appendix B and used during analysis in Chapter 4). While study of the 0.27 keV line was possible in some data acquired, limiting statistics combined with the exponential background within the detector left it less than ideal for detailed quantitative study.

Table 2.2: Decay emissions from ^{37}Ar . [12].

Decay mode	*Yield (decay^{-1})*	*Energy release (keV)*
K-capture	9.02×10^{-1}	2.822
L-capture	8.90×10^{-2}	0.270
M-capture	1.75×10^{-3}	0.009

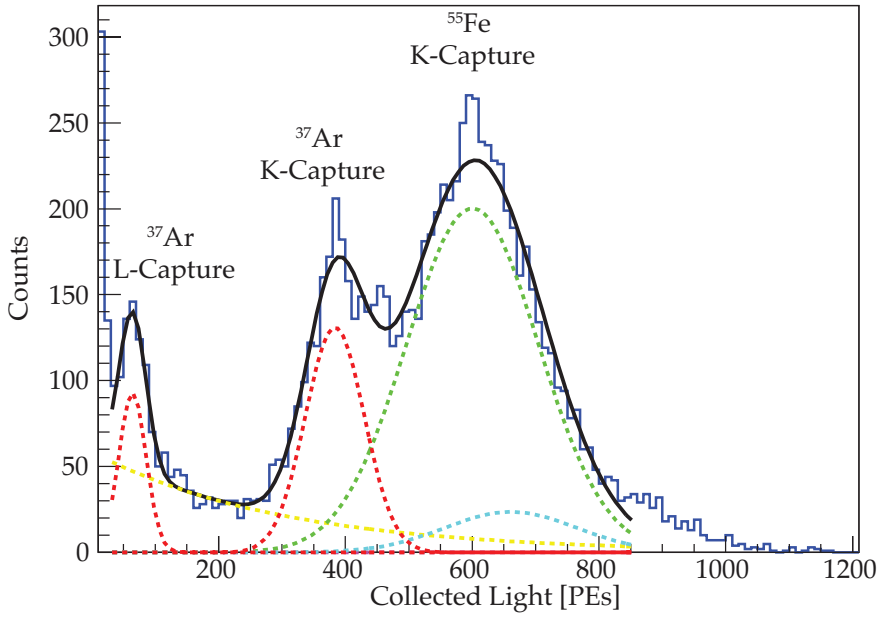

Figure 2.17: High statistics spectra showing the 2.82 and 0.27 keV peaks from ^{37}Ar and the 5.9 keV peak from ^{55}Fe . The non-linear detector response is a result of the variation of electron-ion recombination with energy deposition.

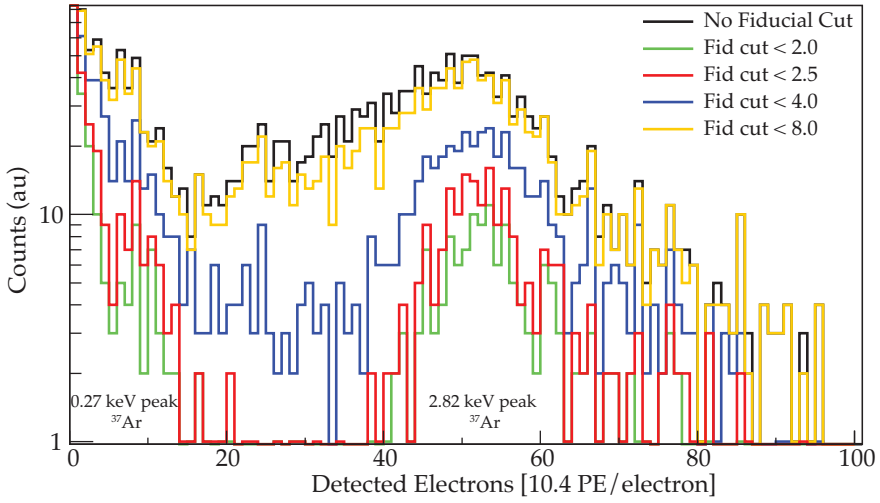

Figure 2.18: Illustration of fiducial cut on ^{37}Ar data.

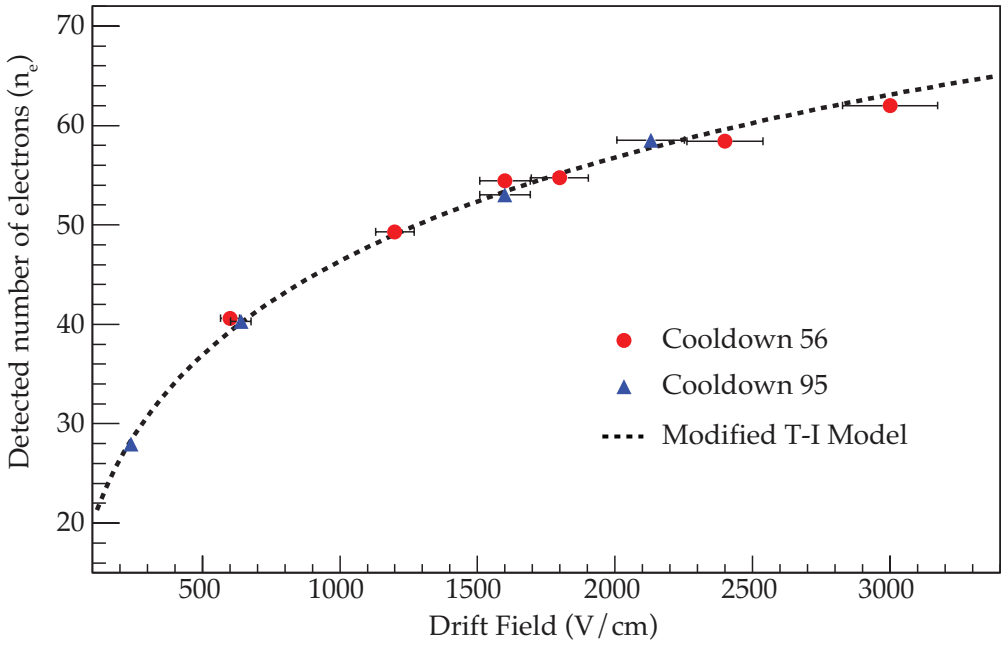

Figure 2.19: Drift field dependance of the 2.82 keV ^{37}Ar peak on applied electric drift field

Chapter 3

Design & Characterization of a Quasi-monoenergetic Neutron Source

The motivation of characterizing nuclear recoil ionization yield required a mechanism for producing known-energy nuclear recoils. Previous measurements of this type have often employed fusion (D-D or D-T) neutron sources to produce high energy neutrons directed at the detector. Scattered high energy neutrons were tagged, often with liquid scintillators, at different scatter angles to trigger data acquisition and kinematically constrain the recoil energy. This approach becomes challenging at shallow angles (low recoil energies). As a result, to characterize low-energy recoils, our group decided to make endpoint type measurements where low energy monoenergetic neutrons are directed at the detector producing nuclear recoils up to a maximum energy. Ionization yield is then measured at this maximum energy. While scattered neutron tagging may be possible, it is quite difficult because the incident neutron energies are below the threshold for traditional liquid scintillators. In this Chapter I present the design and demonstration of the neutron source I designed and that our group built at CAMS.

Relevant Publications:

T.H. Joshi, S. Sangiorgio, V. Mozin, E.B. Norman, P. Sorensen, M. Foxe, G. Bench, A. Bernstein. Design and characterization of a quasi-monoenergetic neutron source. Nuclear Instruments and Methods in Physics Research B (in press). [44]

The text and figures of this paper, of which I was the primary author, are included in this chapter with the permission of all authors. Additional discussion of the installation of the neutron source at CAMS and problems with the Li-target are included in Appendix A.

3.1 Introduction

Characterizing the response of radiation detector media to low-energy $\mathcal{O}$(keV) recoiling atoms, often referred to in the literature as nuclear recoils, is necessary to accurately understand the sensitivity of radiation detectors to light weakly interacting massive particles (WIMPS) [38, 23] and coherent elastic neutrino-nucleus scattering (CENNS) [40, 4, 37, 35, 11]. To produce nuclear recoils of known energy, several different types of experiments have been proposed; the use of monoenergetic neutron sources and tagging the scattered neutron [53, 39, 25], exploiting time of flight and neutron tagging with a pulsed neutron source [5], end-point measurements using a monoenergetic neutron source [41, 24], use of broad spectrum neutron sources and comparison with monte carlo simulations [68], and tagged resonant photo-nuclear scatter [43]. With the exception of the proposal to use resonant photo-nuclear scatter, these experimental designs have all been employed, however successful characterization of sub-keV nuclear recoils has been limited to several results in germanium [11, 42, 41]. A quasi-monoenergetic $\mathcal{O}$(10 keV) neutron source that can be easily constructed at small proton accelerators would enable further characterization of low-energy nuclear recoils in candidate detector materials. More generally, such a source would be useful for characterizing the response of detector materials to $\mathcal{O}$(10 keV) neutrons.

In this article we present the design of a neutron source capable of producing such a beam. The design employs the near-threshold kinematics of the ^{7}Li(p,n)^{7}Be reaction to target resonance interference notches present in the neutron scattering cross-section of certain isotopes. The use of resonance interference notches as neutron filters, only transmitting neutrons within a narrow energy range, has been successfully demonstrated for many years using nuclear reactors [10, 60], however the availability of research reactors instrumented and available for this type of work is limited. Using a nuclear reaction as the source of neutrons allows production of neutron beams with narrow energy spread at proton accelerator beam-lines capable of producing 2 MeV beams.

A prototype neutron source was constructed at the target station of the microprobe beam line at the Center for Accelerator Mass Spectrometry (CAMS) at Lawrence Livermore National Laboratory (LLNL) [64]. In Sec. 3.2 we discuss the characteristics of near-threshold ^{7}Li(p,n)^{7}Be. In Sec. 3.3 we discuss the use of interference notches in iron, vanadium, or manganese as neutron filters. The results from characterization of the neutron source using an iron filter are described in Sec. 3.4 and a discussion of possible low-energy nuclear recoils measurements that may be performed with such a neutron source is included in Sec. 3.5.

3.2 Near-Threshold ^{7}Li(p,n)^{7}Be

The ^{7}Li(p,n)^{7}Be reaction has been extensively studied and used as an accelerator based neutron source thanks to the low Q-value (1.88 MeV) [34]. In the near-threshold regime of the ^{7}Li(p,n)^{7}Be reaction, the incident energy of the proton beam (E_p) establishes a kinematically constrained maximum neutron energy that varies with polar angle (φ) with respect to the incident proton beam. This behavior is evident in the proton energy contours shown in Fig. 3.1. Though solution of the non-relativistic kinematics equations to understand kinematic constraints of neutron production is straight-forward, calculation of the differential neutron yield is non-trivial. In this study we employ the prescription given in [50] for calculation of near-threshold differential neutron yield for protons traversing a Li-loaded target. This methodology was validated in [71]. We make the following reasonable assumptions throughout the article: proton energy loss is constant within the thin targets considered, the incident proton beam is mono-energetic, and target composition is uniform.

Using this prescription we are able to calculate the expected differential neutron yield for any combination of proton beam energy, lithium-loaded target composition, and target thickness. Figure 3.2 illustrates thin target behavior for 53 $\mu g/cm^2$ metallic lithium, 115 $\mu g/cm^2$ lithium oxide, 199 $\mu g/cm^2$ lithium fluoride, 285 $\mu g/cm^2$ lithium carbonate targets computed in 0.250 keV and 0.5° intervals with $E_p = 1.930$ MeV. The areal densities were selected such that lithium areal number density is the same for the four example

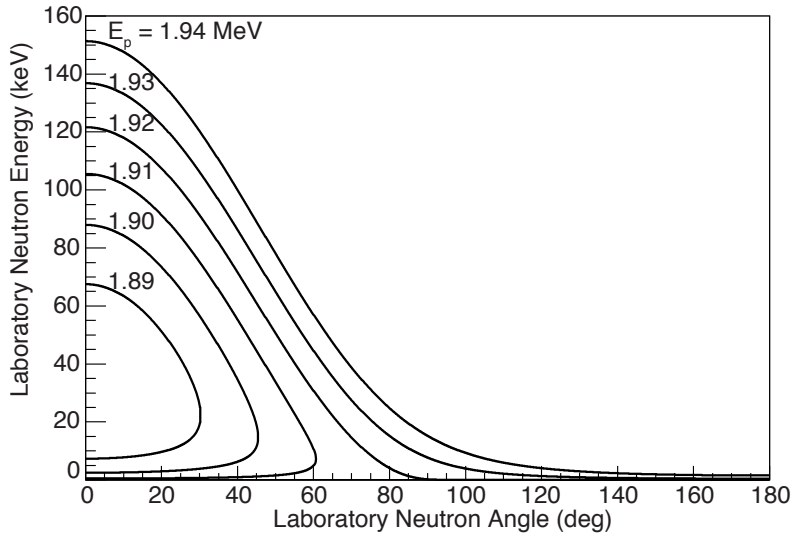

Figure 3.1: Proton energy contours for the ^{7}Li(p,n)^{7}Be reaction near threshold.

targets. Lithium carbonate, though not a traditional target material, is selected because, as discussed in Sec. 3.4, the metallic lithium target used to characterize the neutron source was inadvertently mishandled, resulting in a composition of lithium carbonate. Integrating the differential neutron yield over discrete angles allows comparison of an ideally collimated source with different target characteristics. Fig. 3.2 compares resultant neutron spectra from these thin targets when collimated at 45°. Thin targets have several benefits for production of highly tuned neutron sources. As illustrated in Fig. 3.2, well collimated thin lithium targets may be used to produce neutron beams with small energy spreads by varying collimation angle and/or proton beam energy. As a result, thin targets allow kinematic selection of neutron energies and avoid production of extraneous neutrons (those not produced in the desired energy and angular range), thus limiting the experimental backgrounds associated with neutrons (e.g. elastic and inelastic scatter of neutrons and capture gammas). Additionally, the 478 keV gamma yield from inelastic proton scatter within the lithium-loaded target, ^{7}Li(p,p')^{7}Li, is significantly reduced

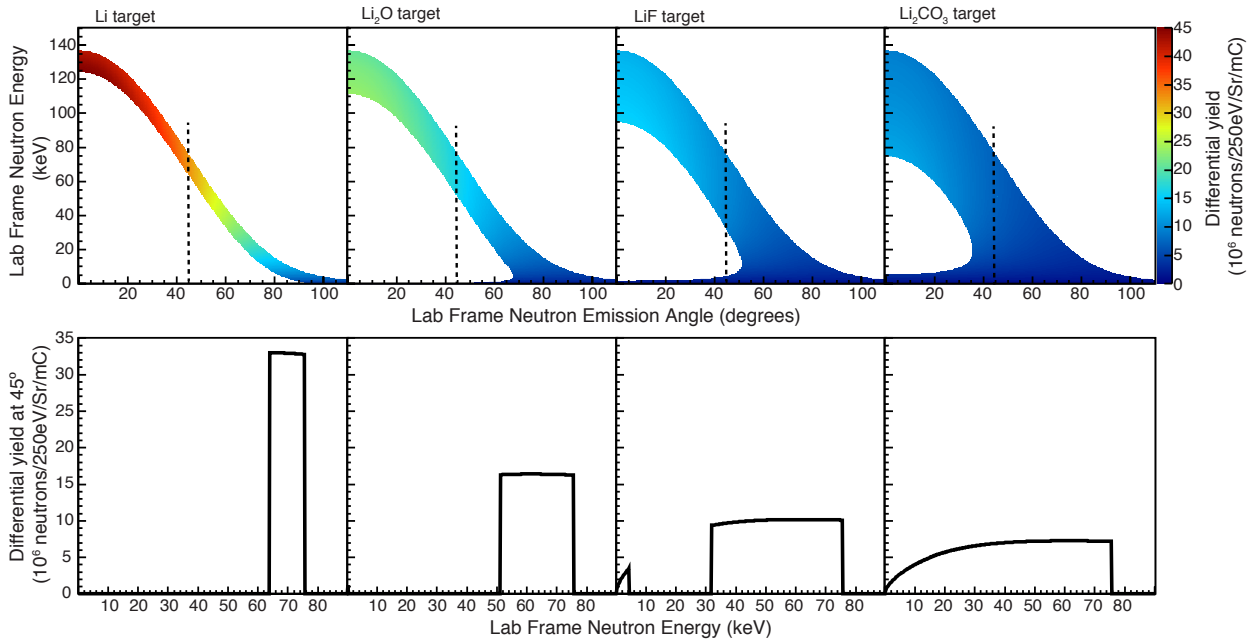

Figure 3.2: Comparison of differential neutron yields for different lithium-loaded targets (Proton energy $E_p = 1.930$ MeV). (top) Calculated differential neutron yield in neutrons/mC/250 eV/steradian and (bottom) ideally collimated neutron spectra at 45° for different thin lithium loaded targets (left to right); 53 $\mu g/cm^2$ metallic lithium, 115 $\mu g/cm^2$ lithium oxide, 199 $\mu g/cm^2$ lithium fluoride, and 285 $\mu g/cm^2$ lithium carbonate. Areal density selected to keep areal number density of lithium constant.

when using thin targets.

For these reasons very thin targets may be quite attractive for some applications, however production, handling, and lifetime of very thin metallic Li targets pose experimental challenges. Very thin targets of lithium oxide or lithium fluoride may be used to ease these concerns, but come at the sacrifice of total neutron rate and increased target stopping power (for equivalent lithium areal number density) which broadens the energy of a collimated beam (Fig. 3.2). It should also be noted that the neutron energy in sources of this type are entirely defined by reaction kinematics and, as a result, are very sensitive to uncertainties in proton energy and angular alignment.

3.3 Filtered Neutron Beams

One approach to utilize the benefits of near-threshold kinematics for production of beams with narrow energy spread (∼10% FWHM), while minimizing sensitivity to uncertainties in proton beam energy and angular location, is the exploitation of narrow

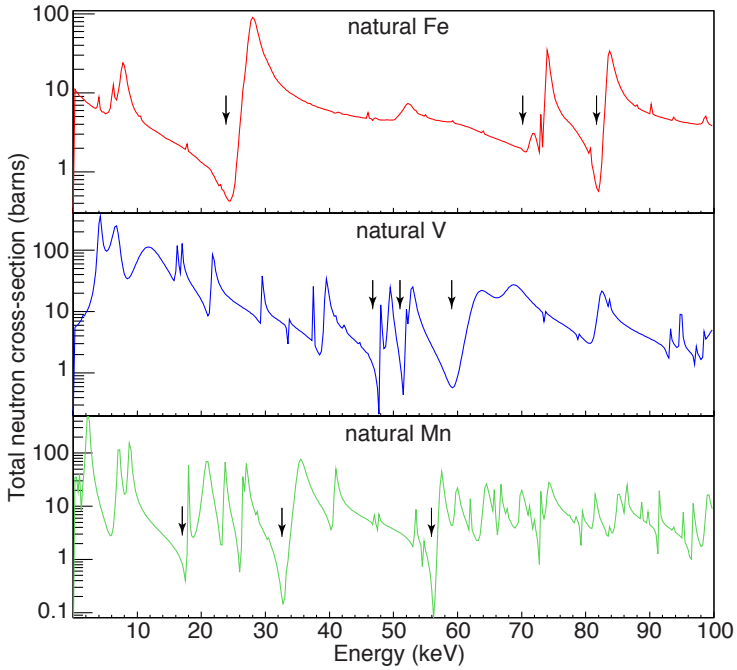

Figure 3.3: Illustration of interference notches in the cross-section of Fe, V, and Mn. ENDF VII total neutron cross-sections for natural compositions of (top to bottom) iron, vanadium, and manganese. Arrows indicate the interference notches that may be used as neutron filters with the near-threshold neutron source.

resonance interference notches in the neutron scattering cross-section of some isotopes. Interference notches selectively transmit neutrons of a particular energy (Fig. 3.3), allowing some materials to serve as a neutron filter. A material endowed with an interference notch at a desirable energy may be used as a neutron filter in combination with a collimated ^{7}Li(p,n)^{7}Be source. Placement of the filter within the collimator aperture and tuning the kinematics of a near-threshold ^{7}Li(p,n)^{7}Be source to target the notch effectively produces a neutron beam with narrow energy spread. The width of the energy spread is dependent upon the properties of the interference notch and the thickness of the filter. The presence of the filter within the collimator also effectively attenuates the 478 keV gammas produced via inelastic scatter in the target, resulting in a quasi-monoenergetic neutron beam with limited gamma contamination.

The sharp maximum neutron energy dictated by reaction kinematics can be used to target specific interference notches. Depending on the presence of lower-energy notches within the filter cross-section, and the thickness of the Li-loaded target, the resulting neutron beam may sometimes be composed of more than one spectral components. To avoid the situation where lower energy notches are filled when targeting higher energies, thin lithium loaded targets may be employed. Alternatively, an additional material may sometimes be identified that effectively out-scatters the lower energy component while allowing some transmission of the higher energy neutrons, and thus be used as a pre-filter.

The 24 keV notch in iron has been characterized for production of neutron beams at nuclear reactors [10]. The 24, 70 and 82 keV notches (Fig. 3.3) in natural iron may be targeted using the approach described here. If targeting the 70 or 82 keV notches with a thick Li-loaded target, a titanium filter may be used in combination with the iron to effectively out-scatter the 24 keV neutrons. Figure 3.4 illustrates the ideally collimated neutron spectra (before and after filtering) when targeting these candidate notches in iron. A lithium carbonate differential neutron yield is used in Fig. 3.4 when illustrating the 24 and 70 keV notches because it was the configuration used to experimentally characterize the neutron source as discussed in Sec. 3.4. Targeting of the 82 keV notch is illustrated with a lithium oxide target.

While iron is an effective neutron filter with several notches, the many naturally occurring isotopes with competing cross-sections limit its performance. An enriched ^{56}Fe filter would perform significantly better than one made with natural iron. Despite this drawback natural iron was selected for experimental demonstration of this work due to availability. Several other materials, such as vanadium and manganese, are also endowed with interference notches that may be targeted with the neutron source described and are both composed of single naturally occurring isotopes. Fig. 3.4 shows several examples of configurations where these filters may be employed to provide narrow neutron beams with a lithium oxide target.

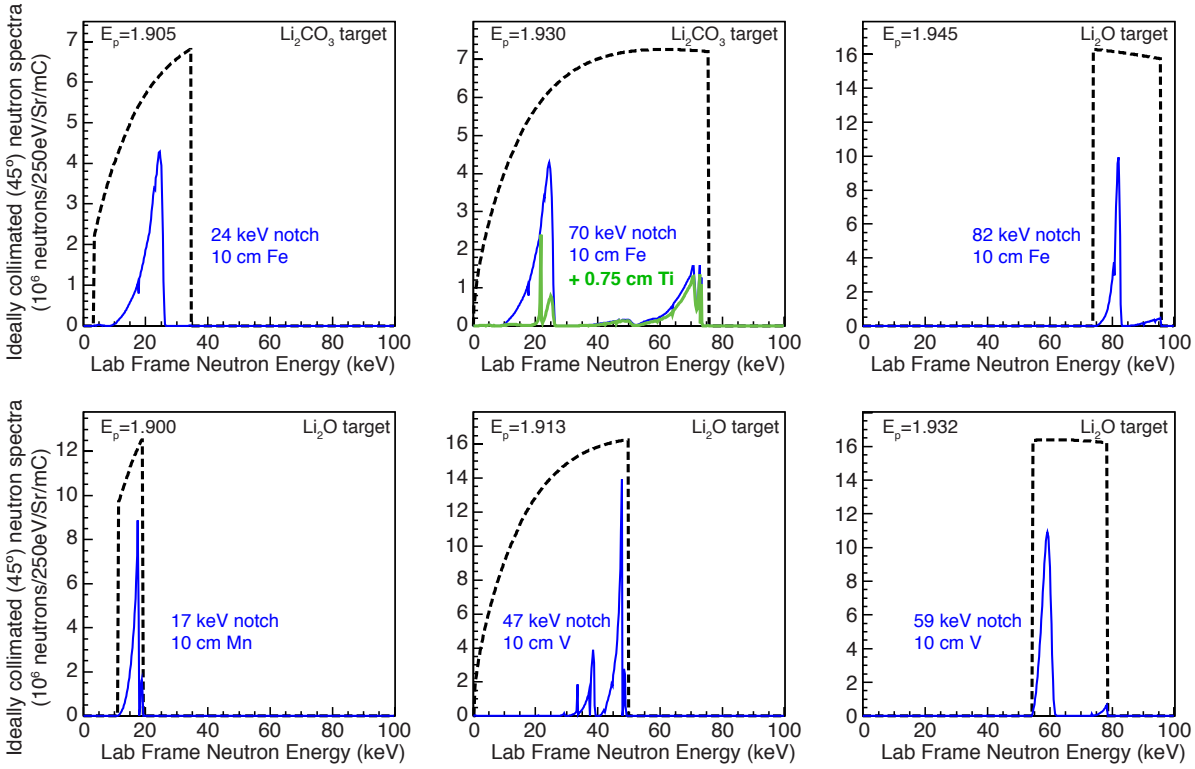

Figure 3.4: Calculated unfiltered and filtered neutron spectra targeting interference notches. Resultant neutron spectra from ideally collimated unfiltered (dashed) and filtered (solid) neutron sources collimated at 45°. The top left and center spectra use the differential yield of lithium carbonate (285 $\mu g/cm^2$). Top right and all bottom spectra use the differential yield of lithium oxide (115 $\mu g/cm^2$). Proton beam energy (E_p) used to calculate the differential yields is indicated on each figure. The length and material of each filter is listed on each figure.

3.4 Experimental Demonstration with an Iron Filter

While the performance of the 24 keV notch in iron was well characterized at a reactor facility [10], the use of an iron filter in combination with a near-threshold ^{7}Li(p,n)^{7}Be source has not been demonstrated. To validate this arrangement several measurements were performed with the prototype neutron source that was built at LLNL. The experimental setup, illustrated in Fig. 3.5, consisted of an electrically isolated flange at the target chamber of the 1.7 MV National Electrostatic Corporation 5SDH-2 tandem accelerator where the lithium target was held. The metallic lithium target, 53 $\mu g/cm^2$, evaporated on a 3 mm thick tantalum backing, was inadvertently exposed to small amounts of air during installation. Rutherford backscatter (RBS) analysis of the target indicates the composition to be lithium carbonate (Li_2CO_3) with areal density of 285 ± 57 $\mu g/cm^2$. Replacement targets were not available so this target was used.

An Ortec 439 current integrator was connected to the isolated target-holding flange for current integration during measurements, and an Ortec 872 counter/timer was used to count the output of the 439 module. Beam currents were typically 600–700 nA. A

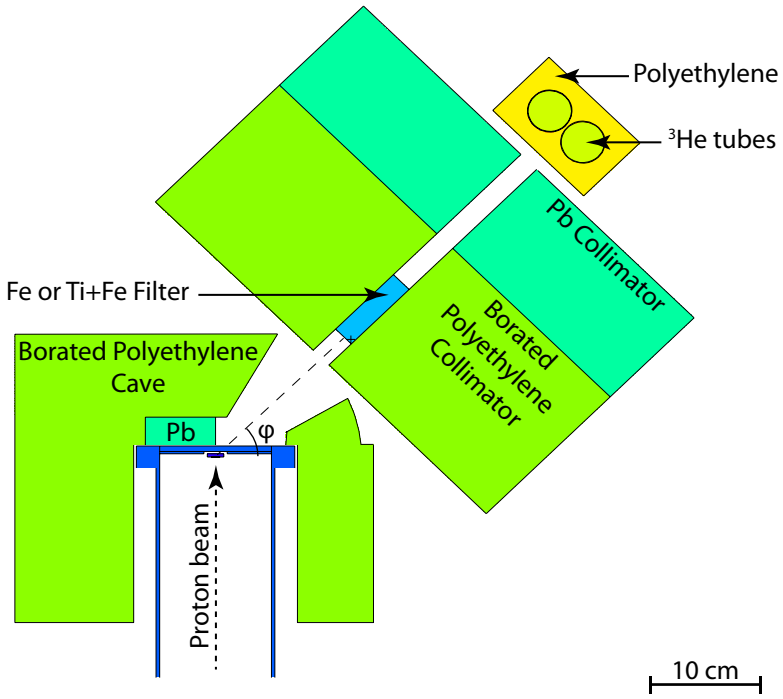

Figure 3.5: Schematic of experimental arrangement. Schematic of the beam on target, borated polyethylene and lead shielding, and counting arrangement (moderated ^{3}He tubes) for validation of the 24 and 70 keV neutron beams.

borated polyethylene cave was constructed around the lithium target. A small 2 cm high path was cut into the shielding from $30^\circ - 60^\circ$ with respect to the proton beam through which neutrons emitted in this direction could pass unimpeded (Fig. 3.5). One inch of lead shielding was placed within the borated polyethylene cave on the face of the target-holding flange to attenuate the flux of forward directed inelastic scatter gammas produced in the lithium target. The 2 cm high path was also present in the lead. An alignment post for the accelerator was placed at 0° and prevented the experimental setup from exploring shallower angles. A rotatable table, aligned to the location of the lithium target and outside of the shielding cave, held the borated polyethylene collimator (39.5x24x15.25 cm) with a 2 cm square beam path. A 2x2x7 cm iron filter was placed within the aperture in the borated polyethylene collimator. The collimator was backed by 10.15 cm of lead to attenuate the capture gammas produced in the borated polyethylene shielding. The 2 cm square beam path was also present in the lead shielding. The rotatable table was able to orient the collimator anywhere from $33^\circ - 55^\circ$ in increments of $\pm 0.5^\circ$, allowing detectors to be shifted to larger angles where neutron energies are not large enough to pass through the filter due to the reaction kinematics. All measurements described in this work were obtained with the table oriented at 45°.

The microprobe located at CAMS [64] was used to produce the proton beam. The energy spread in the proton beam was estimated to be ± 1 keV. The energy of the proton beam was initially calibrated by measuring the threshold for the ^{7}Li(p,n)^{7}Be reaction using two ^{3}He tubes placed within a 17x17x7 cm moderator directly behind the Li-target holding flange at 0°, with all shielding and collimator components removed. The ^{3}He tubes, Saint-Gobain model 15He3-608-38SHV, were held at 1300V and signals read out using Ortec 142PC preamps feeding into Ortec 485 amplifiers and LeCroy 821 discriminators set to accept events within the ^{3}He capture peak and shoulders. Counts registered by the discriminator were tallied using an Ortec 776 timer/counter.

With the shielding and collimator assembled, the performance of the filtered neutron source was validated using the 24 keV transmission notch in iron. The moderated ^{3}He tubes were placed behind the collimator (Fig. 3.5), aligned to 45°. Proton beam energy was incrementally increased to observe the kinematic turn-on for 24 keV neutrons. Figure 3.6 shows normalized counts (counts/μC) as proton beam energy is increased. The kinematic turn-on of the 24 keV notch is clearly visible. The width of the observed increase in neutron counting rate resultant from 24 keV neutron transmission matches expectations based on the 2° width of the collimator and the width of the 24 keV notch. The gradual increase of neutron count-rate before and after the kinematic turn on is attributed to moderated neutrons leaking out of the borated polyethylene collimator and shielding. The sensitivity of the ^{3}He tubes is larger for the moderated neutrons leaking through the collimator than those transmitted through the filter.

A two component model of the form $R(E_p) = C_1 T(E_p) + C_2 Y(E_p)$ was used to describe the data in Fig. 3.6 (left). R is the neutron count rate, T is the numerically cal-

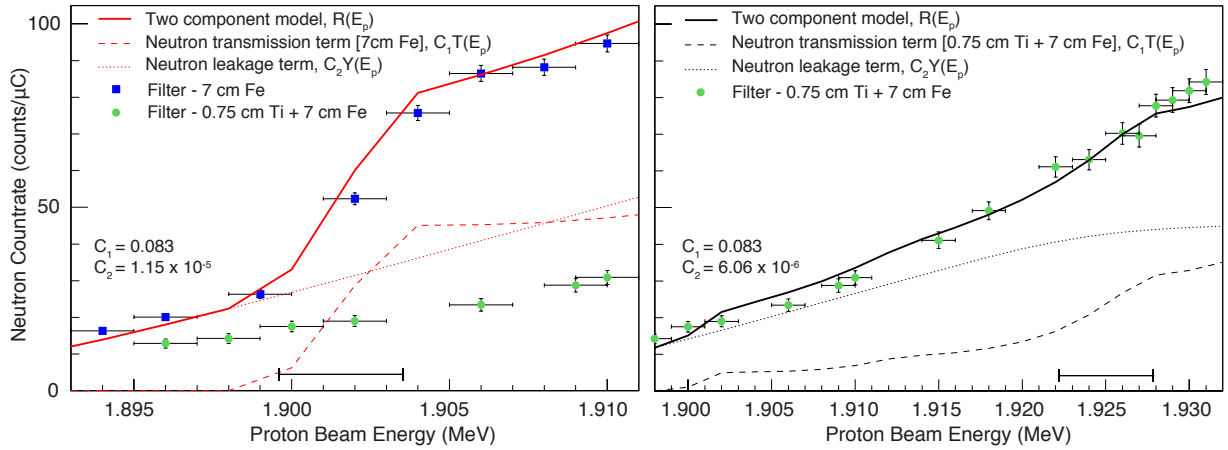

Figure 3.6: Experimental demonstration of the kinematic turn on of 24 keV (left) and 70 keV (right) neutrons. The normalized neutron count rate, using a 7 cm Fe filter (squares) and an additional 0.75 cm Ti pre-filter (circles), was measured at different proton beam energies with ^{3}He tubes placed behind the collimator at 45° (Fig. 3.5). A model with two free parameters (solid), discussed in the text, matches the data well. The horizontal bar near the x-axis indicates the region of the 24 and 70 keV kinematic turn on. A term proportional to the rate of neutrons transmitted through the filter (dashed) (C_1T) illustrates the kinematic turn on of 24 and 70 keV neutrons. A term proportional to the total neutron yield (dotted) (C_2Y) accounts for moderated neutrons leaking out of the collimator and shielding. The values of the free parameters, C_1 and C_2 are listed on the figure. Inclusion of a 0.75 cm Ti pre-filter effectively out-scatters 24 keV neutrons removing the kinematic turn on (left). This Ti pre-filter shifts the scattering profile within the collimator, decreasing the magnitude of neutron leakage. The pre-filter was used to isolate contribution of the 70 keV turn on (right).

culated rate of neutrons directed through the collimator and transmitted by the filter at beam energy E_p, and Y is the numerically calculated total neutron yield of the source at beam energy E_p. C_1 and C_2 are free efficiency parameters. The term C_1T represents the count rate resultant from neutrons transmitted through the collimator and filter. The term C_2Y describes detected thermal leakage as proportional to the total neutron yield. The agreement between the experimental data and the two component model indicates the neutron source, collimator, and filter perform as expected, and that moderated neutrons are leaking out of the collimator and shielding. The rate of moderated neutrons leaking through the shielding is low (^{3}He tubes are very sensitive to moderated neutrons). While the escape of some moderated neutrons are unlikely to cause significant backgrounds in experiments that utilize this filtered neutron source, future

improvements to the apparatus will include an increase in shielding to reduce this neutron leakage.

As an additional validation exercise, 0.75 cm of Ti was added to the 7 cm Fe filter and the measurement repeated. As previously described titanium is very effective at scattering 24 keV neutrons (Fig. 3.4) and its inclusion as a pre-filter should remove the feature attributed to the kinematic turn-on of the 24 keV notch. The result of this measurement is also shown in Fig. 3.6 (left), further confirming that the neutron source and iron filter combination is performing as expected. The titanium filter was placed upstream of the iron filter, shifting the scattering location of neutrons within the collimator upstream and resulting in a reduction of the observed neutron leakage. Additionally, with the titanium filter installed, the same approach was used to observe the kinematic turn-on of the 70 keV notch Fig. 3.6 (right). Again the experimental data is well described by the two component model. The shallow nature of the 70 keV notch, shown in Fig. 3.3, results in the kinematic turn-on being less clear than that of the 24 keV notch. Above $E_p = 1.932$ MeV, neutrons begin to transit the 82 keV notch. In Fig. 3.6, the thermal leakage term, which is proportional to the total neutron yield, plateaus as a result of the thin target.

3.5 Applications and Discussion

The rotatable design of the collimator, though unused in these measurements presented here, may be used to facilitate acquisition of representative background measurements with experiments utilizing this filtered neutron source. The beam energy (E_p) may be tuned such that neutrons effectively transit the filter when the collimator is placed at a shallow angle. A small increase in the collimation angle can then be used to shift the apparatus to a position where the neutron energies that transit the filter are kinematically forbidden. Data acquired at this larger angle will contain the backgrounds present at the shallow angle; associated capture gamma backgrounds from the neutron production, the small flux of lower energy neutrons that may penetrate the collimator and filter, and the 478 keV gammas produced by inelastic proton scatter within the lithium-loaded target. By fixing E_p and normalizing by integrated proton current on target a background subtraction can be used to isolate signals attributable to neutrons that transit the filter.

Such measurements may be performed to characterize the response of various materials to quasi-monoenergetic neutrons. More specifically, the response of materials to low-energy nuclear recoils, which may be produced via elastic neutron scattering, is of interest to the dark matter and CENNS communities. Table 3.1 lists the maximum nuclear recoil energy $E_r(\theta = \pi) = 4E_n * (Mm)/(M+m)^2$ from elastic scatter of neutrons with energies of notches illustrated in Fig. 3.4 on different detector materials. E_n is the energy of the incident neutron, M is the mass of the target nucleus, and m is the mass of the neutron.

Table 3.1: Maximum nuclear recoil energies from filtered neutron beams on Xe, Ar, Ge, and Si.

Neutron energy (keV)	*Max recoil energy* (keV)			
	Xe	*Ar*	*Ge*	*Si*
17	0.5	1.6	0.9	2.3
24	0.7	2.3	1.3	3.2
47	1.4	4.5	2.5	6.3
59	1.8	5.7	3.2	7.9
70	2.1	6.7	3.8	9.4
82	2.5	7.9	4.4	11.0

The accessible nuclear recoil energies are lower than the lowest reported characterization measurement in liquid xenon [53]. Using such a source to perform ionization and scintillation yield measurements for $\mathcal{O}$(keV) nuclear recoils would provide the necessary information to clarify the sensitivity of dark matter searches using these target materials, allow calculation of the sensitivity of these materials to CENNS of reactor neutrinos, and study the field dependence of recombination following energy deposition. One such measurement has been demonstrated using this neutron source (70 keV) to measure the ionization yield of 6.7 keV nuclear recoils in liquid argon [45].

3.6 Conclusions

The near-threshold kinematics of the ^{7}Li(p,n)^{7}Be reaction combined with the neutron transmission properties of materials such as iron, vanadium, and manganese provide the ability to produce neutron beams with narrow energy spreads using a small proton accelerator. We have designed such a source, and demonstrated production of 24 and 70 keV neutron beams using an iron filter. This neutron source may be useful for measuring the response of relevant detector materials to $\mathcal{O}$(10 keV) neutrons. One specific application being the study of detector response to low energy nuclear recoils. Measurements of this type can provide information about the energy loss mechanisms of low-energy nuclear recoils, the recombination effects when electric fields are present within the targets, and the sensitivity of different detector media. Additionally, such characterization would enable accurate calculation of the sensitivity of different detector media to CENNS of reactor anti-neutrinos.

Chapter 4

First Measurement of the Ionization Yield of Nuclear Recoils in Liquid Argon

This chapter details a measurement of the ionization yield (Q_y) of 6.7 keV ^{40}Ar atoms stopping in a liquid argon detector. Nuclear recoils were produced using the 70 keV neutron beam described in Chapter 3. This result is the first measurement of nuclear recoil ionization yield in liquid argon, the lowest energy nuclear recoils measured in liquid argon to date, and demonstration that endpoint measurements may be used to explore low-energy nuclear recoils in liquid nobles. Measurements of ionization yield were made at four different drift field values (240, 640, 1600, 2130 V/cm) to study suppression of ion-electron recombination. The Q_y of 3.6–6.3 detected e^-/keV, for applied electric fields in the range 240–2130 V/cm, is encouraging for the use of this detector medium to search for the signals from hypothetical dark matter particle interactions and from coherent elastic neutrino nucleus scattering.

Relevant Publications:

T.H. Joshi, S. Sangiorgio, A. Bernstein, M. Foxe, C. Hagmann, I. Jovanovic, K. Kazkaz, V. Mozin, E.B. Norman, S.V. Pereverzev, P. Sorensen. First measurement of the nuclear recoil ionization yield in liquid argon. *Physical Review Letters* **112**, 171303 (2014). [45]

The text and figures of this Letter (copyright American Physical Society 2014), of which I was the primary author, are included with the permission of all authors. Some of the figures have been altered to better fit the page format. Appendices have been added for additional discussion of detector installation at CAMS (Appendix A), the single electron calibration (Appendix B), and endpoint analysis (Appendix C).

4.1 Introduction

Liquid-phase argon has long been used as a target medium for particle detection via scintillation and charge collection. Recently there has been considerable interest in direct detection of both hypothetical dark matter particles [38] and coherent elastic neutrino-nucleus scattering (CENNS) [37, 35]. These as-yet unobserved neutral particle interactions are expected to result in a recoiling argon atom $\mathcal{O}$(keV), generally referred to in the literature as a nuclear recoil. This prompts the question of the available signal produced by such recoils in a liquid argon detector. This quantity must be directly measured due to the difference in signals from nuclear recoils as opposed to electron recoils (e.g. Compton electrons and β-particles). In this Letter we report the first measurement of the ionization yield (Q_y) (detected electrons per unit energy) resulting from nuclear recoils in liquid argon, measured at 6.7 keV. This is also the lowest-energy measurement of nuclear recoils in liquid argon.

These results are of interest not only for particle detection, but for theoretical studies of condensed media as well. Models of the production of ions and excited atoms from low-energy recoils in liquid argon exist, but are not fully understood in the few-keV energy range [23]. To study the influence of the electric field on recombination, and thus Q_y, data were obtained at applied electric field values of 240, 640, 1600, 2130 V/cm.

The scintillation efficiency of nuclear recoils in liquid argon has been measured from 10–250 keV at zero electric drift field using the kinematically constrained scatter of 2.8 MeV neutrons [39] and from 11–50 keV at electric drift fields from 0–1000 V/cm using the kinematically constrained scatter of 0.60 and 1.17 MeV neutrons [5]. No measurements of nuclear recoils in liquid argon exist below 10 keV.

Liquid argon dual-phase detectors have been shown to be sensitive to single electrons generated in the bulk [65]. This enhances the detection capability of the ionization channel over the scintillation channel at very low energies. A low-energy threshold and calibration are critical in both dark matter searches and CENNS discovery. Both interactions exhibit a recoil energy spectrum that rises rapidly with decreasing energy [23, 40, 4]. Our results suggest that dark matter searches using only the ionization channel in liquid argon (as has been done in liquid xenon [7]) could probe an interesting new parameter space. The observation and modeling of electric drift-field dependence presented in this Letter, and also recently reported in the scintillation channel [5], lay the foundation for a comprehensive understanding of ion recombination in liquid argon and suggests the need for optimization of drift fields in future liquid argon-based experiments.

4.2 Experimental Details

Our measurement employed a beam of neutrons to create nuclear recoils in liquid argon. The neutron spectrum was peaked at 24 and 70 keV. Contributions from the quasimonoenergetic 70 keV (12% FWHM) neutrons were selected during background subtraction. The design and deployment of the neutron beam is described in detail in Ref. [44]. Our detector, a small dual-phase argon proportional scintillation counter, is described in Ref. [65]. Small modifications to the detector since that work include the removal of the ^{55}Fe source and holder, and the replacement of one of the electrode grids. The response to ^{37}Ar calibrations has been verified to be consistent with the previous results. The active region of liquid argon has a 2.5-cm radius and a 3.7-cm height.

Particle interactions in the liquid argon can produce primary scintillation and ionization. The detector was optimized for detection of the proportional scintillation resulting from extracting the electrons into the gas-phase argon, and accelerating them across a 1.8-cm gap. The detector has been shown to be sensitive to the signal resulting from a single electron [65]. The applied electric field used to create the proportional scintillation was a constant 9.8 kV/cm for these measurements. The applied electric field ($\mathcal{E}$) across the liquid argon target, oriented in the z direction, was varied from 240 V/cm to 2130 V/cm, in order to explore the effect on the available signal. Electrostatic simulations show a 6% nonuniformity in the applied electric field within the LAr target volume, arising from the field cage spacing.

The data acquisition was triggered by fourfold coincidence of the four phototubes, in a $10-\mu$s window. The trigger efficiency was consistent with unity for signals larger than 8 ionization electrons. New triggers were vetoed for 3 ms following very large [$>\approx$10,000 photoelectrons (PEs)] events, to exclude phototube saturation effects from the data.

Research-grade argon was condensed into the detector through a getter to remove electronegative impurities, and a free electron lifetime of > 300 μs was verified throughout the experiment as in Ref. [65]. The maximum electron drift time across the target region varied from 32 μs at 240 V/cm to 14 μs at 2130 V/cm applied electric field, leading to a mean electron loss of 5%. During operation, the argon vapor pressure was maintained at 1.08 bar with 1% stability, and the liquid temperature at approximately 88 K (corresponding to a liquid density of 1.39 g/cm^3).

Q_y was measured in an end-point-type experiment. Monoenergetic neutrons with well-defined energy (E_n) interact within the liquid argon target producing nuclear recoils. For S-wave scatter, expected for this experiment, nuclear recoils are populated uniformly in energy from zero to $E_{max} = 4E_n m_{Ar} m_n/(m_{Ar}+m_n)^2 = 6.7$ keV for $E_n = 70$ keV scattering on ^{40}Ar, the most abundant argon isotope. The end point in the observed ionization spectrum is then attributed to E_{max}.

Quasimonoenergetic neutrons were produced with a collimated near-threshold ^{7}Li(p,n)^{7}Be

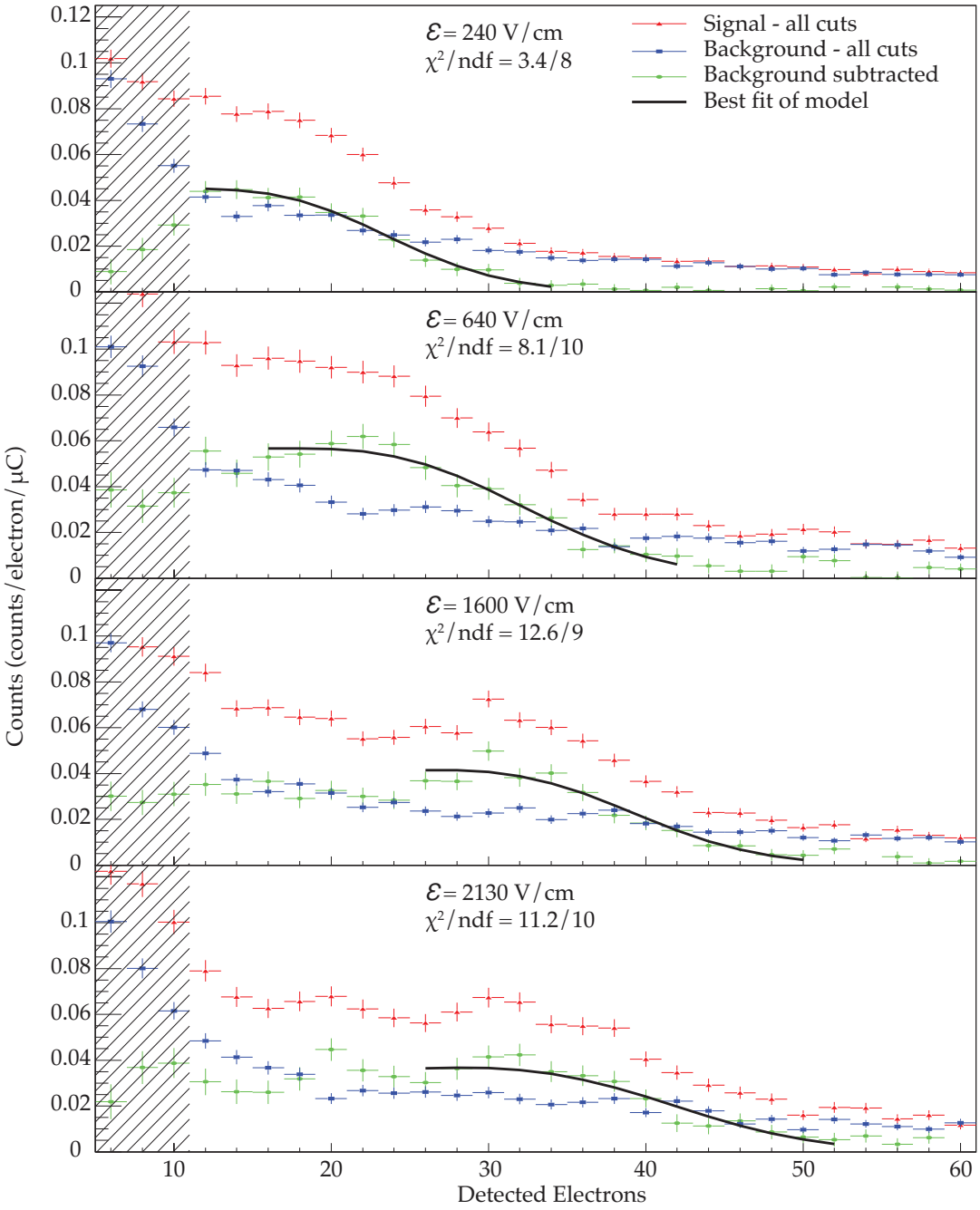

Figure 4.1: Ionization spectrum from neutron scattering at $\mathcal{E}$=240, 640, 1600 and 2130 V/cm. Data quality cuts are described in the text. Background subtracted data is shown with the best fit model in the fit region. The best fit 6.7 keV endpoint location is indicated with an arrow. Events smaller than 11 electrons (shaded region) were not considered in the analysis due to variation in the (x, y) fiducial cut efficiency.

source, and filtered with a 7-cm length of high-purity iron as described in [44]. The iron neutron filter has transmission notches at 24, 70, and 82 keV. The 70-keV notch was selected to target the low-energy side of the elastic neutron scattering resonance centered at 77 keV in ^{40}Ar thus producing a large interaction rate while limiting the probability of multiple scatter.

The proton beam energy was 1.932 MeV for all measurements and calibrated before and during data taking. Beam current was nominally 700 nA throughout data taking. The collimation aperture subtends $\pm 1^\circ$. The iron-filled collimator was oriented at $45 \pm 0.5^\circ$ with respect to the proton beam when collecting signal data. Representative background data were acquired at an angle of $55 \pm 0.5^\circ$, in which case 70 keV neutron production is kinematically forbidden, but all other beam-related backgrounds, including the 24 keV component of the neutron beam and beam-related gammas, are present.

Following the collection of neutron scatter data, a small amount of argon gas ($<$0.5g) containing 3$\pm$0.5 kBq of ^{37}Ar was injected into the detector and allowed to diffuse for one hour. Calibration data as described in Ref. [65] wer then acquired in the same four electric drift-field configurations.

4.3 Analysis

Triggered proportional scintillation (ionization channel) events identified by the analysis were subjected to a series of quality cuts. The cuts included the selection of (a) isolated events, defined as having $<$2 PEs in the 50-μs pre-trigger and $<$10 PEs following the event, and (b) the rejection of primary scintillation from peripheral background events, which have a characteristic fast rise and 1.6 μs decay time. Additional cuts include the rejection of (c) events near the (x, y) edge of the active region using the same algorithm described in Ref. [65] and (d) pileup events, e.g., axially (z) separated multiple scatters, by accepting events with 95% of signal arriving in < 20 μs. Cut (c) also strongly limits the acceptance of pile up and multiple scatters separated in (x, y). The energy dependence of this suite of selection criteria was found to vary by $<$5% for events with > 11 detected electrons. The nuclear recoil endpoint "shoulder" is clearly visible before background subtraction (Fig. 4.1).

Fluctuations in the phototube response were less than 2% over individual data sets. Single PE calibrations were performed for each data set using isolated single PE from the tail of proportional scintillation events.

The transformation of neutron scattering data from measured PE to detected electrons required a single-electron calibration from previous data because single electrons were not observed in sufficiently high rates during this experiment. Previous measurements with this detector found 7.8 ± 0.1 PEs per detected electron (PE/e^-) with a systematic uncertainty of 10% due to the difficulty in localizing the (x, y) coordinates of

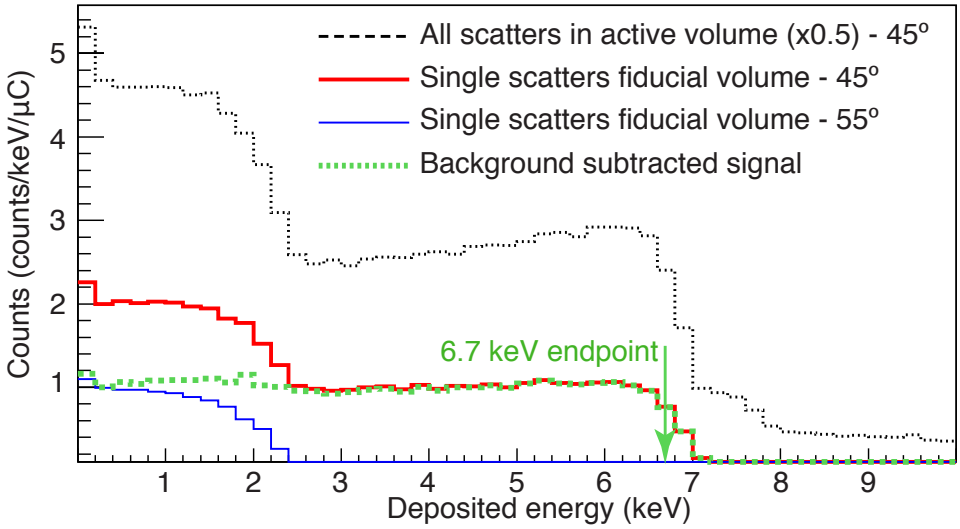

Figure 4.2: Simulated spectra from MCNP-Polimi. Expected neutron energy deposition spectra in the active detector region (black dashed) and single scatter energy deposition in the fiducial detector region when the collimator is oriented at 45° (red solid thick). In this configuration both 70 and 24 keV neutron beams are impinging on the detector. Single scatter energy deposition in the fiducial region at 55° (blue solid thin) shows only contributions from 24 keV neutrons. Background subtracted fiducial data (green dotted) illustrates the experimental design to isolate the contribution of 70 keV neutrons and the 6.7 keV endpoint.

the single-electron signals. A value of 10.4 ± 0.2 PE/e^- was used in the present analysis. The 33% increase in light yield resulted from a larger electric field and physical gap in the proportional scintillation region, and was obtained using the 2.82-keV peak from ^{37}Ar K-capture (2.82 keV released in x rays/Auger electrons [12]) acquired across a range of electric field configurations. The statistical and systematic uncertainties of this calibration were 2% and 10%, respectively.

Backgrounds during these measurements were dominantly beam related–namely, 24 keV neutrons that transit the iron filter, gammas from ^{7}Li(p,p')^{7}Li within the lithium target, and neutron-capture gammas–and were proportional to the proton current on the target. Data were normalized by the integrated proton current and corrected for the live time fraction of the data acquisition system. The normalized spectra were then subtracted as shown in Fig. 4.1.

A detailed MCNP-PoliMi [62] simulation, using the ENDF/B-VII.1 library, was performed to model the expected single-scatter spectra in both the signal and background detector configurations, as shown in Fig. 4.2. For comparison with data as shown in Fig. 4.1, the simulated

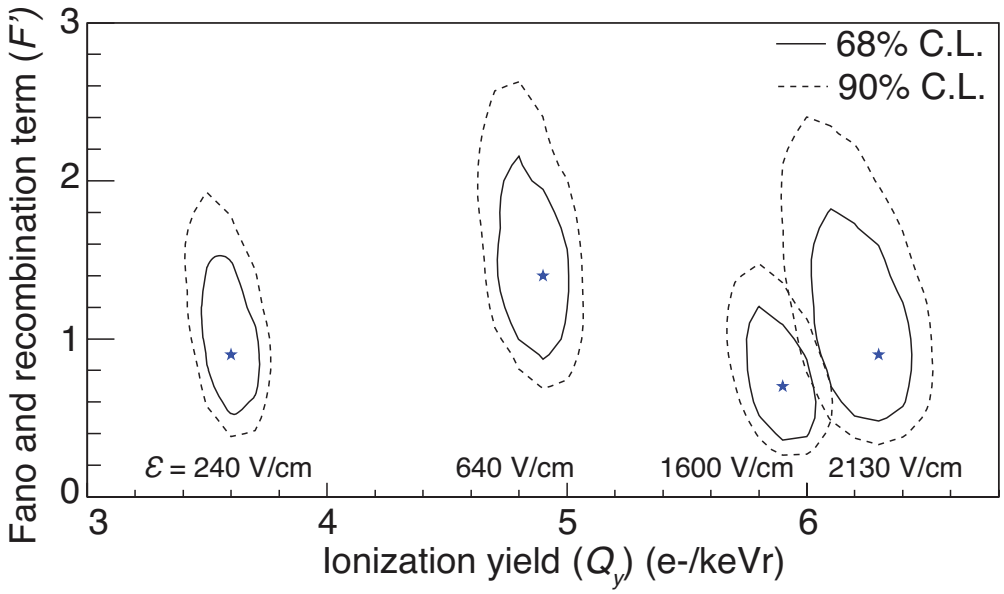

Figure 4.3: 68% and 90% confidence level contours from the endpoint analysis are shown in the space of ionization yield and F′. Stars indicate the position with minimal χ^2. The expected anti-correlation between F′ and ionization yield is observed but constrained by the analysis.

spectra were first converted from recoil energy to a number of electrons via a constant ionization yield (Q_y). Then a resolution term was applied, defined as $\sigma(n_e) = \sqrt{n_e(F' + \sigma_e^2)}$, where n_e is the number of detected electrons and $\sigma_e = 0.37$ is the measured single-electron resolution. The term $F' \equiv F + R$ accounts for the Fano factor (F) and recombination fluctuations (R). The third free parameter in the fit was the rate normalization.

A χ^2 comparison between the simulation and the background-subtracted spectrum was made using a parametric scan across the free parameters (Q_y, F', and rate normalization), resulting in the confidence level contours shown in Fig. 4.3. The region of interest for each drift field was selected to focus on the location of the end-point shoulder. The statistical uncertainty of the best-fit Q_y value was defined by the extent of the 68% confidence level contours.

We emphasize that this analysis was focused solely on extracting the ionization yield at the end point and makes no attempt to extract information about ionization yields below 6.7 keV. This is because at energies below the end point, it is not possible to uniquely resolve the degeneracy between the free parameters in the model. The most robust method of accessing information about Q_y at smaller recoil energies is to decrease the end-point energy [44]. To estimate the systematic uncertainty associated with the assumption that Q_y is constant with recoil energy, we repeated the analysis for each data set with the linear slope of the ionization yield as an additional free parameter. For all but the smallest value of $\mathcal{E}$, the best fit was obtained for a slope of about -0.8 Q_y/keV and a slightly lower end-point Q_y. This is quoted as a systematic uncertainty

Table 4.1: Uncertainties in ionization yield (Q_y) endpoint analysis.

Component		*Statistical (%)*	*Systematic (%)*
Single electron peak		2–10	10
Single electron calibration		2	10
χ^2 analysis		3–5	-
Input spectrum		-	5
Background subtraction		-	1–3
Slope of Q_y in model	240 V/cm	-	$^{+5}_{-25}$
"	640 V/cm	-	$^{+2}_{-18}$
"	1600 V/cm	-	$^{+0}_{-19}$
"	2130 V/cm	-	$^{+0}_{-21}$
Liquid argon purity		-	5
Drift field ($\mathcal{E}$)		-	6

for each drift field in Table 4.1. Additionally, we repeated the analysis using a simple step function for the input nuclear recoil spectrum, to approximate the ideal *S*-wave recoil spectrum from monoenergetic 70 keV neutrons (this is not shown in Fig. 4.2). This provided a conservative approximation of the uncertainty due to underlying uncertainties in the differential nuclear cross-section data, used in the MCNP-Polimi simulation. The systematic uncertainty associated with subtraction of background data was assessed using an exponential fit to background data (> 11 electrons). Using the best-fit exponential for subtraction yielded the same best-fit Q_y. Varying the exponential constant $\pm 15\%$ resulted in a ± 1–3% shift in best-fit Q_y.

Table 4.1 summarizes the statistical and systematic uncertainties present in the ionization yield results. The statistical uncertainty of the best-fit mean is quoted. Asymmetric uncertainties were attributed to several of the listed parameters as a result of their underlying nature. Uncertainties were added in quadrature when combined.

4.4 Results & Discussion

The number of electrons detected from 6.7-keV nuclear recoils as a function of applied electric drift field is shown in Fig. 4.4 and the ionization yield with uncertainties is listed in Table 4.2. The strong dependence on the electric drift field is in reasonable agreement with recent observations in the scintillation channel [5], consistent with the expected anticorrelation of scintillation and ionization. The different recoil energies and the lack of absolute scintillation yields in Ref. [5] prevent a quantifiable comparison.

This field dependence is understood to be a suppression of ion-electron recombination along the ionization track and is extensively discussed in Ref. [23]. In order to fit our data we consider

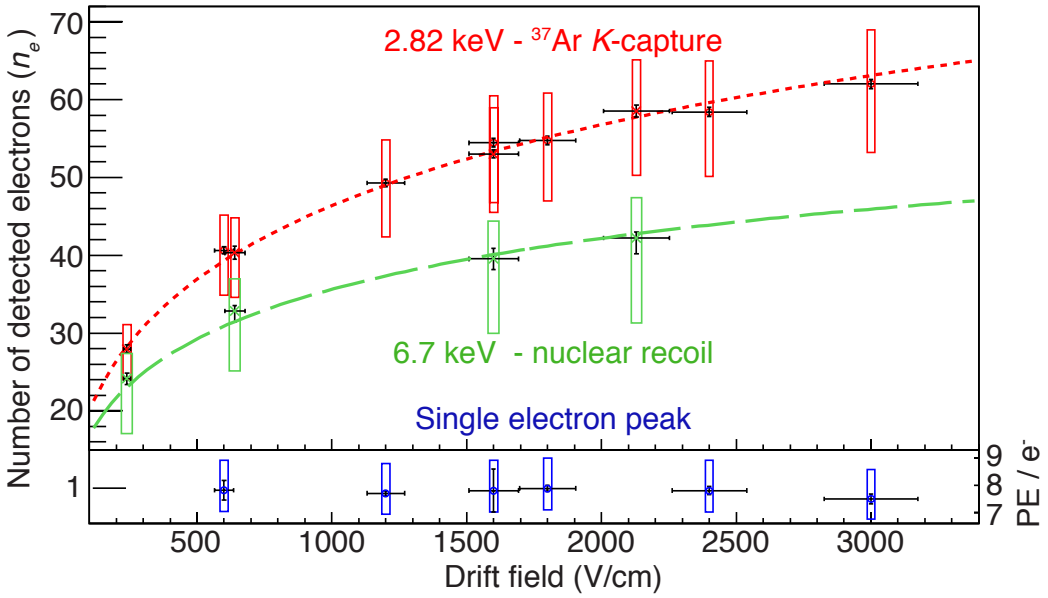

Figure 4.4: (upper) The number of observed electrons from 2.82 keV ^{37}Ar K-capture events and 6.7 keV nuclear recoils as a function of $\mathcal{E}$, with systematic (boxes) and statistical (bars) uncertainty on the mean. Curves are the best fit obtained from Eq. 4.1. (lower) The single electron peaks used (in conjunction with 2.82 keV data) to infer the single electron calibration for endpoint analysis.

an empirical modification [30, 70] of the Thomas-Imel box model [73],

$$n_e = \frac{N_i}{\xi}\ln(1+\xi), \quad \xi = \frac{N_i C}{\mathcal{E}^b}. \tag{4.1}$$

N_i is the number of initial ion-electron pairs produced, n_e is the number of electrons that escape recombination, $\mathcal{E}$ is the applied electric field, and b and C are constants. The electric drift-field dependence is modified from the original model to have a power-law dependence, $\xi \propto \mathcal{E}^{-b}$. The number of initial ion-electron pairs may be written as

$$N_i = \frac{fE}{\epsilon\,(1+N_{ex}/N_i)}, \tag{4.2}$$

where E is the amount of energy deposited in the track, f is the fraction of energy lost through ionization and atomic excitation (unity for electronic recoils) often termed a quench factor, $\epsilon = 19.5$ eV is the average energy required to produce a quantum (excitation or ionization) in liquid argon [33], and N_{ex} is the number of initial excitations. The ratio $N_{ex}/N_i = 0.21$ was measured for electronic recoils in liquid argon [48]. The model has only two free parameters (C, b) when describing electron recoils. Using the 2.82-keV ^{37}Ar *K*-capture calibration data a best fit (Fig. 4.4) yields $C = 2.37$ and $b = 0.61$ when $\mathcal{E}$ is expressed in V/cm.

Table 4.2: Measured ionization yields with uncertainties.

$\mathcal{E}$ (V/cm)	Q_y (e^-/keV)	Statistical	Systematic
240	3.6	$^{+0.1}_{-0.1}$	$^{+0.5}_{-1.1}$
640	4.9	$^{+0.1}_{-0.2}$	$^{+0.6}_{-1.2}$
1600	5.9	$^{+0.2}_{-0.2}$	$^{+0.7}_{-1.4}$
2130	6.3	$^{+0.1}_{-0.3}$	$^{+0.8}_{-1.6}$

Using these values for b and C, the number of initial ion-electron pairs (N_i) is left as a single free parameter when applied to nuclear recoil data. Fitting to the data (Fig. 4.4) we observe good agreement and find $N_i = 72 \pm 2$, assuming this model remains valid at high (saturating) field values. The fact that recombination in liquid argon can be described by the same phenomenological model for few-keV electron and nuclear recoils suggests a similarity in the spatial distribution of electrons and ions for these different energy-deposition mechanisms.

Using Eq. (4.2) and the calculations of Lindhard *et al.* [51] for the partitioning of nuclear recoil energy ($f = 0.25$) results in $N_{ex}/N_i = 0.19$, which is surprisingly similar to the value for electron recoils. Alternatively, if $N_{ex}/N_i \sim 1$ (as measured for nuclear recoils in liquid xenon [67]) then one would find $f = 0.42$. If confirmed this would suggest a promising sensitivity of liquid argon at low energies. Simultaneous measurements of scintillation and ionization are needed to unambiguously determine f and N_{ex}/N_i.

We are not aware of any measurements or theoretical expectations for either the Fano factor or recombination fluctuations for nuclear recoils in liquid argon. With the simple assumption that recombination statistics are binomial, the probability for an electron to escape recombination is $p = n_e/N_i$, and so $R = 1 - n_e/N_i$. From this, it would follow that the Fano factor is given by $F = F' + n_e/N_i - 1$. Taking the range of p from Fig. 4.4 it is clear that F is smaller than F' by a factor which ranges from 0.65 at $\mathcal{E} = 240$ V/cm to 0.42 at $\mathcal{E} = 2130$ V/cm. This is consistent with $F \approx 0.5$, with a fairly large uncertainty as shown in Fig. 4.3.

In this Letter we have presented the first nuclear recoil ionization yield measurement and the first measurement of sub-10-keV nuclear recoils in liquid argon using an end-point-type measurement. This demonstration suggests that end-point measurements with filtered neutron sources [44, 11, 60] are suitable for a comprehensive study of both scintillation and ionization yields of low-energy nuclear recoils in liquid argon, and could also probe < 4 keV in liquid xenon. The results of such a study would clarify the threshold and calibration of liquid noble-based dark matter detectors and CENNS searches. The measurements presented in this Letter demonstrate a large ionization yield for nuclear recoils at energies below current thresholds of liquid argon dark matter searches, suggesting the ionization channel as a means for exploring light-mass dark matter in existing and future liquid argon detectors.

Chapter 5

Nuclear Resonance Fluorescence: A Source of Low-Energy Nuclear Recoils

After studying NRF during my first year in graduate school and assisting on measurement of the NRF states in ^{237}Np, I realized that it could be used as a means of producing tagged sub-keV nuclear recoils. This is the energy range relevant to CENNS searches at nuclear reactors. In this chapter I describe how certain NRF states, sufficiently wide and isolated, can be used to produce tagged low-energy nuclear recoils if a narrow high intensity gamma source is available, using liquid argon as a candidate material. As principal investigator I proposed using this technique to make ionization yield measurements at the High Intensity γ-ray Source (HIγS) at the Triangle University Nuclear Laboratory. While the proposal was successful and our collaboration was awarded 60 hours of beam-time, the performance of the G/NARRLI detector never reached the necessary level to make measurements viable.

Relevant Publications:

T.H. Joshi. A novel source of tagged low-energy nuclear recoils. *Nuclear Instruments and Methods in Physics Research A* **656.1** (2011). [43]

The text and figures of this article (copyright Elsevier 2011), of which I was the sole author, are included in this chapter. Some of the figures have been altered to better fit the page format.

5.1 Introduction

Direct WIMP dark matter [38] and coherent neutrino-nucleus scatter (CNS) [35, 37] searches attempt to detect WIMPs and neutrinos respectively by measuring the energy they deposit when scattering off nuclei in a detector. Understanding the way recoiling nuclei distribute energy between scintillation, ionization, and thermal motion as a function of recoil energy is required to define the sensitivity of these rare event detectors. For this purpose the scintillation efficiency (L_{eff}) and ionization yield (I.Y.) of nuclear recoils have been reported in candidate detector materials (see Table 5.1). Of the reported measurements, only two [42, 10] have probed recoils below one keV, the energy range most important to CNS searches [35, 40, 4]. Moreover, though the energy domain below a few keV is currently inaccessible in most current WIMP searches, an improved understanding of detector sensitivity in this domain could have significant benefits for setting exclusion limits on WIMPs [9, 26].

It is therefore desirable to experimentally measure the signals produced by nuclear recoils at energies below a few keV. The lowest recoil energy reported [42] made use of the nuclear recoil accompanying an (n,γ) interaction. This approach is hampered by the limited choice of γ-emitting transitions in the target material and is further complicated by additional energy deposition from secondary γ-emission. Published measurements at higher recoil energies have employed elastic and inelastic neutron scattering for nuclear recoil production. Those using the latter exploited several low-lying states in Ge isotopes and measured the broadening of their relaxation resulting from the (n,n$'$) nuclear recoil for varying incident neutron energies [21, 22, 41]. The measurements producing recoils with elastic neutron scattering may be split into two families; the first using mono-energetic neutrons incident on a target and detecting neutrons that scatter in the target at a known scattering angle, the second employ broad spectrum neutron sources and compare data with Monte Carlo simulations. For the purpose of exploring the domain below a few keV, using a mono-energetic neutron source and explicitly tagging the scattered neutron to identify recoil energy is preferable to minimize systematic uncertainty in the measurement. Extending measurements of this type to lower recoil energies may be accomplished by either decreasing the incident neutron energy [10], in which case prompt tagging of the scattered neutron becomes a

Table 5.1: Previously reported measurements of the relative scintillation efficiency (L_{eff}) and ionization yield (I.Y.) from low-energy nuclear recoils in candidate detector materials.

Target medium	Nuclear recoil energy (keV)	Recoil mechanism	Measured quantity	*Ref.*
LXe	2–115	(n,n)	L_{eff} & I.Y.	[8, 53, 68]
LAr	11–239	(n,n)	L_{eff}	[39]
Ge	1–100	(n,n$'$)	I.Y.	[21, 22, 41]
	0.3–1.4	(n,n)	I.Y.	[10]
	0.254	(n,γ)	I.Y.	[42]

challenge, or decreasing the neutron scattering angle. Both cases pose significant experimental challenges.

In this paper, an alternative approach is presented by considering elastic photo-nuclear scattering rather than elastic neutron-nucleus scattering. As in the neutron experiments the scattered photon may be detected at a known scattering angle, but with the added benefit of energy discrimination in the γ-tagging detectors, at energies above radioactive backgrounds. The experimental viability of elastic photo-nuclear scattering, both nuclear Thomson and Delbrück, is limited by small cross-sections. The resonant photo-nuclear scattering process of Nuclear Resonance Fluorsescnce (NRF) does not suffer this limitation. The large cross-section and relatively large width (short lifetime) of some NRF states enable nuclear recoils in the energy domain below a few keV to become accessible to detailed study by providing a novel source of tagged low-energy nuclear recoils.

5.2 Nuclear Recoils from NRF

NRF describes the resonant absorption of a photon by a nucleus and the subsequent relaxation of the excited nucleus via γ-emission. A detailed discussion of NRF can be found in [57]. The excited nucleus may decay through various allowed channels (Γ_i), but the branch (Γ_0) to the ground state will be the focus of this paper. Following photo-absorption, the excited nucleus recoils with momentum equal to that of the incident photon. Governed by the width (Γ) of the nuclear level, the excited nucleus exists for a finite lifetime ($\tau = \hbar/\Gamma$) before relaxing, in this case via emission of a 'fluoresced' photon, again imparting recoil momentum to the nucleus.

Approximating the energy of the incident and fluoresced photons as the resonance energy (E_r), the momentum transferred during NRF is simply $2E_r \sin(\theta/2)/c$, where θ is the angle of fluorescence, relative to the direction of the incident photon, in the laboratory frame (see Fig. 5.1). Expressing this quantity in terms of kinetic energy, the energy of the nuclear recoil (E_{NR}) resulting from NRF can be described in terms of the resonance energy (E_r), mass of the target nucleus (M), and the angle of fluorescence (θ).

$$E_{NR} = \frac{2\left(E_r \sin(\theta/2)\right)^2}{Mc^2} \tag{5.1}$$

This description of final nuclear recoil energy is valid when the lifetime of the excited nuclear state is short enough that no momentum is transferred to the surrounding medium by the recoiling nucleus before photon emission. If this assumption is not met, the momentum transferred during NRF is shared by several atoms, introducing a background, scattering before fluorescence (SBF), to the measurement. The fluoresced photon may still trigger data acquisition. The probability an NRF interaction will result in SBF, or FBS (fluorescence before scattering), is governed by the width of the NRF state, the atomic environment of the target material, the mass of the target nucleus, and the resonance energy. If the mean free path of a nuclear recoil in a given medium is ℓ, the probability that the recoiling excited nucleus will relax before scattering (P_{FBS}) and thus create a single nuclear recoil with energy related to the angle of fluorescence is given

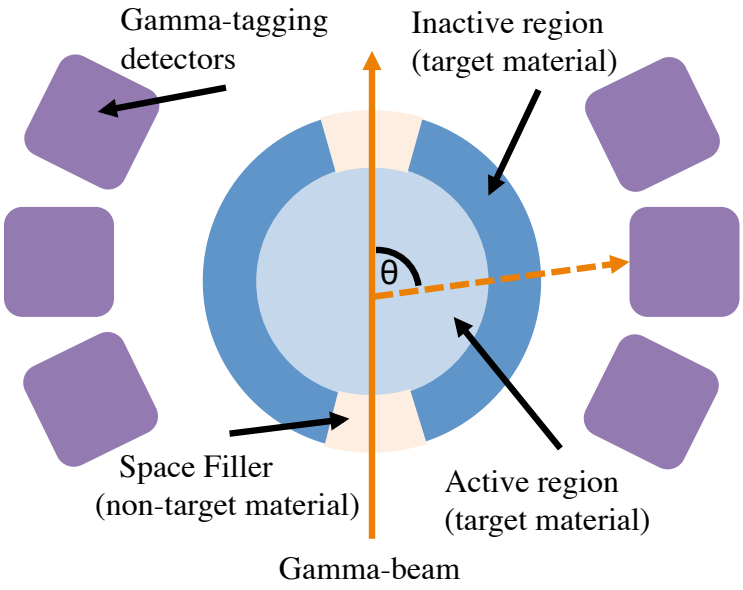

Figure 5.1: Proposed experimental setup illustrating a γ-beam incident on a detector with active and inactive regions of a target material. A space-filling material is placed in the beam path to prevent attenuation of resonant photons in the inactive detector region. The detector is surrounded by an array of γ-detectors for tagging NRF photons. Image proportions are not to scale.

by Eq. (5.2).

$$P_{\mathrm{FBS}} = \ell^{-1} \int_0^{\infty} e^{-x/\ell} \left(1 - e^{-x/L}\right) dx \tag{5.2}$$

The mean distance a recoiling excited nucleus travels before fluorescence is described by $L = E_{\mathrm{r}} \cdot \hbar c / \left(\Gamma \cdot Mc^2\right)$. In a simple fluid the mean free path may be approximated as $\ell = (\mathrm{n}\text{œ})^{-1}$ where n is the local number density and σ is the scattering cross-section. If the system is of greater complexity molecular dynamics simulations may be employed to study the probability of fluorescence before scattering.

5.3 Experimental Considerations

The general design of a measurement utilizing NRF to produce nuclear recoils will consist of a photon beam incident on a detector sensitive to the signals produced by a nuclear recoil (see Fig. 5.1). The incident γ-beam produces nuclear recoils in the target region of the detector via NRF, and energy resolving γ-detectors, placed at different angles of fluorescence, trigger data acquisition upon detection of resonance energy photons. Optimization of an experimental design must take into account selection of target resonances, characteristics of the γ-beam, geometry and response of the detector, and the γ-tagging detectors in order to maximize data collection rates.

A suitable resonance must be selected in an abundant isotope of the target material of the detector by using Eqs. (5.1,5.2) and verifying it has a large branching ratio to the ground state. Using only γ's emitted during relaxation to the ground state is important in reducing background for two reasons. If a branch to an excited state is used, the energy of the fluoresced γ is below beam energy, and can be mimicked by photons created by background processes, resulting in false triggers. Additionally, the recoiling nucleus is still unstable and will likely decay quickly via γ-emission, depositing additional recoil momentum in the target medium. The density of neighboring NRF states also impacts state selection. Assuming the γ-tagging detectors are unable to resolve the peaks from neighboring resonances, the presence of several wide states within the envelope of the γ-source spectrum will increase the event rate at the expense of recoil energy resolution.

Selection of a suitable γ-source is paramount for the proposed measurement. This application of NRF requires the γ-source to provide a well collimated beam of photons, of which a significant number are on resonance. For this reason, bremsstrahlung sources are un-usable due to their broad spectrum. A line source from the relaxation of a nuclear level would be ideal, however, identification of a usable line source may pose a challenge. One flexible option is a Compton-backscatter γ-source at a free electron laser. These facilities are capable of providing tunable pulsed quasi-monoenergetic gamma-beams with energy resolution of one percent [77].

Beam photons, resonant and nonresonant, will pass through the inactive and active regions of the detector. The mean free path of resonant photons in the target medium will be short due to the large cross-section for resonant absorption. It is therefore important to design or modify a detector in a way that prevents the beam from encountering the target isotope until reaching the active region of the detector to prevent attenuation of resonant photons, like the 'space filler' in Fig. 5.1. The size of the detector's active region may be optimized by minimizing the ratio of statistical uncertainty to event rate considering the characteristics of the γ-source and detector.

Non-resonant γ's either pass through the detector or interact via photoelectric, Compton scatter, or pair-production. When one of these interactions occur, the detector response will be significantly larger than those produced by the nuclear recoils from NRF, except in the rare case of very low-energy transfer Compton scattering. The large signals make these background events rejectable, a task further simplified in detectors capable of discriminating electronic recoils from nuclear recoils [52, 53]. Though the vast majority of source-related background interactions may be easily rejected, their pileup with NRF events, within the response time of the detector, becomes an irreducible background and reduces rate of usable events. In addition to P_{FBS}, the response times of the detector are then important in constraining the tolerable flux from the γ-source to maximize the rate of 'clean' NRF events.

Following NRF, detection of the full energy deposition of a fluoresced γ serves as the trigger for data acquisition and the tag of nuclear recoil energy. In order to improve γ-tagging efficiency, an array of γ detectors is placed around the target detector, each placed at different fluorescence angles and therefore tagging different recoil energies. The γ-detectors must be placed outside of the shallow angles where Compton scattered photons are still high in energy and could produce false triggers. The angular domain available for γ-detector placement is thus constrained by the resolution of the γ detectors and the beam energy. The angular position of the γ detectors will

Table 5.2: Properties of candidate NRF states in ^{40}Ar [58].

E_r (MeV)	Γ (eV)	Γ_0 (eV)	P_{FBS}	$E_{NR}(\theta = \pi)$ (keV)
4.769	0.8	0.8	0.931	1.22
9.356	1.0	0.57	0.896	4.70
9.416	3.4	1.2	0.967	4.76
9.500	7.9	6.0	0.983	4.85
9.582	7.3	1.6	0.984	4.93
9.849	20.8	9.7	0.994	5.21
9.950	9.7	1.75	0.987	5.32

also impact the expected count rates due to the anisotropy of NRF, which is governed by the initial and final nuclear states as well as the polarization of the incident γ-beam [77].

Selection of the type of γ detectors is important for data collection rates as the overall γ-tagging efficiency is limited by solid angle and full energy deposition efficiency. Key properties for consideration are γ detector material, volume, and response time. Only moderate energy resolution is required because no background process may create photons with energy near the beam energy, E_r, assuming the beam/resonance energy is above natural background. Nuclear Thompson, Delbrück, and Rayleigh scattering produce E_r energy photons with very small probabilities, but these processes also produce the nuclear recoil of interest and would thus add to the signal rate. The γ detector response time should also influence selection because pileup of background photons in the tagging detectors will increase the dead time in the system. The availability of large crystals with high density, moderate energy resolution, and fast scintillation times make inorganic scintillators strong candidates for this task.

In some situations, measurements may be performed without γ-tagging detectors. If beam-related background interactions can be rejected with high efficiency then two types of measurements become available. The largest non-background signals may be attributed to the largest nuclear recoil energy produced by the selected fluorescence state in an end-point measurement. Going one step further, the theoretical distribution of nuclear recoil energies produced by the target resonance could be folded into analysis of the non-background signals in a similar manner to broad-spectrum neutron scatter measurements [68]. High efficiency background rejection would require detailed background characterization with beam on- and off-resonance in addition to selective triggering of the DAQ and post-processing cuts on quantities such as energy, position, and event shape.

5.4 Liquid Argon: A Model Case

Liquid Argon (LAr) is an ideal case to consider for this novel application of NRF. It is the detector material used in, and proposed for, several dark matter and CNS searches [1, 49, 40]. The

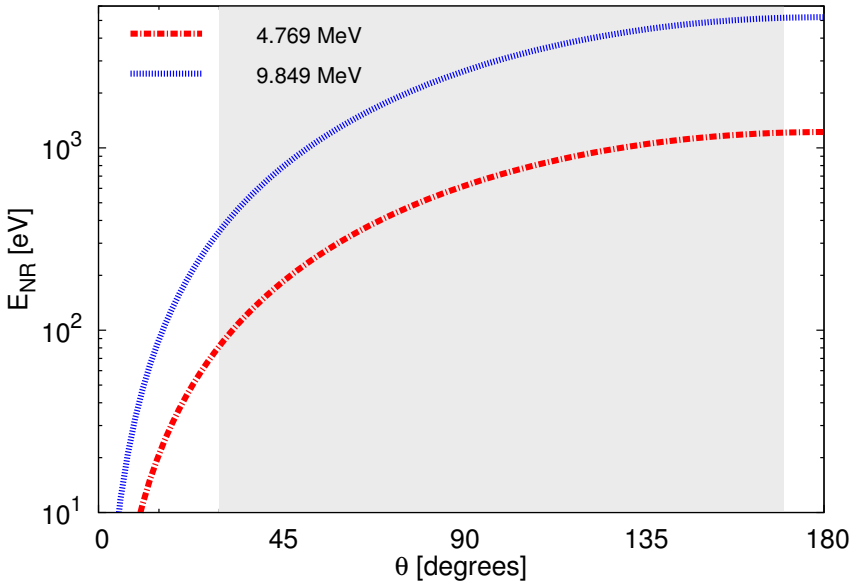

Figure 5.2: Nuclear recoil energy (E_{NR}), Eq. 5.1, as a function of fluorescence angle (θ) for two candidate resonances in ^{40}Ar. The shaded region shows the angular domain available for γ-tagging.

level structure of the most abundant isotope, ^{40}Ar (99.6 %), is well documented up to 10 MeV [58]. Examination of the ^{40}Ar level structure reveals several wide 1^- levels (E1 transitions) in ^{40}Ar, shown in Table 5.2. The 4.769 MeV state is well suited for production of sub-keV nuclear recoils and the resonances above 9 MeV offer the ability to produce nuclear recoils up to 5.3 keV. Selection between these higher energy states is based on ground state width and isolation. Using these criteria, the 9.849 MeV state is preferable. Fig. 5.2 shows nuclear recoil energy vs fluorescence angle for the 4.769 and 9.849 MeV states.

To illustrate the experimental feasibility of this technique we consider a LAr detector with a four cm diameter active region with a 1-cm thick inactive region, filled with PTFE in the beam path to prevent attenuation of the resonant photons (shown in Fig. 5.1). Table 5.3 gives calculated interaction rates if a pulsed γ-source producing 10^5 γ/sec with a one percent energy resolution, characteristic of the High Intensity Gamma-ray Source in high resolution mode (2.79 MHz spill frequency) [77], were incident on this detector. The rate of NRF events ($\dot{R}$) is numerically calculated using the Doppler broadened resonance cross-section [57]. The incident flux and spill frequency of the γ-source are used to calculate Δ, the fraction of NRF events not lost due to pileup with background interactions Eq. (5.3). The total trigger (T) and 'clean' trigger (C) rates are given by Eqs. (5.4) and (5.5) respectively.

$$\Delta = \left(\sum_{k=0}^{\infty} \frac{\lambda^k e^{-\lambda}}{k!} (\zeta)^k \right)^x \tag{5.3}$$

Table 5.3: Summary of estimated event rates and parameters for two resonance energies (E_r). The rate of NRF interactions in the target region is $\dot{R}$ and Δ describes the fraction of NRF events that are not lost due to pileup with background interactions. Trigger rates, total (T) and 'clean' (C), are given per γ-tagging detector with full-energy deposition efficiency η_γ at $\theta = \pi/2$.

E_r (MeV)	$\dot{R}$ (Hz)	Δ	η_γ	T (hour^{-1})	C (hour^{-1})
4.769	22.9	0.355	0.113%	94	33
9.849	49.7	0.415	0.076%	135	56

$$T = \eta_\gamma \cdot \dot{R} \tag{5.4}$$

$$C = T \cdot P_{\mathrm{FBS}} \cdot \Delta \tag{5.5}$$

The probability that a beam-energy photon will pass through the active region of the detector without interaction is ζ, λ is the average number of photons expected per spill from the γ-source ($\lambda = 10^5\ \gamma/\mathrm{sec} \times (2.79\ \mathrm{MHz})^{-1}$), k is the number of photons per spill, x is the number of spills in two detector response times (assumed to be $2 \times 30\ \mu$s, $\therefore\ x = 2.79\ \mathrm{MHz} \times 60\ \mu\mathrm{s} = 168$), and the full-energy deposition γ-tagging efficiency is η_γ.

Placement of γ-tagging detectors at small θ is limited by the possibility of Compton scattered photons producing false triggers. The finite size of an actual detector smears the limiting tolerable angle. Conservative placement of γ-tagging detectors at scattering angles larger than 30 degrees prevents Compton-scattered photons and Bremsstrahlung from producing false triggers. Photons elastically scattered through Nuclear Thomson, Delbrück, or Rayleigh interactions by the inactive region of the detector can also produce false triggers. The differential cross-sections of these interactions at relevant angles ($\theta > 10$ degrees) are small, $\mathcal{O}(\mu\mathrm{b/sr})$, and thus their contribution is not included in this exercise.

The estimated event rates suggest that a statistically significant ensemble of tagged energy nuclear recoil events could be collected in several hours of beam-time while operating with an array of γ-detectors. It is therefore feasible to use NRF to produce nuclear recoils from 0.1–5.2 keV in LAr to characterize scintillation and ionization yields. Similar measurements may also be possible in other materials such as Ge, LXe, and LNe if appropriate resonances can be identified.

Chapter 6

Future Work & Conclusions

The work presented within this dissertation was a part of a larger collaborative effort focused on detection of CENNS at a nuclear reactor. While the results presented here helped to further this effort, significant work remains. Additionally, several ideas I conceived during my research on this project may be built upon in the future to assist in calibration and characterization of liquid noble detectors. In this chapter I discuss nuclear recoil measurements that can be made using the techniques and apparatus presented in this dissertation (Sec. 6.1), the experimental path towards ultra-pure ^{37}Ar and ^{127}Xe sources (Sec. 6.2), and summarize the work presented in this dissertation in the context of the larger physics efforts (Sec. 6.3),.

6.1 Future Measurements

The G/NARRLI detector is capable of making an ionization yield measurement at 2.3 keV using the 24 keV neutron beam. This neutron beam can be produced with the existing infrastructure and the same iron filter used for the 70 keV neutron beam.

Such a measurement will be a significant challenge. The increased 24 keV neutron flux is offset by the smaller cross-section in argon resulting in a rate 0.33% of that with 70 keV neutrons. Additionally, the expected endpoint shoulder will likely lie on the exponential noise wall observed below 10 electrons during the 70 keV measurements. This poses a challenge for G/NARRLI in its current incarnation as a result of the varying efficiency of the fiducial cut below 11 electrons.

In addition to measurements in LAr, detailed study of the nuclear recoil response in LXe is needed to clarify the sensitivity of dual-phase xenon detectors. Such measurements are currently planed at LLNL. The flat neutron scattering cross-section of xenon isotopes in the 10–100 keV energy range means the use of the 70 keV notch in iron is no longer desirable (it was used to target the low-energy side of a resonance in argon). Rather, if using an iron filter, using the 24 and 82 keV notches will deliver the largest experimental rate. When targeting the 82 keV notch using the current apparatus it would be best to include ≥ 10 cm of iron and the 0.75 cm titanium pre-filter to out scatter 24 keV neutrons. Measurements on xenon present an addition challenge of non S-wave neutron scattering. While the kinematically defined endpoint will still be known, the constant population of recoils up to this energy will no longer be present. As a result, the clear endpoint shoulder visible in measurements on argon may no longer be present, however with similar simulation and analysis the endpoint signal should be identifiable.

6.2 Ultra-Pure Calibrations

Introducible dispersible radioactive calibration sources are attractive for calibration of large dual-phase noble element dark matter searches and for detailed low-energy studies in laboratory based systems. While ^{nat}Ar may be cheap, the price of Xe and low-background Ar is non-trivial. As a result, introducible calibrations pose significant risk for introduction of long-lived contaminants. Additionally, large amounts of stable Ar may be considered a contaminant in Xe, so calibration sources need to be highly concentrated. As a result, ultra-pure production techniques should be used to minimize and/or eliminate risk when introducing calibration sources into dark-matter searches and laboratory based Xe systems.

One isotope of primary concern is ^{39}Ar, a long lived β^- emitter ($Q = 565$ keV and $t_{1/2} =$ 269 y). This isotope is produced during production of ^{37}Ar via thermal capture on ^{nat}Ar via ^{38}Ar(n,γ) and fast neutron irradiation of Ca via ^{42}Ca(n,α). In LAr based detectors ^{39}Ar is already a limiting background (1 Bq/kg in ^{nat}Ar) and has driven research in extraction of underground, low-background Ar. This low-background argon has only an upper limit placed upon its ^{39}Ar content, but will soon be experimentally measured in DarkSide-50. In xenon detectors, if accidentally introduced, ^{39}Ar would become a significant background in the WIMP search region due to the limitations of electron recoil rejection in dual-phase xenon and the difficulty in remov-

ing argon from xenon. Additionally, in understanding the acceptable levels of ^{39}Ar, one must consider the future uses of the xenon being used (e.g. if xenon from LUX is going to be used in a future experiment with a lower background budget).

To avoid possible contamination with ^{39}Ar, ^{37}Ar may be produced via ^{37}Cl(p,n), with a threshold of 1.640 MeV. A chlorine target has no first order production mechanisms for ^{39}Ar. Proton irradiation of crystalline NaCl has been used to produce ^{37}Ar trapped in the salt lattice for later extraction [76, 47].

An additional noble isotope that undergoes electron capture is ^{127}Xe ($Q = 662.4$ keV and $t_{1/2} = 36.3d$ days). Following K and L-capture 34 and 4 keV is released in x-rays and Auger electrons, respectively, making it a useful low-energy calibration source. This isotope was observed in LUX, cosmogenically produced in the xenon, but may be useful for calibration in the laboratory or future dark matter searches. This isotope can be produced in a similar manner to ^{37}Ar , via ^{127}I(p,n) (e.g. proton irradiation of NaI) [27]. The yield of a production run should be nearly entirely ^{127}Xe because iodine has only one naturally occurring isotope.

The extraction of ^{37}Ar or ^{127}Xe from the salt targets could be performed via dissolution or heating of the targets. The gas from this volume could then be pumped through a series of cold traps and getters, to remove any volatile impurities, and then through a cooled sealable volume filled with activated charcoal where the ^{37}Ar or ^{127}Xe would be frozen out. The product may be analyzed via atomic mass spectrometry and diluted for non-pressurized storage and transportation.

6.3 Conclusion

CENNS is predicted by the standard model but continues to elude detection. A first measurement of this flavor-blind neutrino interaction will be a true achievement for the field of radiation detection. Among the technologies capable of discovery, dual-phase noble element detectors are strong candidates and the work presented within this dissertation focuses on characterization of LAr as a target material. Following discovery, radiation detector development will need to push even further to produce science experiments that test standard model predictions and study short baseline neutrino behavior [66].

The development of detectors capable of observing CENNS parallels that of detectors searching for WIMP dark matter. As the name indicated, these hypothetical weakly interacting massive particles, predicted by supersymmetric extensions of the standard model, would interact much like the neutrinos of the standard model when coherently scattering with nuclei via exchange of the Z^0. Such interactions would result in nuclear recoils $\mathcal{O}$(0–100 keV) depending on the mass of the WIMP. Indeed, it is now recognized that CENNS interactions of solar and atmospheric neutrinos is the limiting background for searches for spin-independent WIMP interactions [14]. The search for this WIMP dark matter has made tremendous progress in deployment of large low-background detectors, but detector response to low-energy nuclear recoils (where expected signals will largest in number) remains an area where progress is still beneficial for extending the sensitivity of these detectors.

In this dissertation I have presented experimental demonstration of the ^{37}Ar calibration, the design and validation of a quasi-monoenergetic neutron source, measurement of 6.7 keV nuclear recoil ionization yield in liquid argon using this neutron source, and a proposed technique for producing sub-keV nuclear recoils via resonant photo-nuclear scatter. Additionally, in this chapter I have discussed how the neutron source may be used for additional nuclear recoil measurements in liquid argon and liquid xenon and how ultra-pure ^{37}Ar and ^{127}Xe may be produced. While this research was performed in a collaborative environment, the contents of this dissertation focus on my individual contributions and the collaborative experimental demonstration of ideas of my own conception. This work provides to the broader physics community; a demonstration of nuclear recoil sensitivity in LAr at energies lower than ever demonstrated, a quasi-monoenergetic neutron source design that may be used to perform similar nuclear recoil measurements at low-energies in various target media, a technique to make nuclear recoil measurements at sub-keV energies, and a low-energy introducible calibration source that might be used in future physics experiments.

Bibliography

[1] Acciarri, R. et al. "The WArP experiment". *Journal of Physics: Conference Series* 203.1 (2010), p. 012006.

[2] Afonin, A.I. et al. "Neutrino experiment involving inverse beta decay at a nuclear reactor". *JETP Lett. 37* (1983), pp. 150–153.

[3] Ahmad, Q.R. et al. "Measurement of the Rate of $\nu_e + d \rightarrow p + p + e^-$ Solar Neutrinos at the Sudbury Neutrino Observatory". *Phys. Rev. Lett.* 87 (7 2001), p. 071301. DOI: 10.1103/PhysRevLett.87.071301.

[4] Akimov, D. et al. "Detection of reactor antineutrino coherent scattering off nuclei with a two-phase noble gas detector". *JINST* 4.06 (2009), P06010.

[5] Alexander, T. and others. "Observation of the dependence on drift field of scintillation from nuclear recoils in liquid argon". *Phys. Rev. D* 88 (9 2013), p. 092006. DOI: 10.1103/PhysRevD.88.092006.

[6] Alexander, T. et al. "Light yield in DarkSide-10: A prototype two-phase argon TPC for dark matter searches". *Astropart.Phys.* 49 (2013), pp. 44–51. DOI: 10.1016/j.astropartphys.2013.08.004. arXiv: 1204.6218 [astro-ph.IM].

[7] Angle, J. et al. "A search for light dark matter in XENON10 data". *Phys.Rev.Lett.* 107 (2011), p. 051301. DOI: 10.1103/PhysRevLett.107.051301.

[8] Aprile, E. et al. "Simultaneous Measurement of Ionization and Scintillation from Nuclear Recoils in Liquid Xenon for a Dark Matter Experiment". *Phys. Rev. Lett.* 97.8 (2006), p. 081302. DOI: 10.1103/PhysRevLett.97.081302.

[9] Aprile, E. et al. "First Dark Matter Results from the XENON100 Experiment". *Phys. Rev. Lett.* 105.13 (2010), p. 131302. DOI: 10.1103/PhysRevLett.105.131302.

[10] Barbeau, P.S., Collar, J.I., and Tench, O. "Large-mass ultralow noise germanium detectors: performance and applications in neutrino and astroparticle physics". *JCAP* 2007.09 (2007), p. 009.

[11] Barbeau, P.S., Collar, J.I., and Whaley, P.M. "Design and characterization of a neutron calibration facility for the study of sub-keV nuclear recoils". *Nucl. Instrum. Methods Phys. Res., Sect. A* 574.2 (2007), pp. 385 –391. DOI: 10.1016/j.nima.2007.01.169.

[12] Barsanov, V.I. et al. "Artificial neutrino source based on the Ar-37 isotope". *Phys. Atom. Nucl.* 70 (2007), pp. 300–310. DOI: 10.1134/S1063778807020111.

[13] Beringer, J. et al. "Review of Particle Physics". *Phys. Rev. D* 86 (1 2012), p. 010001. DOI: 10.1103/PhysRevD.86.010001.

[14] Billard, J., Strigari, L., and Figueroa-Feliciano, E. "Implication of neutrino backgrounds on the reach of next generation dark matter direct detection experiments". *Phys.Rev.* D89 (2014), p. 023524.

[15] Bolozdynya, A. et al. "Opportunities for Neutrino Physics at the Spallation Neutron Source: A White Paper". *ArXiv e-prints* (Nov. 2012). arXiv: 1211.5199 [hep-ex].

[16] Bolozdynya, A.I. "Two-phase emission detectors and their applications". *Nucl. Instrum. Methods Phys. Res., Sect. A* 422.1-3 (1999), pp. 314 –320. DOI: 10.1016/S0168-9002(98)00965-6.

[17] Boulay, M.G. and Hime, A. "Direct WIMP detection using scintillation time discrimination in liquid argon" (2004). arXiv: astro-ph/0411358 [astro-ph].

[18] Bowden, N.S. et al. "Observation of the isotopic evolution of pressurized water reactor fuel using an antineutrino detector". *Journal of Applied Physics* 105.6, 064902 (2009). DOI: 10.1063/1.3080251.

[19] Brun, R. and Rademakers, F. "ROOT: An object oriented data analysis framework". *Nucl. Instrum. Methods Phys. Res., Sect. A* 389.1-2 (1997). New Computing Techniques in Physics Research V, pp. 81–86. DOI: 10.1016/S0168-9002(97)00048-X.

[20] Brunetti, R. et al. "WARP liquid argon detector for dark matter survey". *New Astronomy Reviews* 49.2-6 (2005). Sources and Detection of Dark Matter and Dark Energy in the Universe 6th {UCLA} Symposium on Sources and Detection of Dark Matter and Dark Energy in the Universe, pp. 265 –269. DOI: 10.1016/j.newar.2005.01.017.

[21] Chasman, C., Jones, K.W., and Ristinen, R.A. "Measurement of the Energy Loss of Germanium Atoms to Electrons in Germanium at Energies Below 100 keV". *Phys. Rev. Lett.* 15.6 (1965), pp. 245–248. DOI: 10.1103/PhysRevLett.15.245.

[22] Chasman, C. et al. "Measurement of the Energy Loss of Germanium Atoms to Electrons in Germanium at Energies below 100 keV. II". *Phys. Rev.* 154.2 (1967), pp. 239–244. DOI: 10.1103/PhysRev.154.239.

[23] Chepel, V. and Araujo, H. "Liquid noble gas detectors for low energy particle physics". *JINST* 8 (2013), R04001. DOI: 10.1088/1748-0221/8/04/R04001.

[24] Collar, J.I. "Applications of an ^{88}Y/Be Photoneutron Calibration Source to Dark Matter and Neutrino Experiments". *Phys. Rev. Lett.* 110 (21 2013), p. 211101. DOI: 10.1103/PhysRevLett.110.211101.

[25] Collar, J.I. "Quenching and channeling of nuclear recoils in NaI(Tl): Implications for dark-matter searches". *Phys. Rev. C* 88 (3 2013), p. 035806. DOI: 10.1103/PhysRevC.88.035806.

[26] Collar, J.I. and McKinsey, D.N. "Comments on 'First Dark Matter Results from the XENON100 Experiment'" (2010). arXiv: 1005.0838 [astro-ph.CO].

[27] Collé, R. and Kishore, R. "Excitation functions for (p,n) reactions on ^{79}Br and ^{127}I". *Phys. Rev. C* 9 (6 1974), pp. 2166–2170. DOI: 10.1103/PhysRevC.9.2166.

[28] Cowan, C.L. et al. "Detection of the Free Neutrino: a Confirmation". *Science* 124.3212 (1956), pp. 103–104. DOI: 10.1126/science.124.3212.103.

[29] Cushman, P. et al. "Snowmass CF1 Summary: WIMP Dark Matter Direct Detection" (2013). arXiv: 1310.8327 [hep-ex].

[30] Dahl, E. PhD thesis. Princeton University, 2009.

[31] Davis, R. "Solar Neutrinos. II. Experimental". *Phys. Rev. Lett.* 12 (11 1964), pp. 303–305. DOI: 10.1103/PhysRevLett.12.303.

[32] Davis, R., Harmer, D.S., and Hoffman, K.C. "Search for Neutrinos from the Sun". *Phys. Rev. Lett.* 20 (21 1968), pp. 1205–1209. DOI: 10.1103/PhysRevLett.20.1205.

[33] Doke, T. et al. "Absolute Scintillation Yields in Liquid Argon and Xenon for Various Particles". *Japanese Journal of Applied Physics* 41.Part 1, No. 3A (2002), pp. 1538–1545. DOI: 10.7567/JJAP.41.1538.

[34] Drosg, M. *Monoenergetic neutron production by two body reactions in the energy range from 0.0001 to 500 Mev*. Tech. rep. Institute of Experimental Physics, University of Vienna, 1999.

[35] Drukier, A. and Stodolsky, L. "Principles and applications of a neutral-current detector for neutrino physics and astronomy". *Phys. Rev. D* 30.11 (1984), pp. 2295–2309. DOI: 10.1103/PhysRevD.30.2295.

[36] Fermi, E. "An attempt of a theory of beta radiation. 1." *Z.Phys.* 88 (1934), pp. 161–177. DOI: 10.1007/BF01351864.

[37] Freedman, D.Z. "Coherent effects of a weak neutral current". *Phys. Rev. D* 9.5 (1974), pp. 1389–1392. DOI: 10.1103/PhysRevD.9.1389.

[38] Gaitskell, R.J. "Direct detection of dark matter". *Annu. Rev. Nucl. Part. Sci.* 54 (2004), pp. 315–359. DOI: 10.1146/annurev.nucl.54.070103.181244.

[39] Gastler, D. et al. "Measurement of scintillation efficiency for nuclear recoils in liquid argon". *Phys. Rev. C* 85 (6 2012), p. 065811. DOI: 10.1103/PhysRevC.85.065811.

[40] Hagmann, C. and Bernstein, A. "Two-phase emission detector for measuring coherent neutrino-nucleus scattering". *IEEE Trans. Nucl. Sci.* 51.5 (2004), pp. 2151 – 2155. DOI: 10.1109/TNS.2004.836061.

[41] Jones, K.W. and Kraner, H.W. "Stopping of 1- to 1.8-keV ^{73}Ge Atoms in Germanium". *Phys. Rev. C* 4.1 (1971), pp. 125–129. DOI: 10.1103/PhysRevC.4.125.

[42] Jones, K.W. and Kraner, H.W. "Energy lost to ionization by 254-eV ^{73}Ge atoms stopping in Ge". *Phys. Rev. A* 11.4 (1975), pp. 1347–1353. DOI: 10.1103/PhysRevA.11.1347.

[43] Joshi, T.H. "A novel source of tagged low-energy nuclear recoils". *Nucl. Instrum. Methods Phys. Res., Sect. A* 656.1 (2011), pp. 51 –54. DOI: 10.1016/j.nima.2011.07.044.

[44] Joshi, T.H. et al. "Design and demonstration of a quasi-monoenergetic epithermal neutron source" (2014). article in preparation.

[45] Joshi, T.H. et al. "First Measurement of the Ionization Yield of Nuclear Recoils in Liquid Argon". *Phys. Rev. Lett.* 112 (17 2014), p. 171303. DOI: 10.1103/PhysRevLett.112.171303.

[46] Kazkaz, K. et al. "Operation of a 1-liter-volume gaseous argon proportional scintillation counter". *Nucl. Instrum. Methods Phys. Res., Sect. A* 621.1-3 (2010), pp. 267 –277. DOI: 10.1016/j.nima.2010.06.088.

[47] Kishore, R. et al. "^{37}Cl$(p,\ n)^{37}$Ar excitation function up to 24 MeV: Study of $(p,\ n)$ reactions". *Phys. Rev. C* 12 (1 1975), pp. 21–27. DOI: 10.1103/PhysRevC.12.21.

[48] Kubota, S. et al. "Evidence of the existence of exciton states in liquid argon and exciton-enhanced ionization from xenon doping". *Phys. Rev. B* 13 (4 1976), pp. 1649–1653. DOI: 10.1103/PhysRevB.13.1649.

[49] Laffranchi, M., Rubbia, A., and collaboration), ArDM. "The ArDM project: a Liquid Argon TPC for Dark Matter Detection". *J. Phys.: Conf. Ser.* 65.1 (2007), p. 012014.

[50] Lee, C.L. and Zhou, X.-L. "Thick target neutron yields for the 7Li(p,n)7Be reaction near threshold". *Nucl. Instrum. Methods Phys. Res., Sect. B* 152.1 (1999), pp. 1 –11. DOI: 10.1016/S0168-583X(99)00026-9.

[51] Lindhard, J. et al. *Integral equations governing radiation effects*. 1963.

[52] Lippincott, W.H. et al. "Scintillation time dependence and pulse shape discrimination in liquid argon". *Phys. Rev. C* 78.3 (2008), p. 035801. DOI: 10.1103/PhysRevC.78.035801.

[53] Manzur, A. et al. "Scintillation efficiency and ionization yield of liquid xenon for monoenergetic nuclear recoils down to 4 keV". *Phys. Rev. C* 81.2 (2010), p. 025808. DOI: 10.1103/PhysRevC.81.025808.

[54] Marion, J.B. "Accelerator Calibration Energies". *Rev. Mod. Phys.* 38 (4 1966), pp. 660–668. DOI: 10.1103/RevModPhys.38.660.

[55] Marx, J. and Nygren, D. "The Time Projection Chamber". *Physics Today* 31 (10 1978). DOI: 10.1063/1.2994775.

[56] Mavrokoridis, K. "Light Readout Optimisation using Wavelength Shifter - Reflector Combinations". *Journal of Physics: Conference Series* 308.1 (2011), p. 012020.

[57] Metzger, F. "Resonance Fluorescence in Nuclei". *Progress in Nuclear Physics*. Vol. 7. 1959, pp. 54–88.

[58] Moreh, R. et al. "Strong photon strength in ^{40}Ar between 8 and 11 MeV". *Phys. Rev. C* 37.6 (1988), pp. 2418–2427. DOI: 10.1103/PhysRevC.37.2418.

[59] Mundy, J.N. and McFall, W.D. "Comparison of the Isotope Effect for Diffusion of Sodium and Silver in Lithium". *Phys. Rev. B* 7 (10 1973), pp. 4363–4370. DOI: 10.1103/PhysRevB.7.4363.

[60] Murzin, A.V. et al. "Neutron filters based on V, Mn, S, and the stable isotopes52Cr,56Fe,58Ni, and60Ni". English. *Soviet Atomic Energy* 67.3 (1989), pp. 699–701. DOI: 10.1007/BF01123214.

[61] Overley, J.C., Parker, P.D., and Bromley, D.A. "The energy calibration of tandem accelerators". *Nucl. Instrum. Methods* 68.1 (1969), pp. 61 –69. DOI: 10.1016/0029-554X(69)90689-2.

[62] Pozzi, S.A., Padovani, E., and Marseguerra, M. "MCNP-PoliMi: a Monte-Carlo code for correlation measurements". *Nucl. Instrum. Methods Phys. Res., Sect. A* 513.3 (2003), pp. 550 –558. DOI: 10.1016/j.nima.2003.06.012.

[63] Regenfus, C. et al. "Study of nuclear recoils in liquid argon with monoenergetic neutrons". *Journal of Physics: Conference Series* 375.1 (2012), p. 012019. DOI: 10.1088/1742-6596/375/1/012019.

[64] Roberts, M.L. et al. "The stand-alone microprobe at Livermore". *Nuclear Instruments and Methods in Physics Research Section B: Beam Interactions with Materials and Atoms* 158.1-4 (1999), pp. 24 –30. DOI: 10.1016/S0168-583X(99)00362-6.

[65] Sangiorgio, S., Joshi, T.H., et al. "First demonstration of a sub-keV electron recoil energy threshold in a liquid argon ionization chamber". *Nucl. Instrum. Methods Phys. Res., Sect. A* 728.0 (2013), pp. 69 –72. DOI: 10.1016/j.nima.2013.06.061.

[66] Scholberg, K. "Prospects for measuring coherent neutrino-nucleus elastic scattering at a stopped-pion neutrino source". *Phys. Rev. D* 73 (3 2006), p. 033005. DOI: 10.1103/PhysRevD.73.033005.

[67] Sorensen, P. and Dahl, C.E. "Nuclear recoil energy scale in liquid xenon with application to the direct detection of dark matter". *Phys. Rev. D* 83 (6 2011), p. 063501. DOI: 10.1103/PhysRevD.83.063501.

[68] Sorensen, P. et al. "The scintillation and ionization yield of liquid xenon for nuclear recoils". *Nucl. Instr. Meth. A* 601.3 (2009), pp. 339 –346.

[69] Swan, D.W. "Drift velocity of electrons in liquid argon, and the influence of molecular impurities". *Proceedings of the Physical Society* 83.4 (1964), p. 659.

[70] Szydagis, M. et al. "NEST: a comprehensive model for scintillation yield in liquid xenon". *Journal of Instrumentation* 6.10 (2011), P10002.

[71] Tanaka, K. et al. "Irradiation characteristics of BNCT using near-threshold 7 Li(p, n) 7 Be direct neutrons: application to intra-operative BNCT for malignant brain tumours". *Physics in Medicine and Biology* 47.16 (2002), p. 3011. DOI: 10.1088/0031-9155/47/16/315.

[72] *Technologies Underlying Weapons of Mass Destruction*. Tech. rep. U.S. Congress, Office of Technology Assessment, 1993.

[73] Thomas, J. and Imel, D.A. "Recombination of electron-ion pairs in liquid argon and liquid xenon". *Phys. Rev. A* 36 (2 1987), pp. 614–616. DOI: 10.1103/PhysRevA.36.614.

[74] Tuli, J.K. "Evaluated nuclear structure data file". *Nucl. Instrum. Methods Phys. Res., Sect. A* 369.2-3 (1996), pp. 506 –510. DOI: 10.1016/S0168-9002(96)80040-4.

[75] Vogel, P. and Engel, J. "Neutrino electromagnetic form factors". *Phys. Rev. D* 39 (11 1989), pp. 3378–3383. DOI: 10.1103/PhysRevD.39.3378.

[76] Weber, R.O. et al. "Cross sections and thermonuclear reaction rates of proton-induced reactions on ^{37}Cl". *Nuclear Physics A* 439.1 (1985), pp. 176 –188. DOI: 10.1016/0375-9474(85)90212-X.

[77] Weller, H.R. et al. "Research opportunities at the upgraded HIγS facility". *Prog. Particle and Nucl. Phys.* 62.1 (2009), pp. 257 –303.

Appendix A

Installation and Calibration at CAMS

Several problems associated with the Li-target were encountered when building the neutron source at CAMS (Chapter 3). Here I expand on the installation process, beam energy calibration, the problems encountered, and our final understanding of the target used for neutron source validation and 6.7 keV endpoint measurements.

A.1 Target Problems at CAMS

The original Li-target installed at CAMS was inherited from researchers at LLNL. This target, 10 μm of metallic Li evaporated on a 3 mm thick silver puck, sat unused for $\sim$ 6 years in a triple vacuum sealed container before we acquired it and set out to install it at CAMS. Installation, was performed within a glove bag with continuous Ar flow to limit the oxidation of the Li-target. A flange was fabricated to clamp the target within the accelerator target area and provide sufficient conductive cooling. The final section of the accelerator vacuum chamber, upon which the target-holding flange was mounted, was electrically isolated and used as a Faraday cup for beam current integration.

Following successful installation of this target, the shielding described in Chapter 3 was assembled and radiation safety surveys were performed. These surveys were informed by several MCNPX simulations that were run during design of the shielding and quantified expected dose based on conservative assumptions about performance of the Li-target, yield of the 478 keV (p,p') gammas produced within the target, and 478 keV production during neutron capture in the borated polyethylene shielding. The radiation surveys showed much lower ($\times 10 - 20$) levels of neutrons that expected, suggesting some problems with our apparatus.

The process of identifying the yield problem resulted in a study of the many assumptions we had made up to this point. We were confident in our approximate calibration of proton beam energy (discussed in the next section) having verified it with both a Si-detector and the neutron producing reaction threshold. Our first step was checking the beam alignment using a camera

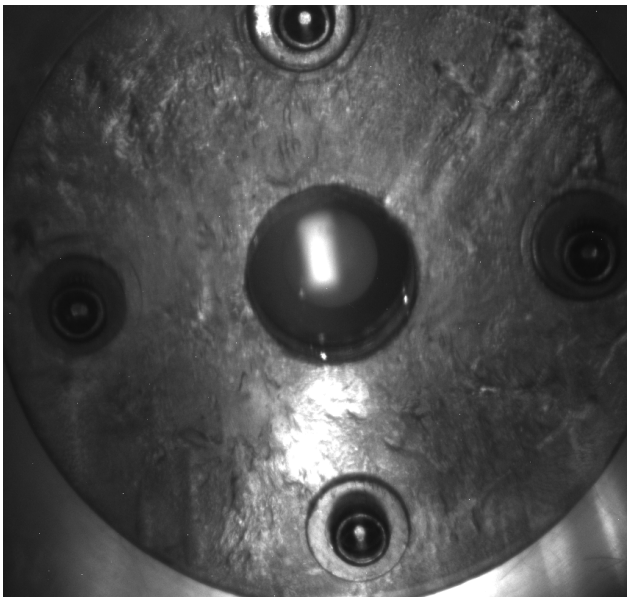

Figure A.1: Photograph of proton beam (bright rectangle at center) incident on the Li-target (gray circle at center).

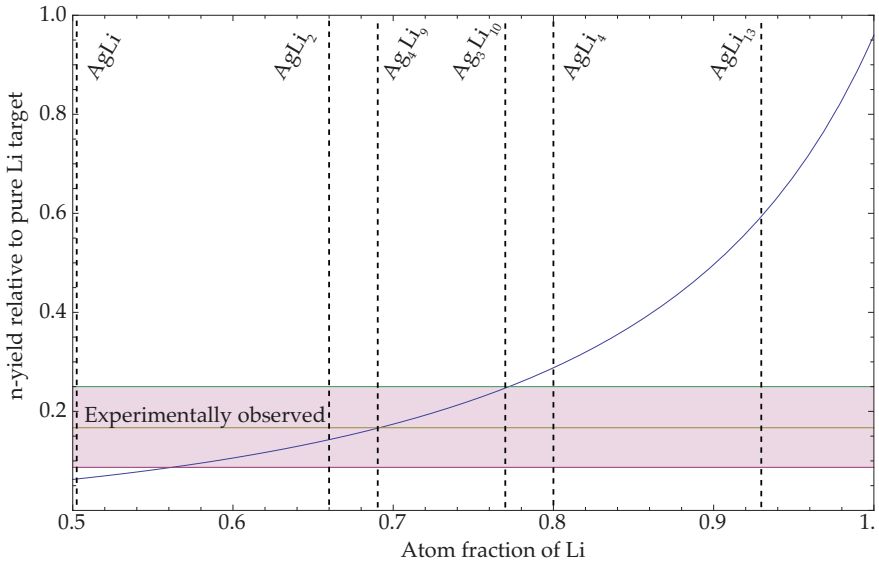

Figure A.2: Relative neutron yield versus Ag content in Li-target indicating lithium diffusion into the silver backing is a plausible explanation for target behavior.

to image the proton beam incident on the Li-target shown in Fig. A.1. Following this, we set out to study the neutron and gamma yield of the installed target by removing all of the shielding and using the moderated ^{3}He tubes discussed in Chapter 3 placed up against the target holding flange, and using NaI detectors in different locations near the flange. From these measurements the neutron yield was 16±7% of expected and 478 keV gamma yield 78% of expected (from inelastic scatter on ^{7}Li). Around this time additional conversations also resulted in the realization that Li has a very large diffusion constant in Ag at room temperature (D=5×10^{-11} cm^2/s) [59].

While this diffusion constant is likely incorrect for the large concentrations of Li, it serves as a good starting point. Assuming this value, after 6 years our Li target would be 80% Ag. To understand the observed neutron yield behavior I made a quick calculation with the following assumptions: Li content of the target is constant; stopping power of the target is the linear combination of the Ag and Li components (Bragg's rule); the alloy target is homogenous; stopping power of the alloy target is constant over the relevant proton energy window. With these assumptions I calculated expected neutron yield as a function of lithium number density, shown in Fig. A.2, along with AgLi room temperature phases. Compositions of 50–60% Li would result in the observed 478 keV gamma yields. From this analysis we concluded that our inherited Li-target slowly self-destructed via room temperature Li diffusion into the Ag backing.

With the help of Jason Burke, we acquired three new Li-metal targets. They were fabricated in France by Vincent Meot. Each target was approximately 1 μm of Li evaporated on a Ta puck. Installation of targets was performed as before, using a glove bag and continuous Ar flow. Neutron yield measurements were again taken, and again were lower than expected. To assess the target composition Rutherford backscatter analysis of one target was performed at LLNL by Sergey

Kucheyev. The resulting analysis showed a lithium carbonated (Li_2CO_3) composition, indicating exposure to air. A comparison of expected yield with metallic lithium, lithium carbonate, and the observed yield as a function of energy, shown in Fig. A.3, verified this. We concluded that the target installation using glove bags did not provide a sufficiently clean environment for target installation. Unfortunately all three targets were compromised because they had been packaged together. As illustrated in Chapter 3, this caused a significant reduction in rate and increase in background from neutrons of energies outside of the relevant energy band. Analysis of the endpoint measurement using lithium carbonate targets showed that it would still be viable, so these targets were used for the remainder of measurements.

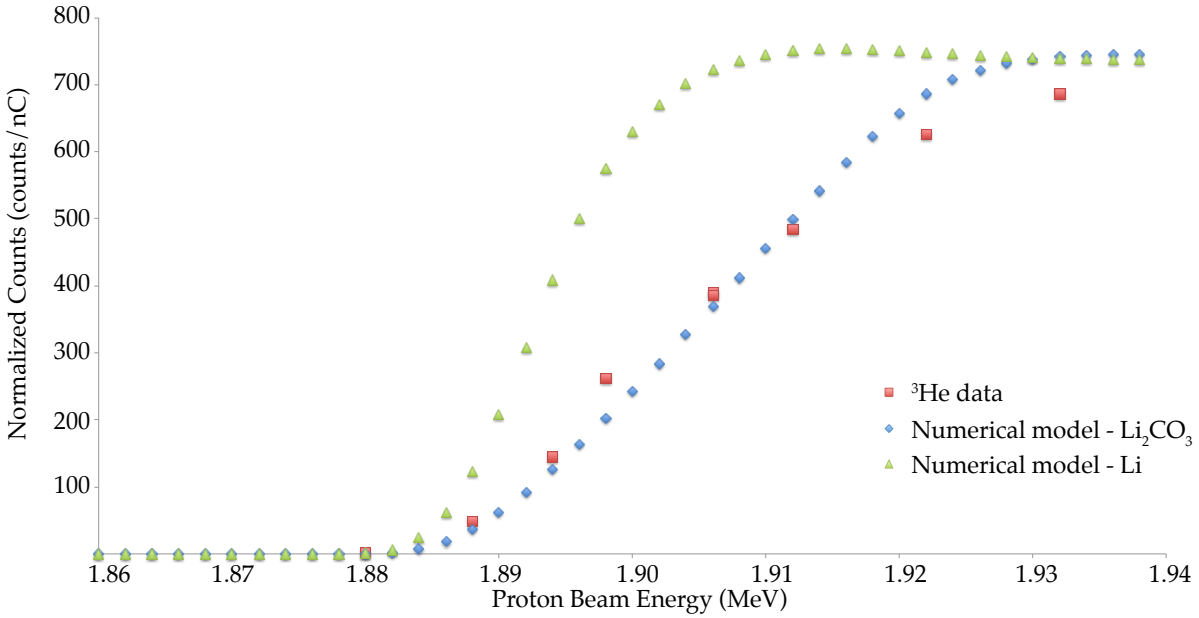

Figure A.3: Lithium carbonate rates vs. energy and expectations from carbonate and metallic lithium. Results suggest lithium target was exposed to air producing a carbonate target.

A.2 Calibrating the Proton Beam at CAMS

Three approaches were used to calibrate the proton beam energy from the microprobe at CAMS. The first was use of a Si-detector (Ametek TB-018-150-200) installed in the beam line, the second used knowledge of the ^{7}Li(p,n)^{7}Be threshold and measured neutron yields vs. proton energy, and the third exploited the notch transmission of iron and kinematics of the ^{7}Li(p,n)^{7}Be reaction. Proton beam energy was understood to be $E_p = 2 \times E_{term} + E_{IS}$, where E_{term} is the terminal potential and E_{IS} is the energy of ions delivered by the ion source.

We measured the proton beam energy using a Si-detector that was installed on a translation stage within the CAMS target along with a ^{226}Ra calibration source. The calibration of this detector and results from proton beam calibration are shown in Fig. A.4. This exercise exposed $\sim$20 keV difference in expected and measured beam energy.

Proton beam energy was also validated using the known threshold for neutron production via ^{7}Li(p,n)^{7}Be (1.885 MeV). Measurements were performed using moderated ^{3}He tubes placed directly in front of the Li-target holding flange (0°). Proton beam energy was increased and the current normalized neutron count rate was measured. As performed in [61, 54], the yield (background subtracted count-rate) taken to the 2/3rd power was plotted as a function of beam energy and a linear fit made (Fig. A.5). The x-intercept of this fit corresponds to the threshold which is known. The $\sim$20 keV difference between expected and measured beam energy was also observed with this technique.

While the previous method was useful in calibrating the proton beam energy, it required complete disassembly of the shielding around the Li-target. An alternate approach was used, again with the moderated ^{3}He tubes, relying on knowledge of the reaction kinematics and neutron transmission properties of an Fe filter placed within the borated polyethylene collimator (see Fig. 3.5). The neutron transmission rate through the collimator/filter was measured using the ^{3}He tubes as a function of proton beam energy and an increase, corresponding to the 24 keV notch in the Fe filter (Chapter 3) was easily identified. Using kinematic calculations for the ^{7}Li(p,n) reaction and collimation at a known angle, the calibration of the proton beam energy was measured (Fig. 3.6). This method also identified the difference in expected and measured beam energy, and that this difference slowly drifted. This calibration approach was used throughout data taking for the measurements in Chapter 4 to correct for the small drift in proton beam energy.

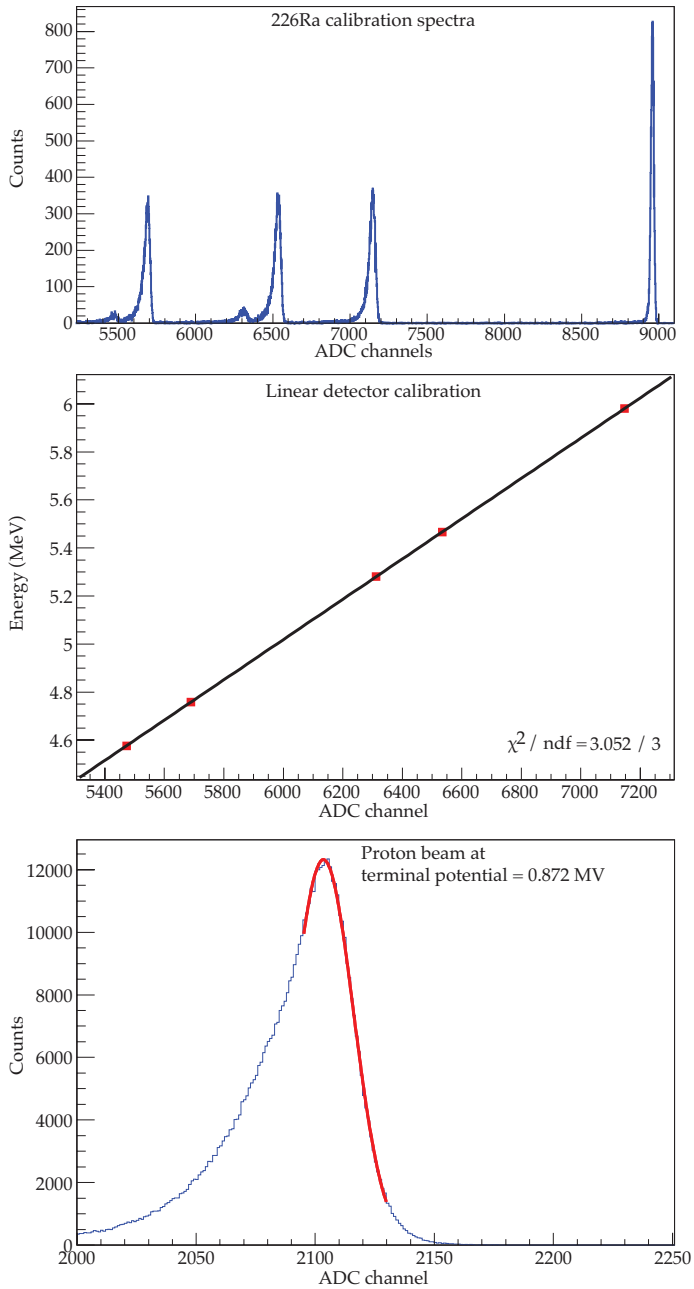

Figure A.4: (top) ^{226}Ra calibration alpha spectra taken inside the CAMS target chamber with the Si detector. (middle) Linear calibration of the 5 lowest energy peaks from the calibration spectra. (bottom) Spectra from protons incident on Si detector. Terminal potential was 0.872 MV. This shed light on a $\sim$ 20 kV discrepancy in expected and observed beam energy.

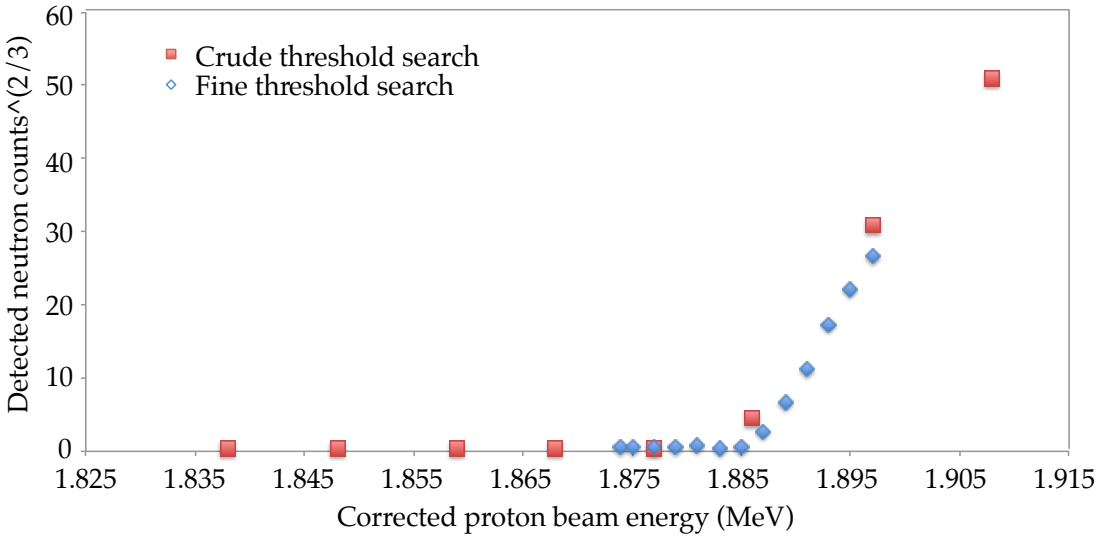

Figure A.5: Neutron count rate in moderated ^{3}He tubes to the 2/3rd power vs. beam energy.

A.3 Detector Installation

The G/NARRLI detector was assembled in B432 at LLNL. The design was semi-noble to allow for straight-forward transport to the beam facility at CAMS (B190). The detector was moved with a flatbed truck. Disassembly, transport, and reassembly took about a day. Below are several photographs of the detector in transit and installed at LLNL (Figs. A.6,A.7). During installation the rotatable table was aligned to the target-holding flange using a laser alignment system. The alignment used a 45° mirror mounted to the flange and a laser that attached to the rotatable table. The table was positioned such that the return beam entered its origin. This procedure was performed with the detector dewar dropped, allowing the laser to pass through the active volume of the detector.

Figure A.6: Photograph of the detector equipment outside CAMS during transport.

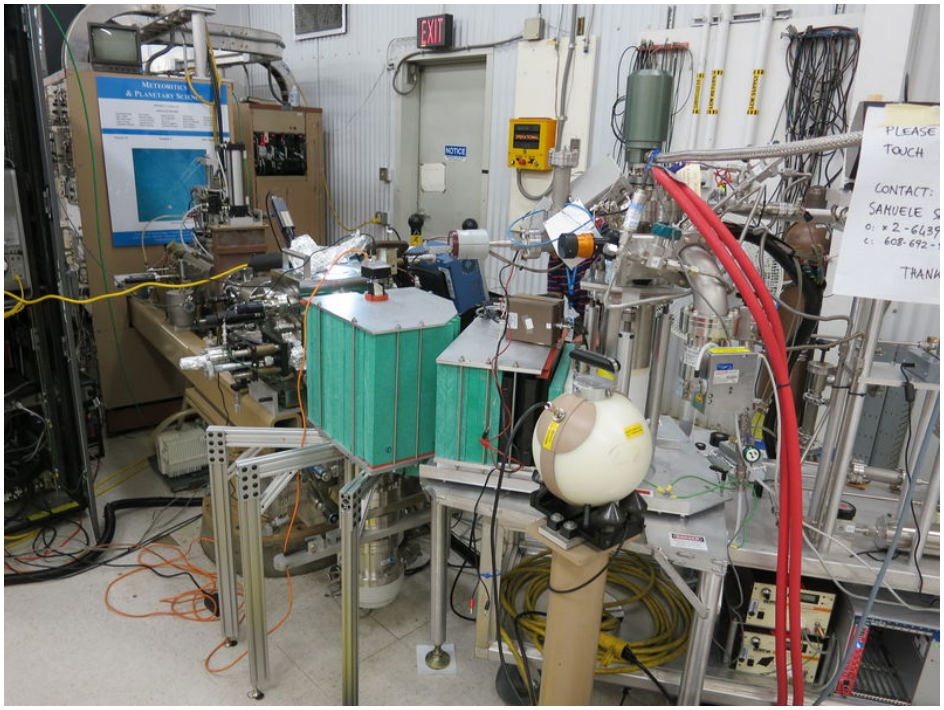

Figure A.7: Photograph of the detector at CAMS. The target station, shielding, collimator, and rotatable table holding the detector are visible. A spherical neutron dose instrument used to survey the radiation field is obstructing clear view of the detector dewar.

Appendix B

Single Electron Calibration

Calibration of the single electron response of G/NARRLI was required because single electrons were not observed in large enough quantities during measurements without the ^{55}Fe source assembly. To calibrate the single electron light yield (PEs/electron), an analysis was performed with ^{37}Ar data acquired when the single electron peak was present and ^{37}Ar data acquired during the cool down where calibration was needed. In this section I discuss the methodology of this calibration.

Two groups of data were used during the single electron calibration. The first group set (SE) was composed of six data sets acquired at drift fields of 600, 1200, 1600, 1800, 2400, and 3000 V/cm with ^{37}Ar present. A single electron peak was visible in all six of these data sets and the gain field was held constant. The centroid and shape of the single electron peaks from group SE were constant with respect to change in the applied drift field. The mean value of the peak centroids was used as the single electron calibration for all six sets. The uncertainty in the mean was used as the statistical uncertainty for this parameter. Additionally, an asymmetric 10% systematic uncertainty was included with this value because of the inability to apply a fiducial cut to single electron events. This calibration was used to transform fiducialized 2.82 keV ^{37}Ar data from PE to detected electrons, and therefore must represent the single electron signal for central electrons.

Following the acquisition of nuclear recoil data at CAMS, ^{37}Ar was injected into the detector. After a 30 minute equilibration period four data sets were acquired at same drift fields as the nuclear recoil data (240, 640, 1600, 2130 V/cm) and the same gain field. These data sets compose data group EP. Clear single electron peaks were not observed in these data sets.

The 2.82 keV single electron calibration data (Fig. 2.19) were well described by the modified Thomas-Imel box model discussed in Sec. 4.4. To perform the single electron calibration used in Ch. 4, a simultaneous fit of this functional form was made to the 2.82 keV peak data from both data groups. This fit had three free parameters; b, C, and S where S (SPE/e^{-}) is the single electron calibration for data group EP.

Figure B.1 shows the simultaneous fit of 2.82 keV peak locations for both datasets. Statistical uncertainties on the 2.82 keV peak locations were included in addition to the statistical uncertainty associated with the single electron calibration for data group SE. The best fit of $S = 10.4 \pm 0.1$ was found in this fit. Additionally, a 10% systematic uncertainty to account for this calibration methodology was included with the asymmetric 10% systematic uncertainty associated with the fiducialization of single electron data.

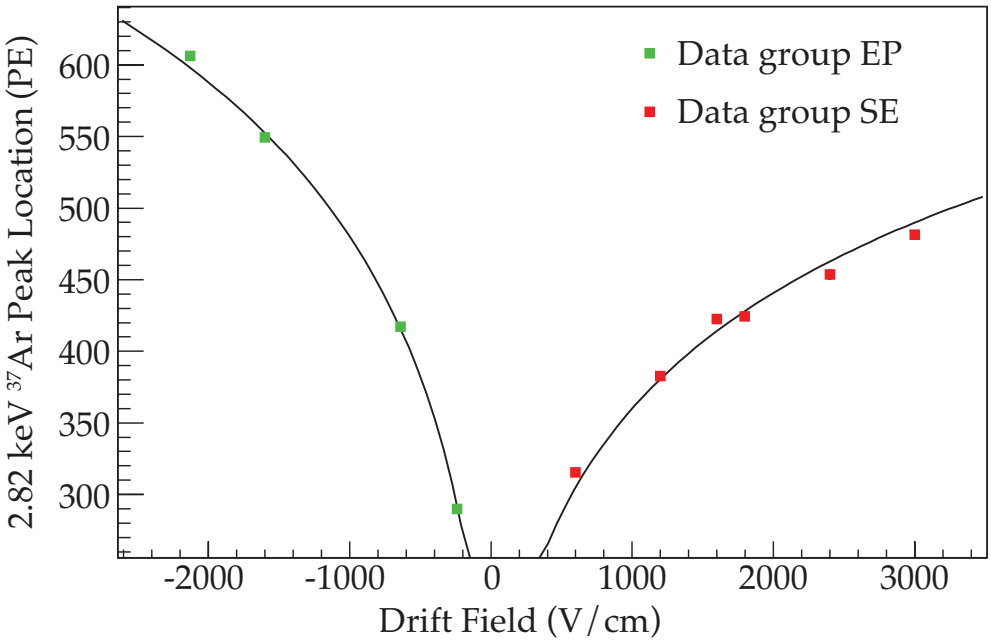

Figure B.1: Simultaneous fit of 2.82 keV ^{37}Ar peak using the modified Thomas-Imel model (Chapter 4). Statistical uncertainties on peak location are smaller than the marker size. Systematic uncertainties are not shown.

Appendix C

Endpoint Analysis

The analysis of endpoint data was described in Chapter 4. In this Appendix I expand on the process used to transform the expected nuclear recoil spectrum into an expected ionization spectrum and show the impact of variation of F' and the slope of ionization yield with recoil energy.

The expected single-site nuclear recoil spectrum (Fig. 4.2) was produced from detailed MCNP-PoliMi simulations using a neutron source term defined using the procedure discussed in Chapter 3 and described in [50]. The histogram of single-site recoil events at 45° and 55° was binned in 100 eV intervals and read in to a ROOT script. These histograms were subtracted to represent the background subtraction process used to isolate the contributions of the 70 keV neutrons.

Transformation of this expected recoil spectra to an expected ionization spectra required five inputs: normalization, a resolution term (F′), ionization yield at 6.7 keV – $Q_y(6.7\text{ keV})$, the slope of ionization yield with respect to recoil energy (M_Q), and single electron resolution (σ_e). The first three terms were left free and swept over in a parametric sweet for χ^2 minimization. M_Q was conservatively assumed to be zero, but later allowed to float for determination of the systematic uncertainty of this assumption. Single electron data was used to define $\sigma_e = 0.37$. The ionization yield below 500 eV was assumed to be zero.

The spectrum was first transformed to number of electrons (n_e) by multiplying the contents of each recoil energy bin by the input ionization yield $Q_y(E_r) = Q_y(6.7\text{ keV}) - (6.7 - E_r)M_Q$. Next, each bin of the ionization spectrum was smeared using the resolution term $\sigma(n_e) = \sqrt{n_e(F' + \sigma_e^2)}$. Figure C.1 illustrates this process for $F' = 0, 0.5, 1, 2$.

This expected ionization spectrum was then compared with the background subtracted experimental spectra using a least-squares analysis. While I conservatively assumed that $M_Q = 0$, it was found that $M_Q < 0$ produced better agreement with the data for $\mathcal{E} = 640, 1600, 2130$ V/cm. Figure C.2 illustrates a best fit when M_Q was allowed to float when fitting $\mathcal{E} = 640$ V/cm. Such findings were also similar if the fitting range was extended to lower numbers of electrons (fitting over a larger recoil energy range). While it is tempting to draw conclusions regarding the ionization yield of lower energy recoils from this analysis, the kinematic endpoint is the only energy that may be unambiguously resolved.

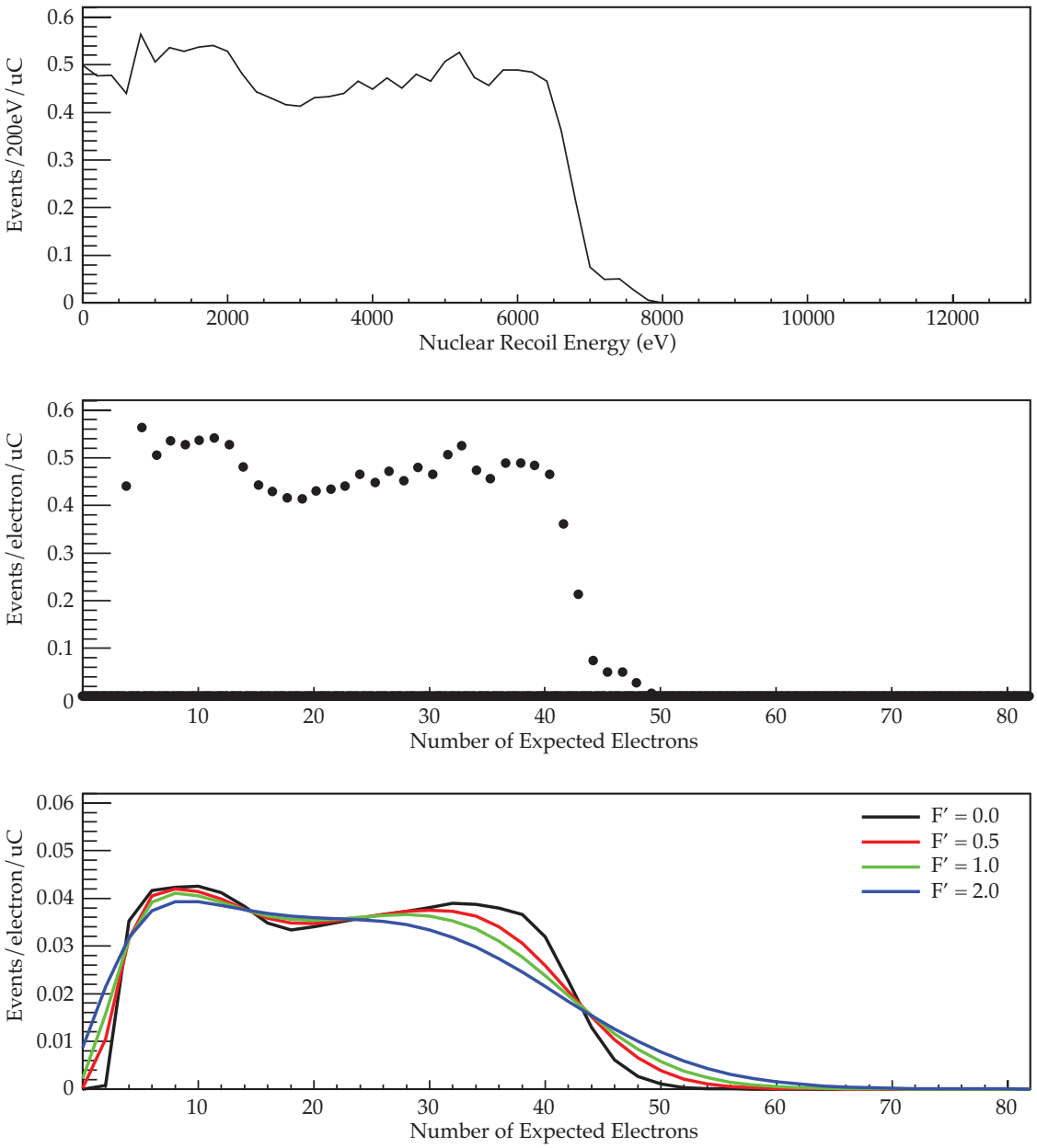

Figure C.1: Transformation from expected recoil spectrum to expected ionization spectrum. (top) Expected nuclear recoil spectrum from MCNP Polimi simulation. (middle) Transformation to number of expected electrons by multiplication of the ionization yield function. (bottom) Expected number of electrons after smearing with the resolution term for different values of F'.

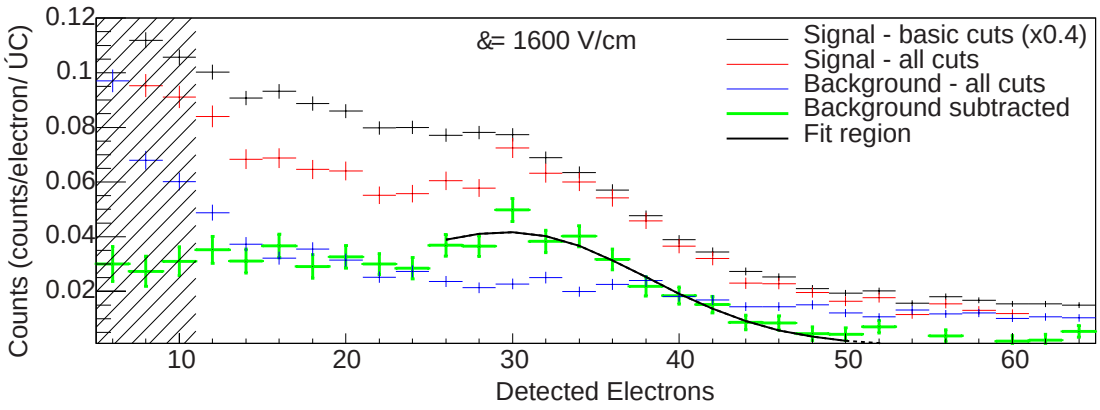

Figure C.2: Best fit of 1600 V/cm nuclear recoil data with floating Q_y slope. Best fit slope of $-0.8Q_y/keV$ indicates the ionization yield is increasing below 6.7 keV, however the degenerate nature of the terms within this analysis make conclusions about the ionization yield below the endpoint inadvisable.